Seed layer assisted solution growth of aligned ZnO nanostructure arrays for electron transport layer in dye and perovskite solar cells

A Thesis

Submitted

in Partial Fulfillment of Requirements for the award of the degree of

Doctor of Philosophy

In

Materials Engineering

By

NANOJI ISLAVATH

(Reg. No. 11ETPM12)

School of Engineering Sciences and Technology
UNIVERSITY OF HYDERABAD
August 2016

Seed layer assisted solution growth of aligned ZnO nanostructure arrays for electron transport layer in dye and perovskite solar cells

A Dissertation Submitted in Partial Fulfillment of
Requirements for the Doctor of Philosophy

In

Materials Engineering

By

NANOJI ISLAVATH
(Reg. No. 11ETPM12)

Under the guidance of

Dr. Dibakar Das (UoH)
Dr. Easwarmoorthi Ramasamy (ARCI)

UNIVERSITY OF HYDERABAD
School of Engineering Sciences and Technology
August 2016

Declaration

I declare that this written submission represents my ideas in my own words, and where others' ideas or words have been included, I have adequately cited and referenced the original sources. I also declare that I have adhered to all principles of academic honesty and integrity and have not misrepresented or fabricated or falsified any idea/data/fact and source in my submission. I understand that any violation of the above will be a cause for disciplinary action by the Institute and can also evoke penal action from the sources that have thus not been properly cited, or from whom proper permission has not been taken when needed.

Nanoji Islavath
11ETPM12

School of Engineering Sciences and Technology

UNIVERSITY OF HYDERABAD

CERTIFICATE

This is to certify that the work contained in this thesis entitled ”Seed layer assisted solution growth of aligned ZnO nanostructure arrays for electron transport layer in dye and perovskite solar cells”, has been carried out by Mr. Nanoji Islavath under my supervision and the same has not been submitted for the award of research degree of any university.

DR. DIBAKAR DAS (UoH)
Research Supervisor

DR. EASWARAMOORTHI (ARCI)
Research Supervisor

PROF. M. GHANASHYAM KRISHNA
Dean of SEST

Acknowledgments

It had been a wonderful journey of five years in my life with lot surprise and delight. This Ph.D tenure not only taught me science various experiments but also it provided me an to learn a lot from different people, tradition and culture. It provided me with an essence of research and life through various concepts and interesting people. So it is my duty to thank each and every one, who were influence in this pivotal period of my life.

At the outset, I would like to express my sincere gratitude to Prof. Shrikant. V. Joshi, Former Additional Director, ARCI, for providing me an opportunity to work as a internal Ph.D. research scholar at ARCI in CSEM. I sincerely thank Prof. Sundararaman Mahadevan Former Dean, and Prof. M. Ghanashyam Krishna (Dean), UoH, for permitting me to register for Ph.D.

I am greatly indebted to my mentors Dr. Dibakar Das (SEST, UoH) and Dr. Easwaramoorthi Ramasamy (CSEM, ARCI) for their timely support, valuable guidance, and encouragement throughout my doctoral studies. I am privileged to work with Dr. Easwaramoorthi Ramasamy, who has been guiding me day to day in all the experiments, analyses and discussions. I felt the utmost care and affection from her in and out of the laboratory and the way he supported me even during my tough times is simply exceptional. I am very fortunate to work with Dr. Dibakar Das, my internal guide at UoH, who is, without a doubt, an exemplary supervisor. The way he contributed to my thesis work with pertinent suggestions during experiments and analysis of the results is incredible. I am very grateful to him for his personal concern to me during my tough times. I am honored to have Dr. Shrikant V. Joshi, Additional Director, and ARCI, as one of my off-screen mentors. I have been fortunate for the last four years to get his time for my research work discussions and doctoral committee meetings. His valuable suggestions and comments contributed significantly to my thesis. He has given a tremendous support and took personal care during the difficult times of Ph.D. I am extremely happy to have worked with above three and I am always obliged to them. I am at loss of words to thank them for their constant support for the last four years.

I sincerely thank Dr. Sanjay R. Dhage (CSEM) and Dr. G. Ravi

Chandra, Team Leader, Centre for Materials Characterization and Testing, for getting the characterizations done and his valuable suggestions related to sample preparation. I would like to thank Dr. K. Suresh, Mrs. Jyotirmayi, Mr. M. Ramakrishna, Mr. K. Ramesh Reddy and Mr. L. Venkatesh for their great help in the characterization of the samples. I am very thankful to my lab mates Mrs. Saroja, Mrs. Swathi, Ms. Sandhya rani, Mr. Hariesh, Mr. Srinivas Reddy, Mr. Santhan Reddy and Mr. Arvind who has helped me during experiments.

I like to thank my friends Mr. Hari Mohan, Bolla Reddy, Dr. Pramod, Dr. Uday Bhaskar, Mr. Amol, Mr. Brijesh, Mrs. Divya at ARCI and Mr. Pardhu Yella, Mr. satyanarayana, Mr. Nagaraju and Mr. Satti babu at UoH for their help in various aspects. I am very fortunate to have good friends. I am very thankful to my batch mates at ARCI and UoH for their loving support, loyal friendship, and pleasant company.

I owe to my parents (Mr. Bucha Islavath and Mrs. Rangamma), my brother (Mr. Ramesh Islavath) and my sister-in-law (Ms. Sowmya Dale) who have been a constant source of encouragement and driving force that helped me overcome the rigors of research work.

Dedicated to Prof. Sundararaman Mahadevan,
Prof. Shrikant V. Joshi and my parents...

Abstract

The work documented in this thesis describes the growth of aligned ZnO nanostructures on transparent conductive substrates and their application as electron transport layer in dye and perovskite solar cells. The seed layer is critical for the growth of aligned ZnO nanostructures on nonepitaxial substrates. In this work, ZnO seed layer was prepared by spray coating and optimization of the spray parameters, whereby precursor flow rate and volume were particularly influential in attaining preferably oriented and uniform ZnO seed layer. In specific, the high-tech advantages of aligned one-dimensional (1D) ZnO nanowires are successfully demonstrated in dye and perovskite solar cells. The superior performance observed in devices constructed using 1D nanowire is usually attributed to enhanced electron transport and quantum confinement effect. The seed layer-dependant growth mechanism of aligned ZnO nanostructure is studied in detail. The seed layer-nanostructure interface investigated by electron microscopy reveals that nanostructures grow directly on top of the individual seed grains. Moreover, microstructural features of grown nanostructures are largely influenced by seed grain size. Expanding from the 1D nanowires, aligned three-dimensional (3D) nanowalls are novel building blocks for devices those require not only facile carrier transport path but also the higher surface area. Nevertheless, well aligned 1D nanowires and 3D nanowalls received less attention, presumably because of the difficulties in retaining their shape during the growth process. Here, we report a facile and scalable low-temperature solution approach to grow well aligned 1D nanowires and 3D ZnO nanowall on transparent conductive substrate by introducing a controlled amount of Al into a seed layer. By varying Al content in the seed layer, the morphology of ZnO nanostructure is gradually changed from 1D nanowire to 3D nanowall arrays. Conductive-probe atomic force microscopy studies show that ZnO nanostructures grown on Al-ZnO seed layer provide a higher average current of 200 nA at 0.6 V, as compared to 95 nA yielded by nanostructures grown on ZnO seed layer. Consequently, perovskite solar cells are fabricated using aligned 3D ZnO nanowalls as electron transport layer and maximum power conversion efficiency 2.6 % is demonstrated. The large void space available across the 3D ZnO nanowalls can be further functionalized with a suitable metal oxide to enhance the surface area, thereby one can expect higher absorber loading, and electron transport, as evidenced by higher photocurrent density 9.65 $\mathrm{mA.cm^{-2}}$ and power conversion efficiencies of 3.65 %.

Abbreviations

List of Nomenclature

1-D	One dimensional
2-D	Two dimensional
3-D	Three dimensional
AM	Air mass
Al-ZnO	Al doped ZnO
a-Si	Amorphous silicon
CB	Conduction band
CE	counter electrode
CV	Cyclic voltammetry
DMF	N,N-dimethylformamide
DSSC	Dye-sensitized solar cell
EQE	External quantum efficiency
Eg	Band gap energy
E_F	Fermi level
Eredox	Redox potential or electrolyte energy mediator
EIS	Electrochemical impedance spectroscopy
FWHM	Full width at half maximum
FF	Fill factor
FTO	Fluorine doped tin oxide
GBL	γ-Butyrolactone
GT	Growth Time
HOMO	Highest occupied molecular orbital
HR-TEM	High-resolution transmission electron microscopy
HTM	Hole-transporting material
J	Current density
Jo	Saturation current density
JCPDS	Joint committee on powder diffraction standards
Jph	Photocurrent density
J_{sc}	Short circuit current density
I	Current
IPCE	Incident photon–to–electron conversion efficiency
IQE	Internal quantum efficiency

LHE	Light-harvesting efficiency
LiTFSI	Lithiumbis(trifluoromethylsulfonyl)imide
LUMO	Lowest unoccupied molecular orbital
MO	Metal oxide
mc	Mono-crystalline
NHE	Normal hydrogen electrode
nm	Nanometer
NW	Nanowire
NWL	Nanowall
PCE	Solar–to–electrical power conversion efficiency
pc	Poly-crystalline
PEC	Photoelectrochemical
PV	Photovoltaic
PSC	Perovskite solar cell
rpm	Revolutions per minute
RT	Room temperature
R_s	Series resistance
ssDSC	Solid-state dye sensitized solar cell
SAED	Selected area electron diffraction
SEM	Scanning electron microscopy
SL	Seed layer
TBP	4-tert-butylpyridine
TCO	Transparent conductive oxide
TEM	Transmission electron microscopy
V	Voltage
V_{oc}	Open circuit voltage
UV	Ultraviolet
VB	Valence band
Vis	Visible
V_{th}	Threshold voltage
XRD	X-ray diffraction spectroscopy

List of Symbols

α	Absorption coefficient
κ	Boltzmann constant
σ	Conductivity
Θ	Diffraction angle (XRD)
L_d	Diffusion length
ρ	Resistivity
η	Efficiency
Φph	Incident photon flux
ε	Molar extinction coefficient
μ	Mobility
ϵ	Permittivity
λ	Wavelength (in nm)

Physical Constants

$2.998 \text{ X } 10^{8}$ m.s^{-1}	Speed of light (c)
$1.602 \text{ X } 10^{-19}$ C	Elementary charge(e)
$9.64 \text{ X } 10^{4}$ C . mol^{-1}	Faraday constant (F)
$6.626 \text{ X } 10^{-34}$ J.s	Planck constant(h)
$1.3181 \text{ X } 10^{-23}$ J . K^{-1}	Boltzmann constant(k)

Contents

List of Figures

List of Tables

Chapter 1

Introduction

”I have no doubt that we will be successful in harnessing the sun’s energy. If sunbeams were weapons of war, we would have had solar energy centuries ago.”

-George Porter-Nobel Prize winner in Chemistry, 1967.

Energy is one of the essential needs of human society. However, the continued increase in energy consumption causes depletion of fossil (i.e., oil, gas, and coal) energy resources [1]. On the other hand, the excessive release of greenhouse gasses, caused by burning fossil fuel, results in global warming, jeopardizing the Earth’s ecosystem. Yet, nuclear power is not a viable alternative to carbon-based fuel due to the unacceptable global risks and a problem of waste disposal [2]. Accordingly, development of affordable renewable energy sources has become necessary. Considerable scientific endeavors have focused on the design of technologies that utilize one of the four primary renewable energy resources-solar irradiation, the wind, water, and biomass-for power generation [3]. Due to the huge amount of energy that the Earth receives daily from the Sun, solar energy is seen as the strongest candidate to alleviate the world’s energy crisis.

One of the most prominent strategies based on solar power use is the direct conversion of sunlight into electricity using solar cells. Conventional silicon and copper indium gallium selenide (CIGS) solar cell technologies that permit an efficient conversion of solar energy into electrical power were developed and commercialized a few years ago. However, energy-intensive fabrication processes and the high cost per Watt are not competitive with the conventional power.

In the last six years, several promising alternatives based on cost-efficient inorganic and organic materials have been proposed. The advantage of these emerging photovoltaic technologies is the use of earth-abundant low-cost materials that can be processed from the solution-based approach, enabling the application of large-scale reproduction techniques to reduce the manufacturing costs and the energy payback period. Amongst them, dye (DSSC) and perovskite solar cells(PSC), imitating Nature's amazing energy conversion mechanism of photosynthesis, have gained notable attention. The basic principles of DSSC, as well as PSC and how such a system can offer a cost-efficient solution to convert the freely available solar energy into useful electric energy, are discussed in the posterior portion of this chapter.

1.1 Basics of solar energy conversion

The "photovoltaic effect" is the basic physical process through which a solar cell converts sunlight into electricity. In 1839, the photovoltaic effect was discovered by Edmond Becquerel, when he was experimenting with illuminated metal electrodes in an electrolyte [4]. This concept of converting sunlight into electricity has opened a novel domain of alternative energy generation. In 1883, the first working solar cell was produced using selenium and gold by an American inventor, Charles Frits. In 1905, theoretical work on photovoltaic effect was explained by Albert Einstein. He proposed that electrons are emitted from a solid due to the absorption of "light quanta" now called photons [5].

After a century of innovation, the technology has become so broad that it has engendered a field of interest of its own. Traditional solar cells, made from silicon, are usually p-n junction solar cells and are generally the most efficient. The thin-film solar cells are made from amorphous silicon or cadmium telluride, CIGS, allowing the layers of semiconductor materials to be only a few micrometers thick [6]. Various semiconductor materials (for absorbing the light) and device architecture concepts have been developed with the aim of increasing conversion efficiency. However, a great boost in the efficiency is compromised by the excessive cost of devices. The highly efficient PVs (mainly multi-junction solar cells) are prohibitively expensive. Moreover, most dominant technologies in the market (i.e., crystalline or poly-Si) achieve 25% efficiency in the laboratory, while less than 20% is obtained from commercial devices. In a very interesting recent development, the organo-metal halide perovskite-based solar cell ($CH_3NH_3PbI_3$) was reported to yield 22.1% efficiency [7]. Beyond that, the research trends have been widespread, mostly based on material development. One of the main research and development directions is to find cheaper and effectual absorbers. Other efforts focus on developing alternative device concepts, such as perovskite solar cell, multi-junction, and tandem solar cells. Reducing the "fundamental" losses is one of the main research goals, which remains very challenging.

As mentioned previously, the amount of Sun's energy that reaches the Earth's surface every minute is equivalent to the amount of energy the world's population consumes in a year. The power density from the Earth's surface is given by solar constant 1353 ± 21 W.m^{-2}, declining to around 1000 W. m^{-2} on average at the Earth's surface, as it is attenuated by absorption in the atmosphere. Fig 1.1 compares the extra-terrestrial solar spectrum Air-Mass 0 (AM 0G) to the standard terrestrial AM 1.5G spectrum, which is used as a standard reference for the solar cell efficiency measurement and corresponds to a solar incident angle of 48 degrees relative to the normal surface.

The spectral distribution of solar radiation also depends on the attenuation. In practice, various solar spectra can be measured at the Earth's surface and the degree of attenuation is variable. The most important parameter determines the solar irradiance under clear sky conditions and the sunlight has to travel distance through the atmosphere. This distance is the shortest when the sun is at the zenith, i.e., directly overhead. The ratio of an actual path length of sunlight corresponding to this minimal distance is known as the optical air mass (AM). When the sun is at its zenith, the optical air mass is unity and the radiation is described as air mass one (AM 1) radiation. When the sunlight is at an angle to the zenith, the air mass is calculated using the following expression:

$$AirMass = (Cos\Theta)^{-1} \tag{1.1}$$

where Air Mass (AM) corresponds to the degree to which the atmosphere affects the sunlight received at the Earth‘s surface. The factor behind pertains to the length of the path when the light passes through the atmosphere.

Fig 1.1 depicts the main loss mechanism in solar cells. It shows the maximum achievable energy of solar cells in relation to the spectrum characterizing the sunlight. Photons carrying a specific energy can only generate one electron-hole pair even if their energy is higher. The energy above the band gap level is lost in thermalization of the hot carriers, i.e., through heat. Photons with energies lower than the band gap cannot generate an electron-hole pair. These two losses account for about 50% of the power carried in the Sun spectrum [8].

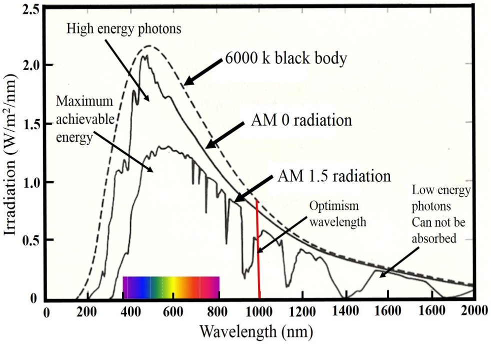

Figure 1.1: Spectral losses and maximum achievable energy of three generations of solar cells in relation to the sun spectrum (AM 1.5).

1.2 Basic structure of a solar cell

Solar cells are made of semiconducting materials that can convert incident sunlight into electricity. In the solar cell, semiconducting materials (like silicon, CIGS/CZTS, dye, and perovskite) are used as a light absorber and the absorption process generates an electron in the conduction band, i.e., an electron from the valence band is transferred to the conduction band, leaving behind a hole in the valence band. The semiconducting materials prevent the reverse process (in which the excited carrier recombines to its ground state) from taking place. Such recombination would transfer the excitation energy of the electron into the excitation of a photon, which transfers its energy to another already excited electron. When the contacts are connected via an external circuit, the cell can produce work at an external load. Mostly, solar cells are based on semiconductor p-n junctions, forming this most widely studied system. In the present study, the maximum conversion efficiency of a photovoltaic device is discussed in relation to this system.

Properties of a p-n junction: Typical solar cells are based on p-n junctions. The p-n junction can be formed by two different semiconducting materials or diffusing donors into a p-type substrate such that a layer of semiconductor is converted into n-type. The non-equilibrium caused by the diffusion of holes to the n-region and electrons to the p-region generates the space charge region between the p- and an n-type semiconductor, as shown in Fig 1.2. The measured open circuit voltage (V_{oc}) at the contacts is given by the difference in quasi-Fermi energy of the electrons in the conduction band (E_{FCB}) and in the valence band (E_{FVB}) [9], as given below:

$$eV_{oc} = E_{FCB} - E_{FVB} \tag{1.2}$$

where e is the elementary charge, (E_{FCB}) is the quasi-Fermi level for the electron distribution in the conduction band (CB), and (E_{FVB}) is the quasi-Fermi level for the electron distribution in the valence band (VB). The energy band diagram of a p-n junction under illumination is shown in Fig 1.2.

Maximum solar energy conversion efficiency in a p-n junction: Shockley-Queisser limit or detailed balance limit refers to the calculation of the maximum theoretical limit of the efficiency of an ideal solar cell. It was first calculated by William Shockley and Hans Queisser in 1961 [10]. The following assumptions are made for a semiconductor with band gap Eg:

- Every incident photon with energy greater than the bandgap, h$\geq$Eg, produces an electron-hole pair.
- The only recombination mechanism of electron-hole pairs is radiative. The maximum photo-current is determined by the difference between the absorbed radiation and the emitted radiation.
- The difference in quasi-Fermi levels of the charge carriers at the point of generation is the same as that at the external contacts (no series resistance in the device).

These conditions allow finding an expression for the maximum conversion efficiency as a function of the band gap, denoted as η_{max} (E_g).

Thus, the maximum theoretical limit for the efficiency of single p-n junction solar energy converters referred to as the detailed balance limit of efficiency, is calculated by the amount of electrical energy extracted per incident photon. The calculation places maximum solar conversion efficiency at about 33.7% assuming a single p-n junction with a band gap of 1.4 eV (Fig 1.1 and Fig 1.3). Therefore, an ideal solar cell with incident solar radiation will generate 337 W.m^{-2}. When the solar radiation is modeled as 6000 K blackbody radiation, the maximum efficiency occurs at the band gap energy of E$_g$ = 1.4 eV [11, 12].

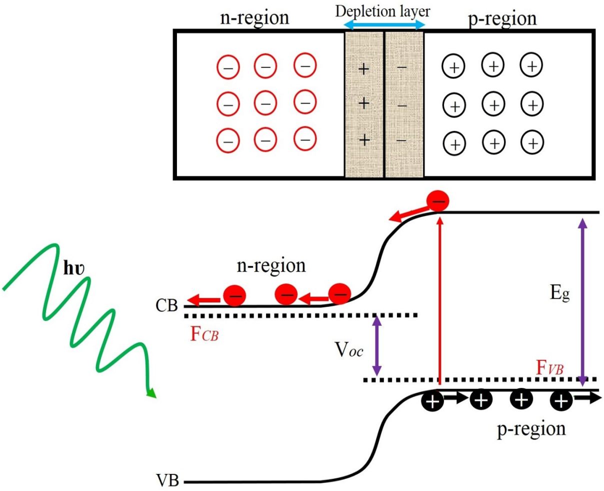

Figure 1.2: Schematic representation of a p-n junction in equilibrium and Energy band diagram of a p-n junction under illumination.

The efficiency can be increased beyond the single-junction limit by multi-single-junction solar cells using the hybrid materials such as tandem solar cells. High-energy photons are absorbed by the top cell and the transmitted lower energy photons are successively absorbed by the bottom cells. Such devices are called multifunction solar cells. The maximum efficiency increases to about 45% by a double junction, with 51% reported for a triple junction, and approaches the thermodynamic limit of 85% for an infinite number of junctions. The losses in real devices are mainly due to reflection, non-radiative recombination of electron-hole pairs, and ohmic losses [13, 14].

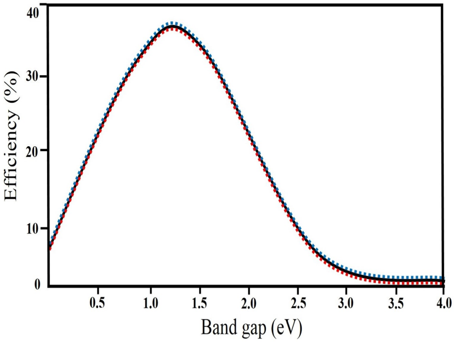

Figure 1.3: Calculated maximum conversion efficiency for AM 1.5G illumination of a p-n junction as a function of its band gap (eV).

1.3 Generations of solar cells

Solar cells are categorized into three generations based on their performance and cost-effectiveness. The first generation of solar cells has a relatively higher efficiency (15-25%) and good stability, albeit at a very high production cost. They are the classical example of solar cells in which photo-generated electron-hole pair is separated and collected through the p-n junction of a doped semiconductor, mainly silicon. The commercial market is dominated by this generation. Single crystalline silicon solar cells are expensive and, in order to reduce their cost, multi-crystalline silicon, and ribbon-silicon based PV modules have been developed [12]. However, the cost of solar electricity is still high and is not competitive relative to that of conventional electricity.

Thin film solar cells based on CdTe or CIGS comprise the second-generation cells. They have a lower efficiency (10-20%) but are much cheaper to produce and require a less extensive fabrication process (and thus limit the use of toxic materials). By employing thin film technology, the cell thickness has been reduced from the millimeter range down to just a few microns, reducing the production cost to just $ 0.50 per Watt in 2011, as shown in Fig 1.4. However, as the manufacture of second-generation solar cells still necessitates vacuum processes and high-temperature treatments, large energy ingestion is still associated with the production of these solar cells [12]. Further, the 2^{nd} solar cells are based on scarce elements and this is a limiting factor in the price. Laboratory efficiencies for small-area devices are approaching 20% and large-area modules have reached 15%, as shown in Fig 1.5.

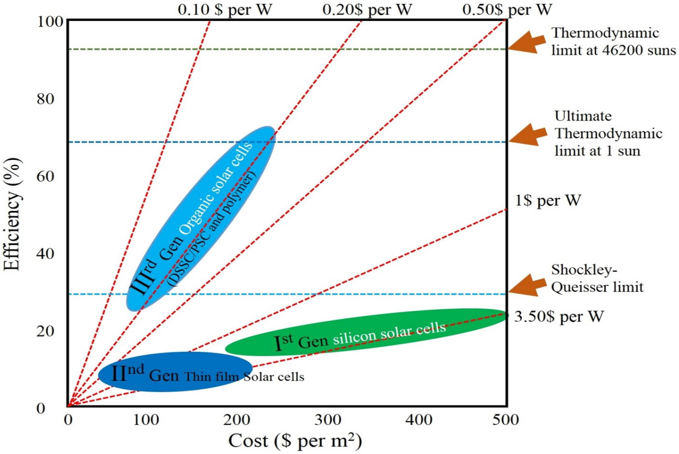

Figure 1.4: Efficiency-cost trade-off for the three generations of solar cells.

The drawback to the 1^{st} and 2^{nd} generation of solar cells is that they are limited by the Shockley-Queisser theoretical limit of ∼30% for a single p-n junction. The 3^{rd} generation solar cells consist of any cells that are not classified into these two groups. They employ a variety of different technologies and are not restrained by the Shockley-Queisser limit, as shown in Fig 1.4. While most of the third-generation technologies are not yet commercially available, extensive research is being conducted in this field, with a promising future. Dye and perovskite and organic solar cells are classified as 3^{rd} generation and carry lower cost compared to the first and second generation. Although the concert and stability of 3^{rd} solar cells are still limited compared to those classified into the first two generation, they have a great potential and are already commercialized. Research interest in PSCs has increased significantly in recent years and it is now possible to produce them at a price that enables projects such as the free OPV initiative. Fig 1.4 shows the history and current achievements of photovoltaic research in different categories throughout the world.

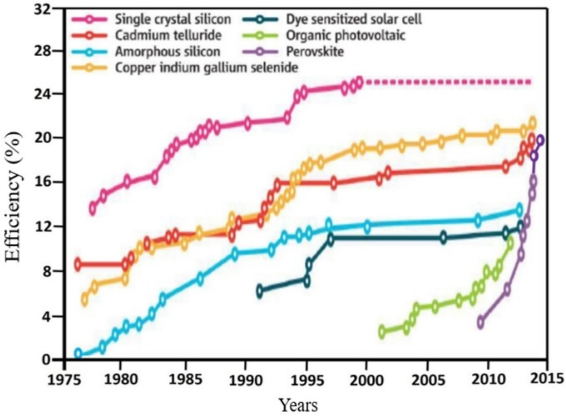

Figure 1.5: Comparison of reported efficiencies for various solar cells.

1.4 Dye-sensitized solar cell

Dye-sensitized solar cell (DSSC) is an attractive solar energy conversion technology and its advantages include low cost of manufacture and ease of fabrication. It was first introduced by Gratzel in 1991 [15]. However, the working principle of DSSC is differed from other organic solar cells, with respect to charge carrier generation and transport mechanism. Fig 1.6 shows the schematic diagram of DSSC. By employing a dye-sensitized, wide band gap semiconductor as a photo-anode, the two fundamental processes-photon absorbtion and carrier transport are separated from each other. Therefore, bulk properties of the semiconductor exhibit less influence on the device performance and thus device comprising of low-grade materials yields reasonable efficiency. Apart from industrial perspectives, DSSCs are emerging as an ideal model system to study the fundamental issues, such as ultra-fast electron injection and transport in nanocrystalline semiconductor electrodes.

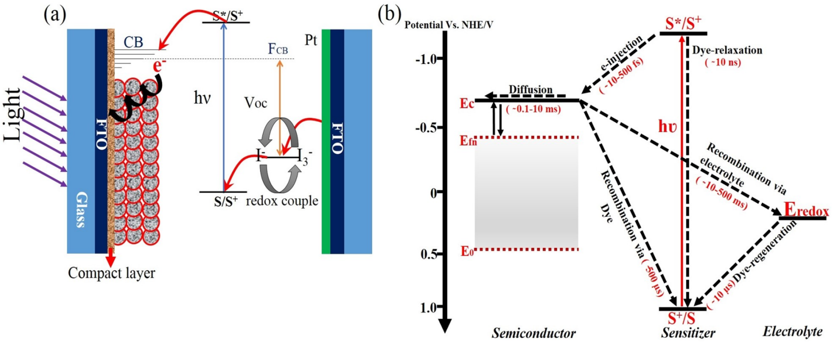

Figure 1.6: (a)Schematic representation of electron injection, and (b) energy level diagram of DSSC.

1.4.1 Device structure

A DSSC, the Gratzel cell that was designed by Gratzel and O'Regan at the EPFL, is a new class of low-cost solar cell belonging to the group of thin film solar cells. DSSC consists of three primary parts. The working electrode is composed of a mesoporous layer of TiO_2 covered with a dye mono-layer. Platinum (Pt) is used as a counter electrode of the cell. Between the two electrodes is the electrolyte, which contains a redox couple. The two glass substrates (photo-anode and a counter electrode) are coated with fluorine-doped tin oxide (FTO) to harvest light into the cell and to collect electrons. The space between the photo-electrode and the counter electrode is filled with a liquid type electrolyte for electron transfer into the cell. Therefore, an appropriate sealing method is required to prevent the liquid electrolyte leaking out. In this approach, attached dye molecules (N719), rather than the TiO_2 itself, are the absorbing species. They inject electrons into the TiO_2 conduction band upon excitation. These electrons are collected at the conducting surface of the FTO, generating photocurrent [15, 16], as shown in Fig 1.7.

1.4.2 Operating principle:

A porous nanocrystalline TiO_2 layer prepared on FTO substrate serves as a base for the DSSCs. The monolayer of sensitizing dye molecule is chemically adsorbed onto the TiO_2 layer and acts as a light absorber. Upon illumination, electrons are injected from the photoexcited dye into the conduction of TiO_2, while hole moves towards the counter electrode through iodide/tri-iodide redox couple electrolyte. After performing the work in the external circuit, electron enters the cell through the counter electrode and reduces the number of tri-iodine ions, thus completing the electrical circuit [16].

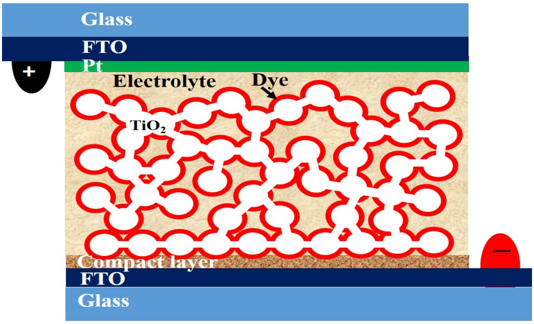

Figure 1.7: Schematics cross-sectional view of the dye-sensitized solar cell configuration: FTO glass, compact TiO_2 underlayer, mesoporous TiO_2 with N719 dye, electrolyte, and counter electrode.

1.4.3 Charge carrier generation and transport

In DSSCs, excitons are generated at the hetro-interface between the dye attached TiO_2 layer and redox electrolyte. The lack of exciton diffusion and ultra-fast injection of electrons into the TiO_2 conduction band makes DSSC more efficient than any other excitonic solar cell [17]. Fig 1.6(a) schematically describes the charge carrier generation and transport in dye-modified TiO_2 layer. The TiO_2 electrode serves as a support for the dye molecule, as well as a conductive pathway between the site of electron injection and collection. Electron transport in the TiO_2 layer is believed to occur by diffusion since nanometer (nm) size of the particle does not provide support for the drift field. Permeation of redox electrolyte in the mesoporous structure also imposes an electroneutrality. Therefore, transport of electrons results in charge imbalance and creates the electric field, which in turn drags the cations in the electrolyte [18].

1.4.4 Oxidation and reduction of redox couple

The photovoltaic performance of DSSC largely relies on the properties of the redox electrolyte employed to regenerate the dye molecules following the ultra-fast electron injection. For a successful operation of the solar cell, electron transfer kinetics of the redox system must be sufficiently fast at the counter electrode and very slow at the working electrode. Despite the effort to develop an alternative redox system including solid state hole conductors, the best efficiencies have been obtained using I^-/I_3^- redox couple. This is attributed to slow electron transfer process from the TiO_2 to I_3^- ions in the electrolyte and regeneration of I^- from I_3^- at the counter electrode [19, 20], as shown in Fig 1.6(a).

1.5 Perovskite solar cell

The high-efficiency perovskite solar cell was designed by Miyasaka and is a new class of low-cost solar cell that belongs to the group of thin film solar cells. The first PSC prototype was realized with the structure of a DSSC in 2009 with the perovskite absorber replacing the N719 dye and liquid electrolyte [21]. The name perovskite derives from the crystalline structure of the absorber materials: ABX_3 the organo-lead halide ($CH_3NH_3PbI_3$) compound obtained from a simple synthesis and deposited through conventional solution process techniques.

1.5.1 Perovskite structure and properties

The latest and the most exciting development in the field of solid state solar cells utilizes a novel material from the perovskite class that has many beneficial properties. Perovskite originates from the discovery of calcium titanium oxide ($CaTiO_3$) by the Russian mineralogist Lev Perovski. Later, several materials with the same crystal structure were created. More generally, perovskite refers to AMX_3 crystals, where A is a cation, M a metal cation, and X denotes an oxide or a halide anion. AMX_3 extended as a 3D structure formed by an MX_6 corner-sharing octahedron is shown in Fig 1.8. AMX_3 has cubic geometry; however, the lattice is never ideal and can exhibit distortions that will affect optical and physical properties of the crystal. Moreover, the size of cation and metal-ion (M) will influence the lattice structure and will be a critical parameter for modulating the electronic and optical properties of the material. The organic (CH_3NH_3) group usually contains an alkyl chain or a single-ring aromatic group. In addition, these materials can be easily prepared by the solution-based approach, which offers potentially low-cost and lower temperature processes for materials preparation [21]. Herein, the focus is mainly on the family of lead halide perovskites ($CH_3NH_3PbX_3$), where X = I, Cl, or Br, and more specifically on $CH_3NH_3PbI_3$ (crystal structure is shown in Fig 1.8). One peculiarity of the perovskite containing small organic cations is that the $CH_3NH_3{}^+$ is free to rotate in the lattice [22, 23].

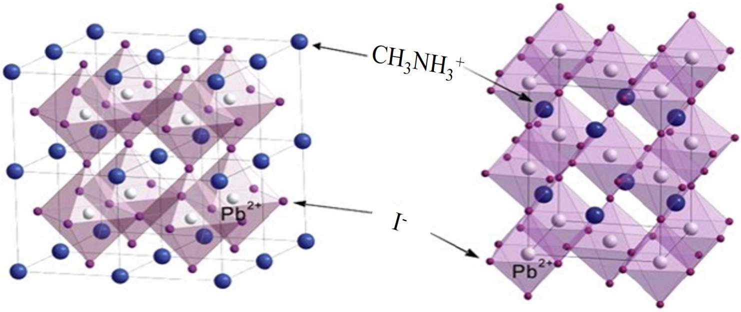

Cubic $CH_3NH_3PbI_3$ **Tetragonal $CH_3NH_3PbI_3$**

Figure 1.8: Crystal structure of $CH_3NH_3PbI_3$.

Optical properties: Organic-inorganic halide perovskites (AMX_3) have interesting optical properties mainly because of their direct band gap that can be tuned either by changing the alkyl group ($A= HC(NH_3)_3{}^+$, $CH_3NH_3{}^+$), the metal atom (M= Pb, Sn) or the halide (X = I, Cl and Br). The perovskite materials ($CH_3NH_3PbI_3$) have direct band gap (E_g) and a value of $E_g = 1.54$ eV was reported for $CH_3NH_3PbI_3$ deposited on mesoporous TiO_2. The position of the valence band energy (E_{VB}) was estimated at -5.43 eV below the vacuum level, confirmed by Schulz et al [24]. Thus, from the optical bandgap, the position of the conduction band can be estimated at E_c=-3.93 eV vs.vacuum. Perovskites usually exhibit sharp resonances in their room-temperature optical absorption spectra, which arise from an exciton state associated with the inorganic semiconducting layers [25, 26].

Electronic properties: Organic-inorganic halide perovskites (AMX_3) have interesting electrical properties. In their study, Stoumpos et al. reported electron mobility for two different lead (Pb) and tin (Sn) metal atom-based perovskites, as determined through Hall effect and resistivity measurements. They found electron mobilities of 2320 cm^{-2} $V^{-1}s^{-1}$ for $CH_3NH_3SnI_3$ and 66 cm^{-2} $V^{-1}s^{-1}$ for $CH_3NH_3PbI_3$. These values are remarkably high and are comparable to those of classical semiconductors like Si (1400 $cm^{-2}V^{-1}s^{-1}$) [27]. The authors also pointed out that the very low carrier concentrations measured are indicative of nearly intrinsic semiconductors. Effective diffusion lengths for $CH_3NH_3PbI_3$ as measured in solar cell architecture are discussed more extensively in the following paragraph.

It is important to the discussion that some significant differences between the iodide-based perovskite and the mixed halide $CH_3NH_3PbI_3 - xCl_x$ are noted. Diffusion lengths of 100 nm for electrons and holes were reported for iodide-based perovskite, while electron and hole diffusion lengths in mixed halide $CH_3NH_3PbI_3 - xCl_x$ were found to be one order of magnitude higher, exceeding 1μm [28]. Other reports support the finding that a small amount of chlorine (Cl) doping dramatically improves the charge transport properties without changing its optical properties. Due to the presence of a $CH_3NH_3{}^+$ cation and a $PbX_3{}^-$, $CH_3NH_3PbI_3$ can be considered as an ionic compound with a permanent electric dipole moment. For this reason, its dielectric constant is relatively high and was initially estimated at 6.5 but recent reports suggest even higher values, up to 30. The high dielectric constant also explains the low binding energies of the exciton, since the photo-induced charges can be effectively screened by the dipoles of the lattice [29].

1.5.2 Perovskite in photovoltaic devices

The use of organic-inorganic halide perovskite (AMX_3) materials used in devices for light energy conversion was reported by Miyasaka and coworkers in 2009. These authors employed perovskite nanocrystals as a replacement for the conventional dye-sensitizer in DSSCs. They measured a relatively low power conversion efficiency (PCE) of 3.8% and 3.1% in AMI_3 and $AMBr_3$ based solar cells, respectively. Interestingly, a very high V_{oc} was reported, up to 960 mV, achieved with the lead bromide-based solar cell, which is an impressive value. Soon after, the PCE was raised to 6.5%, as reported by Im et al [30]. Replacing the liquid electrolyte with a solid hole conductor material (HTM) solved the immediate instability problem of the perovskite-based solar cells and increased their efficiency. Record efficiencies of 9.7% have been achieved for $CH_3NH_3PbI_3$ deposited on TiO_2 mesoporous structure, while in the same period Lee et al [31]. reported PCE of 10.9% for a supposedly mixed halide $CH_3NH_3PbI_3-xCl_x$ deposited on aluminum oxide (Al_2O_3), where no extraction of the charges in the mesoporous oxide is possible [32]. Due to the high J_{sc} (20 $mA.cm^{-2}$) and V_{oc} (1000 mV), these two works have attracted the attention of a very large scientific community, prompting the development of many studies using these perovskites in However, these cells suffered from a major drawback, as they were decomposing very rapidly, typically 80% degradation would occur after 600 seconds of illumination, due to the dissolution of the perovskite in the liquid electrolyte photovoltaic architectures, as shown in Fig 1.9.

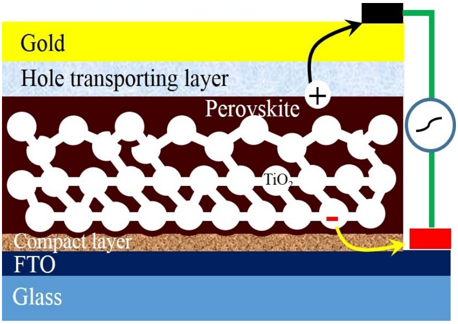

Figure 1.9: Schematics cross-sectional view of the perovskite solar cell configuration: FTO glass, compact TiO_2 underlayer, mesoporous TiO_2 with infiltrated $CH_3NH_3PbI_3$, HTM, and gold.

Initially, the preparation route for PSCs consisted of the deposition of a precursor solution containing CH_3NH_3I and PbI_3 in γ-butyrolactone. Recently, a breakthrough in PCE was achieved by using a modified perovskite processing method, called the sequential deposition method, where PbI_2 is first spin-coated from a dimethylformamide (DMF) solution on the TiO_2 film and then successively converted to perovskite by dipping into a CH_3NH_3I solution in isopropanol (IPA) [33]. This new method has led to a PCE of 15% and a certified value of 14.1% with high reproducibility. The last record to date on mesoporous TiO_2 has been certified for a device by a group at the Korean Research Institute of Chemical Technology (PCE = 20.1%) and efficiencies above 19% are reported for research devices at the laboratory scale [34]. Perovskite layers on flexible substrates (PET) have also been reported, paving the route for numerous types of applications of these photovoltaic devices.

1.6 Aligned nanostructure for dye and perovskite solar cells

Aligned nanostructure (1D, 2D, and 1+2D = 3D) arrays, with two quantum confined directions and one unconfined direction in order to conduct electrons, is shown in Fig 1.10. It should be noted that aligned nanostructures differ from bulk materials owing to their single crystalline and grain boundary-free nature, increased surface area to volume ratio, very high density of electronic states, enhanced exciton binding energy, diameter-dependent band gap and increased surface scattering for electrons and phonons.

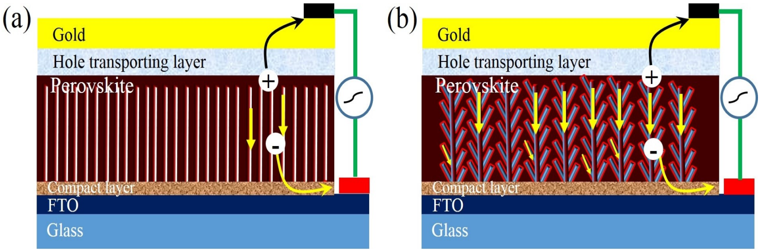

Figure 1.10: Schematic of electron transport in (a) 1D nanowire, and (b) hybrid nanostructure-based perovskite solar cell.

The problems of the 3D nanostructure (nanoparticles) of TiO_2 or ZnO in electron moment arise due to random drift mode and much slower charge transport. Compared to the 3D and 2D, the 1D nanostructure has a low surface area and faster electron transport. The charge transport can be increased and the recombination rate of vertically aligned 2D nanostructure-based photoanode reduced by doping or hybrid structure. The conductivity of photoanode increases with doping, without augmenting the surface area of the electrode. The hybrid nanostructure has a high surface area and enables fast charge transport owing to the reduced diffusion paths for electrons. This increase in efficiency could be attributed to the combined effects of the charge-carrier concentration, reduced recombination process and changes in morphology, which are proportional to the electrode surface area. As a consequence, overall efficiencies of the nanowire, as one of the hybrid nanostructure PSCs, could potentially surpass those of nanoparticle-based PSCs.

1.7 Motivation

High-efficiency solar cells are an attractive solar energy conversion technology and their advantages include low cost of manufacture. The first dye and perovskite solar cells were introduced by Miyasaka and coworkers. Metal oxide nanoparticle are usually employed as electron transport in third generation solar cells. Although nanoparticles provide large surface area for anchoring the absorber materials, the poor networking and interparticle connectivity limiting the efficient transport of photo generation charge carriers (e^-). Replacing the conventional nanoparticulate of metal oxide film by aligned metal oxide nanostructures may improve the electron transport. Furthermore, the absence of interparticle continuity grain boundaries are expected to minimize the carrier recombination. However such efforts always accompanying the reduction in specific area of the photo anode. In this context, growth of aligned 3D nanostructre may provied high specific surface area for anchoring the absorbers, and also provide the direct path for the transportion of photogenerated carriers. Realizing such effoerds by low temperture solution base approch may further enchace the technical viablity of next generation solar cells. Such aligned three dimensional (3D) ZnO nanowall architecture, with the unique combination of high surface area and cage-like pores, grown on seed layer coated transparent conductive substrate is beneficial for the electron transporting material (ETM) in dye and perovskite solar cells.

1.8 Outline of the thesis

This thesis comprises of four chapters. **Chapter 1** provided a brief introduction of solar cells, structure and working principle of dye and perovskite solar cells, as well as the transport process in 3D and hybrid nanostructure-based dye and perovskite solar cells, which is one of the key processes in the cell operations.

Chapter 2 presents a review of the pertinent literature discussing dye and perovskite solar cells, as well as the problems associated with 3D nanostructure (nanoparticles) of TiO_2 or ZnO in electron moment, namely random drift mode and much slower charge transport. TiO_2 nanoparticle layer used for electron transport in solar cells can substituted with dense arrays of aligned ZnO nanostructures. The synthesis methods for aligned ZnO nanostructures on the arbitrary substrates by the hydrothermal method are also presented.

In **Chapter 3**, details of synthesis and experimental techniques employed in this work are reported in detail. The description of the characterization apparatus is also given briefly.

Chapter 4.1 is designated to the discussion of a novel non-vacuum route for uniform deposition of a ZnO seed layer on large-area FTO substrate. Aligned ZnO nanowires were grown on the aforementioned substrate by a hydrothermal method. It is demonstrated that the alignment, diameter and aerial density of the ZnO nanowires are significantly influenced by the characteristics of the underlying ZnO seed layer and the photovoltaic properties. In **Chapter 4.2**, the influence of spray coated seed layers on vertical alignment and electrical properties of ZnO nanowire arrays are presented. **Chapter 4.3** provides details of the ZnO nanostructure growth mechanism dependent on the seed layer characteristics. It has also been found that microstructural features of grown nanostructures are largely influenced by the seed grain sizes. In **Chapter 4.4**, it is shown that by adding a controlled amount of Al into the ZnO seed layer, the morphology of the ZnO nanostructure is gradually changed from 1D nanowire to 3D nanowall arrays. Such aligned 3D ZnO nanowall architecture, with the unique combination of high surface area and cage-like pores, grown on seed layer coated transparent conductive substrate is found to be beneficial for the ETM in dye and perovskite solar cells. Large internal voids of aligned 3D ZnO nanowall arrays were successfully functionalized with ZnO nanowires, thereby improving absorber loading and photocurrent. Thus, in **Chapter 4.5**, graphene is described, as an alternative material for the counter electrode in the dye and perovskite solar cells.

Chapter 5 presents the conclusions yielded by this investigation, along with some future outlooks for this research field.

Chapter 2

Literature review

This chapter presents the review of extant literature on the growth of aligned ZnO nanostructures on FTO substrates and their application as electron transport layer in dye and perovskite solar cells. The dye-sensitized solar cells became one of the most promising solar cells in the energy research and industrial field due to their high efficiency, low-cost materials, and efficient manufacturing. In this device, TiO_2 is used as a scaffold for sensitizers, as well as to provide efficient electron transfer [15]. In this chapter, studies describing the device structure and operation mechanism are reviewed. With the aim of improving electron transport, in this work, the TiO_2 is replaced by high electron mobility semiconductor ZnO, while dye-liquid electrolyte is replaced by perovskite.

Wide bandgap semiconductor materials have been extensively used in optoelectronic devices, due to their high electron mobility, chemical stability, non-toxicity and inexpensive production cost [15, 35]. The DSSC consists of a dye-adsorbed TiO_2 layer as a working electrode, platinum coated TCO as a counter electrode and liquid electrolyte containing $I^-/I_3{}^-$ redox couple as p-type hole transport. Once the light is incident on the device, dye molecules are excited and inject the photoexcited electrons into the photoanode conduction band. The photoanode conduction band edge level is lower than that of the light harvesting materials, such as dye for effective injection of electrons [19, 36], as shown in Fig 2.1(a). Basically, nc-TiO_2 is porous and transparent to the visible light, resulting in a considerable part of light incident on the DSSC being transmitted through the TiO_2 layer without interacting with the sensitizer. Consequently, the photoinjected electrons may recombine with I_3^- species in the redox electrolyte. The electron recombination without light interacting with sensitizer will cause the loss of photocurrent, substantially decreasing the photovoltaic performance of DSSC [37, 38].

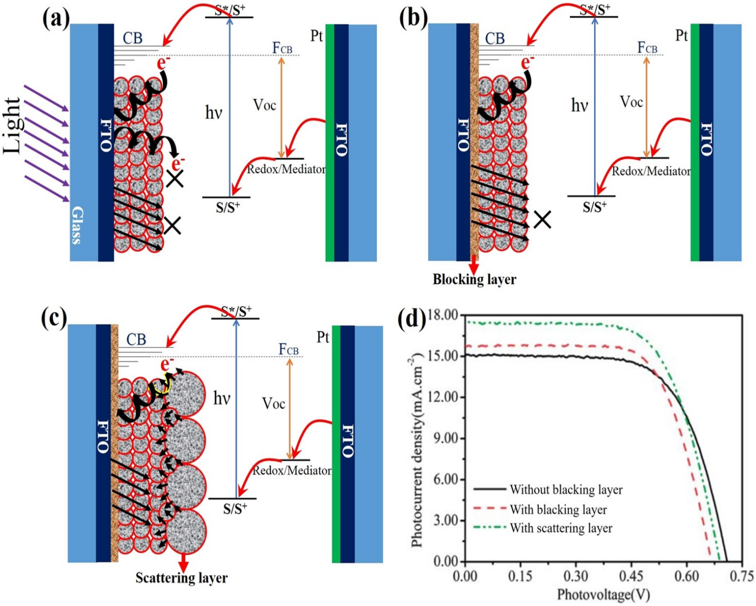

Figure 2.1: Schematic diagram of the DSSCs (a-c) without and with blocking, scattering layer and (d) corresponding I-V characteristics.

To overcome this problem, Gratzel group developed a light scattering layer over the nc-TiO_2 layer, the primary purpose of which was to increase light absorption by extending the effective path length of light traversing through the cell. Therefore, enhancing light harvesting or absorbance within the photoanode of DSSCs is essential for obtaining high-performance DSSCs [39, 40], as shown in Fig 2.1(b). This work has attracted extensive interest, resulting in important progress towards improving the performance and understanding of this novel photovoltaic device. According to Peter et al., the blocking layer of TiO_2 can improve the DSSC performance, as it provides good adhesion between the

FTO and the nanocrystalline layer of TiO_2. Thus, it blocks the electron back-transport between the electrolyte and the FTO by preventing direct contact. The resulting blocking layer thickness of around 100 nm is deemed sufficient to prevent the direct electron transfer from the TCO to the redox mediator. This blocking layer is necessary for the solution-phase redox mediators [38], as shown in Fig 2.1(c). The scattering/nc-TiO_2/blocking layer (SNB-TiO_2) based DSSC, which has a high surface area for dye adsorption and electron energy level matching, allows for the injection of carriers from dye to TiO_2. The main drawback of SNB-TiO_2 based photoanodes is that their many inter-particle boundaries easily trap charge carriers, which results in a decrease in the carrier mobility and transport, and shortens carrier lifetime. Empirical evidence suggests that 12-14 μm thickness is optimal for obtaining the highest efficiency [41-43], as shown Fig 2.1(d).

The nanoparticles are advantageous in providing a high surface area. However, the existence of many boundaries in the nanocrystalline layer has been regarded as an unfavorable factor that may increase interfacial charge recombination occurring between the photo- generated electrons and the positive species in the electrolyte. Employing 1D nanostructures in DSSCs is one of the means of overcoming this problem. This approach is based on the premise that 1D nanostructures, such as nanowires and nanorods, can provide direct pathways for electron transport from the electron injection site to the conducting film of the collector electrode [43-45]. As such, it is expected to achieve faster electron transport than in the nc-TiO_2 layer. This has been evidenced by experiments, which reveal that the electron transport in photo-electrode comprised of single crystal nanowires is even 100 times faster than that in the case of the nc-TiO_2 [46]. Fast electron transport may lower the opportunity for photogenerated electrons to react with the positive species in the electrolyte and, therefore, significantly suppresses the interfacial charge recombination [43, 47]. Aligned nanostructures have demonstrated a great potential to achieve a high diffusion coefficient of carriers in electric devices due to their unique 1D, and 2D structures, as shown Fig 2.2.

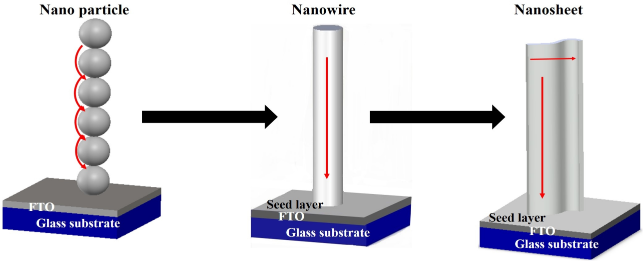

Figure 2.2: Schematic of electron transport in (a-c) 3D, 2D, and 1D nanostructures.

Furthermore, in order to improve the electron transport in DSSC, the TiO_2 photo-anode can be replaced with ZnO. ZnO has attracted great attention owing to its significant electric and optical properties. This interest is prompted further by the extensive use of ZnO in optoelectronic applications. While ZnO has been extensively studied for years, detailed investigations of its novel semiconducting properties commenced in 1950s. In 1960s, numerous studies of band structure, as well as excitonic and electrical transport properties of ZnO, were carried out. Their findings indicate that ZnO can be a good competitor to TiO_2 due to their similarities in wide-band gap and higher electron mobility conditions (130-200 $cm^2.V^{-1}s^{-1}$) [46, 48]. In addition, ZnO has a larger exciton binding energy ($\sim$ 60 meV for ZnO, 60 meV for TiO_2 (anatase)). In addition, it is abundant and can be produced through simpler and more cost-effective crystal growth methods compared to TiO_2. ZnO has three different crystal structures, namely rocksalt, zinc blende, and hexagonal wurtzite, as shown in Fig 2.3. The wurtzite crystal structure is chemically and thermodynamically stable in ambient atmospheric conditions [49]. Ideally, this wurtzite ZnO unit cell is hexagonal and has two lattice parameters a and c with the ratio of c/a $=$ 1.633, and the structure's space group is P_63_mc. The wurtzite structure can be described as a number of alternating tetrahedrons composed of coordinated O^{2-} and Zn^{2+} ions, stacked alternately along the c-axis. One zinc ion is surrounded by four oxygen ions in a tetrahedral unit cell and vice versa. The polar surfaces are another important characteristic of the ZnO wurtzite structure. Spontaneous polarization along the c-axis and a normal dipole moment are produced by oppositely charged Zn-(0001) and O-(0001) surfaces. Usually, the polar surfaces have facets for exhibiting surface reconstruction to maintain a stable structure. Moreover, the planes (0001) in ZnO wurtzite structure are atomically static and without reconstructions [50-52]. The reason for the stability of ZnO is still not fully understood and is currently at the forefront in surface physics research.

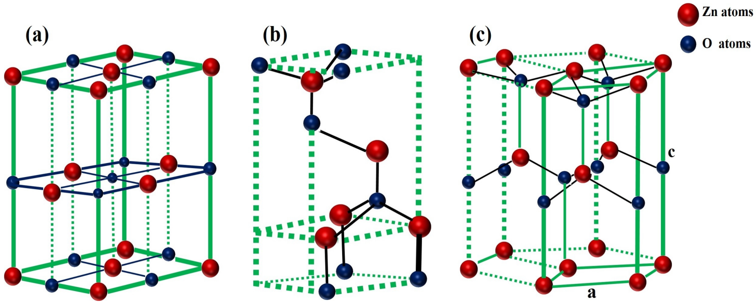

Figure 2.3: ZnO crystal structures: (a) cubic rocksalt, (b) cubic zinc blende, and (c) hexagonal wurtzite.

To grow aligned ZnO nanostructures, such as nanowire, various growth methods can be adopted, including vapor-phase deposition, molecular beam epitaxy (MBE) and pulsed laser deposition that provides aligned ZnO nanostructure. However, these approaches require high-temperature, insulating and/or low-transmittance epitaxial substrates and a metal catalyst, limiting their technical viability in optoelectronic applications [53, 54]. Aligned ZnO nanostructures can be synthesized by various low-temperature solution processes, such as chemical bath deposition, electrochemical deposition, and hydrothermal method. However, a hydrothermal method is the most inexpensive process for obtaining uniform and high-quality aligned ZnO nanowires on arbitrary substrates. Vayssieres developed a low-temperature solution process for growth of aligned ZnO nanostructures on TCO substrates. Aligned ZnO nanostructures were realized by introducing a compact layer of ZnO seeds on top of the TCO substrate [55]. The seed-free growth of aligned ZnO nanostructure is very difficult to achieve on TCO substrates, because of the lattice mismatch. A seed layer is essential in order to achieve aligned nanostructure on the substrate [56, 57]. Recently, numerous seed layer deposition techniques have been used for growth of aligned ZnO nanostructures, such as atomic layer deposition (ALD), pulsed laser deposition (PLD), RF sputtering and spray coating [58, 59]. Spray coating can be used as a high throughput non-vacuum technique for uniform deposition of seeds on large area FTO substrates. Aligned ZnO nanostructures with tunable features, such as diameter and aerial density, have been successfully grown on spray coated ZnO seed layer/FTO substrates by hydrothermal reaction [59].

The aligned ZnO nanostructures grown on the TCO substrate are used as electron transport layer in DSSCs. In 2005, Law et al. successfully grew aligned ZnO nanostructures on FTO substrate that were used as electron transport layer in DSSC, achieving the fill factor of 0.37% and 1.5% efficiency [60]. Seol et al. have grown ultra-long ZnO nanowires on a sputtered seed layer/FTO substrate by a multi-step solution method and have demonstrated a maximum efficiency of 4.15% in quantum dot sensitized solar cells [61]. Akhtar et al. used ZnO with different morphology, including flowers, spheres, etc., as a DSSC photoanode and observed that sheet-sphere ZnO was highly crystalline and had a large surface area to volume ratio. This was reflected in the photovoltaic performance with the overall conversion efficiency of 2.6% in DSSC fabricated with sheet sphere ZnO as compared to others [62]. Aligned ZnO nanostructure typically has a roughness factor of only 10-100, and its PCE is significantly lower than that of a nanoparticle. However, ultra-long aligned ZnO nanostructures with the roughness factor of 500 and DSSC efficiency of 7% have recently been reported by the Gao group. The photocurrent and efficiency increase with nanostructure length, confirming that energy conversion is indeed limited by light harvesting [63]. Moreover, Fu et al. developed aligned hybrid ZnO nanostructures, which not only provide high surface area for dye absorption but also enable fast charge transport due to the shortened diffusion path for electrons [64]. This increase in efficiency could be attributed to the change in morphology of ZnO nanostructures. Gan et al. synthesized hybrid ZnO/TiO_2 electron transport layer for DSSCs by combining ZnO nanowires and TiO_2 nanoparticles with the assistance of the ultrasonic irradiation assisted dip coating method [65]. Xu et al. have established hybrid ZnO nanowire-nanosheet architectures for better dye loading and light harvesting. They reported a PCE of 4.8%, which is nearly twice as high as that of DSSCs fabricated using the ZnO nanosheets [66]. Enhancement in the photovoltaic performance can benefit from the enlargement of the internal surface area within the photo-anode without sacrificing a direct conduction pathway for the rapid collection of photo-generated electrons.

Aligned ZnO nanostructure-based DSSCs were constructed with liquid electrolytes and PCE of 7% with N719 dye. The greatest challenge for DSSC is the need to improve their long-term stability. The stability issues related to temperature, electrolyte leaking and dye degradation could reduce the device efficiency. In contrast, the liquid electrolyte of DSSCs could be replaced with solid-state organic hole transport material (HTM) to minimize the stability issues. The PCE of solid-state DSSCs was relatively lower than that of the conventional liquid ones. The highest PCE reported for solid-state DSSCs is around 6% with spiro-OMeTAD as the organic HTM. Perovskite material ($CH_3NH_3PbI_3$) was first used in solar cells in 2009 by Miyasaka et al. In this work, $CH_3NH_3PbI_3$ was applied as a sensitizer in a DSSC with liquid electrolyte. The perovskite was deposited on top of a TiO_2 coated FTO substrate and the device architecture structure is shown in Fig 2.4. The authors reported the maximum cell PCE of 3.81%, with spectral response covering the entire visible region, up to 800 nm. However, the structure became unstable when exposed to air [21]. Park et al. reported in 2011 a PCE of 6.5% using the similar structure in which perovskite quantum dots were deposited in a one-step solution process on top the TiO_2 layer with liquid electrolyte [30]. The previous reports show that perovskite exhibits better absorption than the N719 dye-sensitizer, whereas the ionic crystal perovskite dissolved in the polar electrolyte resulted in rapid performance degradation. The replacement of the liquid electrolyte with spiro-MeOTAD not only improved the stability of the solar cell but also boosted its efficiency to 9.7% [31]. In the subsequent work, the perovskite layer was prepared by spin coating on a TiO_2 coated FTO substrate before dipping in a cation iodide solution. Uniform coverage and 200-300 nm thick perovskite over TiO_2 was achieved by this deposition technique, and the device efficiency of 15% was reported by the Gratzel group [33]. Kelly and colleagues improved the PCE to 15.7% by $MAPbI_3$ deposition in a two-step deposition on top of compact ZnO instead of compact TiO_2 [67]. Yang's group demonstrated a further increase in PCE to 19.3% by modifying the commonly utilized planar configuration [68].

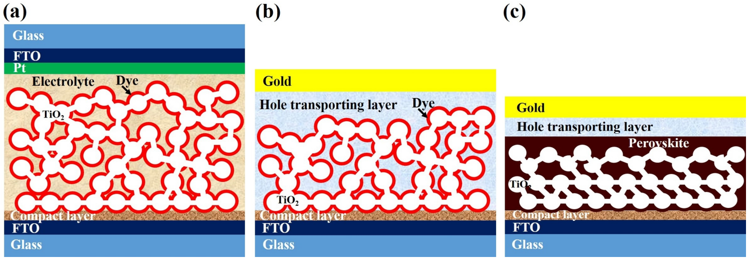

Figure 2.4: Evaluation of perovskite solar cell

A comprehensive literature review related to the aligned ETL in third generation solar cells (DSSC, PSC) is presented in this chapter. Device based on aligned nanostructure, such as optoelectronic application is discussed in detail. Finally, the state-of-the-art development in the aligned ZnO nanostructures by low temperature solution base approach has the merit of low temperature, large scale, and economical synthesis, it has attracted the interest of numerous researchers worldwide is reviewed. This study aims to make use of spray coated seed layer for growth of aligned ZnO nanostructures in DSSCs and PSC to achieve the ultimate goal of producing high efficiency solar cells by a fast and cost fabricate method.

Chapter 3

Experimental Section

In the previous chapter, the background on aligned ZnO nanostructures grown on the transparent conductive substrates was provided and their application as electron transport layer in dye and perovskite solar cells was discussed. Hydrothermal method is the most inexpensive process employed to obtain a uniform and high-quality aligned ZnO nanostructure on seed layer coated substrates. Spray coating was used as a non-vacuum route for deposition of a ZnO seed layer on substrates. The experimental techniques employed for the fabrication and characterization of ZnO nanostructures and ZnO seed layers discussed in this work are briefly described.

3.1 Substrates preparation and cleaning

Optically transparent and electrically conducting substrate is used for electron collecting layer in the 3^{rd}-generation solar cells. The substrate allows visible light to penetrate while blocking the wavelengths in the white light region. The FTO substrates were used for both working and counter electrode because of their relatively stable under atmospheric conditions. In addition, FTO is chemically inert, mechanically hard, high-temperature resistant has a high tolerance to physical abrasion and is less expensive than ITO substrates [69]. The FTO substrate used for all experiments was purchased from Pilkington. Four-point probe measurements revealed a sheet resistance of $R_{sheet} = 12\Omega/\square$. To convert the sheet resistance (R_{sheet}) into the specific resistance (ρ_{FTO}) of this substrate, the layer thickness (d_{FTO}) had to be determined using Eq(3.1).

$$\rho_{FTO} = R_{sheet} \times \mathrm{d}_{FTO} \tag{3.1}$$

$$\rho_{FTO} = 12\Omega/\Box \times 600 = 7.2 \times 10^{-4}.\Omega cm \tag{3.2}$$

The surface morphology of the FTO layer was mostly comprised of sub-micron size F: SnO_2 grains as shown in Fig 3.1(a). Fig 3.1(b) shows the cross-section SEM image of an FTO substrate with the layer thickness of around 600 nm. The specific substrate resistance was calculated using the Eq(3.1).

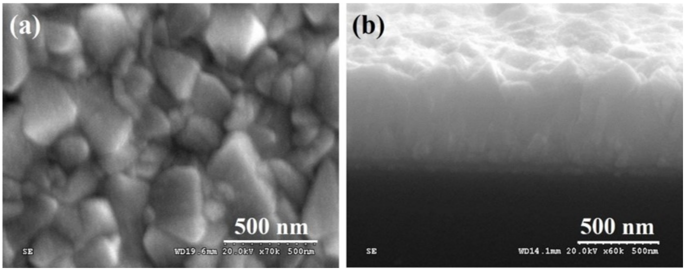

Figure 3.1: Cross-sectional and surface SEM images of FTO film on glass substrate.

The FTO substrates were cut into 15 × 15 mm size pieces from the original size of 30 × 30 cm. To prevent short circuits when contacting the top of the electrodes, some part of the FTO was removed by etching. Part of the FTO layer was etched away by covering the other portion with Kapton tape. Parts of the conductive layer on the FTO substrate were first etched using zinc powder and hydrochloric acid. Then, the tape was removed, and the substrate was cleaned in an ultrasonic bath for 15 min in acetone and ethanol, followed by further 15 min in Di-water, after which the substrates were dried under a nitrogen flow and stored in a dust-free box. These 15 × 15 mm FTO substrates were used for the growth of ZnO nanostructure arrays.

3.2 Hydrothermal growth of aligned ZnO nanostructure arrays

The solution-based approaches are especially attractive for laboratory and industry applications, because of their low cost, low processing temperature, and ease of morphology control. In addition, the process is environmentally friendly [70]. To grow aligned ZnO nanostructure arrays on FTO substrates, a seed layer reduces the lattice mismatch between the ZnO nanostructures and a substrate, allowing the growth of aligned nanostructures on the substrate [55]. The seed layer, composed of ZnO nanocrystals acting as homoepitaxy nucleation sites, is prepared by spray coating. For this purpose, non-vacuum deposition technique is usually adopted, due to its low cost, while enabling preparation of a ZnO seed layer with a high specific surface area [71].

3.2.1 Seed layer prepared by spray coating

The seed layer is deposited onto the FTO substrate by different techniques, such as pulsed laser deposition, sputtering, spray coating, etc. Among various techniques, spray coating is most widely adopted due to its comparatively simple procedure, as there is no need for a costly vacuum system. Moreover, it has an advantage of large-area deposition and uniformity of the film thickness [59]. Spray coating was employed as a non-vacuum route for deposition of a seed layer on large-area FTO substrates and was used to grow ZnO nanostructure arrays. However, use of multi-step, energy-intensive vacuum processes for seed layer deposition undermines the scale-up potential of solution-grown ZnO nanostructure-based devices.

The seed layer solution was prepared by dissolving 0.1 M zinc acetate dihydrate and aluminum chloride hexahydrate (0–5 at. %) in methanol at room temperature. The resulting transparent solution was then sprayed on FTO substrates, maintained at 350^{o}C with the help of a hot plate, using a portable spray gun connected with an air compressor, as shown in Fig 3.2. Spray parameters, such as precursor concentration, flow rate, and substrate temperature, were optimized to ensure uniform deposition of the seed layer. Five different samples were prepared by varying the precursor volume from 0 to 1 ml (0 at. % of Al), and five further samples were prepared by varying the aluminum concentration. The substrate temperature and spray volume of the precursor are the main parameters determining the seed layer morphology and structural, electrical and optical properties. By increasing the spray volume, film thickness, and particle grain size are increased, as discussed in Chapter 4.1 to 4.3.

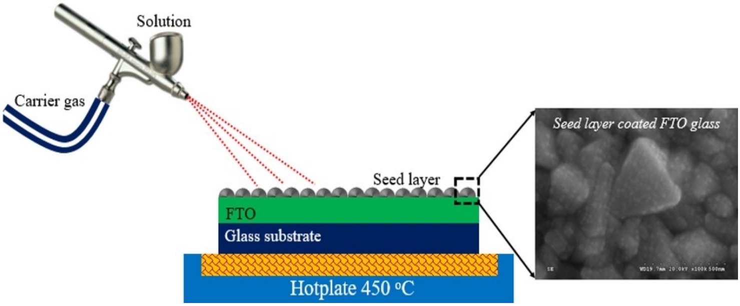

Figure 3.2: Schematic diagram of spray coating set up for deposition of seed layer on FTO substrate.

3.2.2 Growth of aligned ZnO nanostructures arrays

Aligned ZnO nanostructures have been typically grown on single crystalline epitaxial substrates (Al_2O_3 or GaN) by physical vapor deposition (PVD) method [53]. However, the technical feasibility of PVD-grown ZnO nanowires in photovoltaics is largely constrained by insulating and low-transmittance epitaxial substrates. In this regard, Vayssieres developed a low-temperature solution process for the growth of aligned ZnO nanostructures on transparent and conductive glass substrates [55]. However, a hydrothermal method is the most inexpensive process for obtaining uniform and high-quality aligned ZnO nanostructures on substrates.

The hydrothermal method offers many advantages over conventional synthesis methods. Unlike many advanced methods that can be employed to produce a large variety of forms, the respective costs associated with instrumentation, energy and precursors are far lower for hydrothermal methods. From the environmental perspective, hydrothermal methods are more environmentally benign than many other methods. The low growth temperature also mitigates other problems encountered when high-temperature processes (Czochralski method, Bridgeman method) are employed, such as poor stoichiometric control due to volatilization of components and stress-induced defects caused by phase transformations that occur. Moreover, the growth of nanostructures with uniform size and morphology control is presently not possible with many synthesis processes. On the other hand, several morphologies and nanostructure sizes can be obtained via hydrothermal processing [72, 73].

Nanostructure growth under hydrothermal conditions requires a reaction vessel called an autoclave, as shown in Fig 3.3. In the hydrothermal method, a highly corrosive salt is used to synthesize inorganic materials for longer reaction time. The autoclave must be capable of sustaining highly corrosive solvent at high temperature and pressure for a longer period. To avoid corrosion of the autoclave material, it should coated with a non-reactive material (Teflon) from the inside. Due to the larger coefficient of thermal (liner) expansion of Teflon versus metal, Teflon will expand and contract much more with the repeated heating and cooling cycles than its enclosure material.

Aligned ZnO nanostructures with different morphologies were grown on seed layer coated FTO substrate by hydrothermal method. The seed layer precursor solution was prepared by dissolving 0.1 M zinc acetate dihydrate and aluminum chloride hexahydrate (0–5 at.%) in methanol. The resultant solution was sprayed on the FTO substrate maintained at 450^oC. Hydrothermal growth solution obtained by dissolving 0.025 M of zinc nitrate hexahydrate and 0.025 M of hexamethylenetetramine in deionized water was poured into an autoclave. The seed layer coated substrates were loaded into the autoclave and were heated at 95^oC for various durations [74]. After the reaction, substrates were removed from the solution, rinsed with deionized water and annealed at 350^oC for 20 min. To assess the role of the seed layer, ZnO nanostructure was grown on seed layer coated FTO substrates. The aim was to gain a better understanding of the morphology, crystalline structure, electrical property, and growth mechanism, which were characterized by an electron microscope, X-ray diffractometer, and atomic force microscopy, as discussed in Chapter 4.1 to 4.4. These ZnO nanostructure is grown substrates were used as the electron transporting layer in dye and perovskite solar cells. IPCE and PCE were tested for the fabricated device, as discussed in

Chapter 4.1 to 4.3.

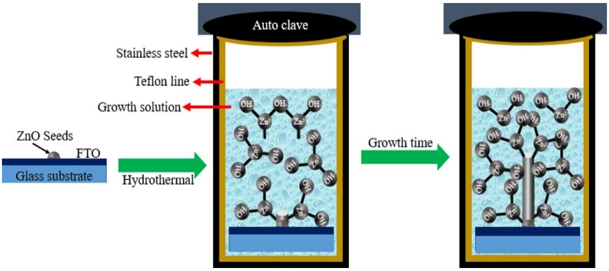

Figure 3.3: Schematic illustration of a typical autoclave used in a hydrothermal method for growth of ZnO nanostructure arrays.

3.3 Electrical properties of ZnO nanowires

Conductive AFM (C-AFM) is a powerful current sensing mode and is derived from contact mode AFM. In C-AFM, a DC bias is applied between a conductive tip and the sample when the tip scans the sample surface, as shown in Fig 3.4. C-AFM can simultaneously measure both height and current distribution [75]. The cantilever deflection feedback signal is used to obtain a contact mode height image. The current passing between the tip and the sample is recorded to characterize conductivity variations in the nanomaterials. It can measure the current in the range of hundreds of femotoamps to nearly a microamp. C-AFM is different from scanning tunneling microscopy (STM), although both apply a DC bias between the conductive tip and the sample. STM is based on the concept of quantum tunneling. When a conductive tip is placed in close proximity to the sample surface, the DC bias allows electrons to tunnel through the vacuum. The resulting tunneling current is an exponential function of tip position, applied voltage, and local sample density. Changes in the tunneling current or the tip height can be mapped above the sample surface by maintaining the height of the tip or the tunneling current, respectively. Therefore, the nanomaterial surface information at an atomic level is obtained by STM. It is also noteworthy that the contact with the sample should be preferentially ohmic. Otherwise, the influence of the additional barrier has to be considered carefully [76]. The commonly used range of the applied voltage is ±10 V. The application of higher voltages is possible using external voltage sources, though additional circuit protection should be implemented.

Particular attention during C-AFM experiments has to be paid to the contact properties, which primarily depend on the tip conditions. Although any conductive AFM probe, including conventional doped silicon probe, can be used in C-AFM, probes with conductive, wear resistive coatings are favored due to the high tip geometry stability and its electrical properties. There are several types of commercially available conductive probes designed especially for CAFM. These are conventional AFM probes for contact mode with one of the following coatings: heavily doped diamond, PtIr, TiN, W_2C, and Au. Despite the fact that the metal coatings like Au or PtIr have lower resistivity (0.01-0.025 Ω.cm), their lifetime is low compared to the diamond coated ones, since the soft coating is worn much faster. Another important parameter is the work function of the coating, which affects the type of the tip-to-sample electrical contact and barrier height in the case of barrier formation [76]. The work functions for several materials used as C-AFM tip coatings are summarized in Table 3.1.

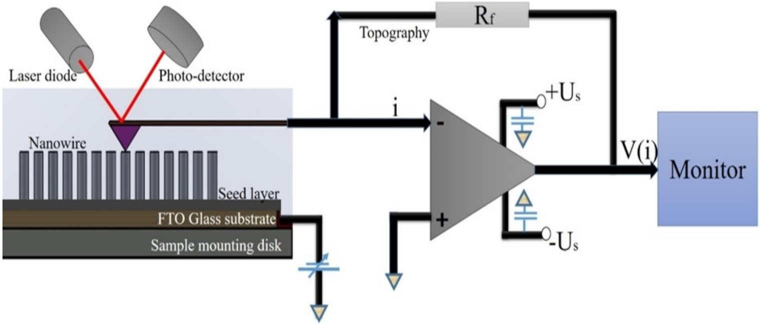

Figure 3.4: Schematic diagram showing the use of an AFM probe used to measure the I–V characteristics corresponding to an individual ZnO nanowire.

Table 3.1: Work functions of materials used as conductive coatings in C-AFM probes

Coating	W_2C	TiN	Au	Pt	PtIr	Diamond
Work function (eV)	4.7-4.8	4.8-5.3	5.10	5.65	5.6	5.7

3.4 Growth mechanism of ZnO nanostructures

A new approach was adopted to prepare the sample for plan-view TEM study. For cross-sectional TEM sample preparation, two samples were attached face to face with glue for mechanical stabilization. Specimen thickness was then reduced from 6 mm to 1 mm equally from both glass substrates without damaging the interface. The thinned specimen was then cut and fixed in a 3 mm copper tube with the help of glue. The copper tube was cut to 3 mm disc using an isomet cutter, and the disc was thinned down to 50 μm using emery paper. The 40 μm disc was then subjected to dimpling to reduce the ion milling time in a cold stage and mitigate the thermal effect of the ion beam during milling, as shown in Fig 3.5. TEM study was conducted at an acceleration voltage of 200 kV for the microstructural analysis [77]. Preparation of the ZnO nanostructure specimens for plan-view TEM studies posed several difficulties. The mechanical properties associated with the morphology of ZnO nanostructures were the limiting factors. Extremely fragile nature of the nanostructures led to their delamination from the substrates.

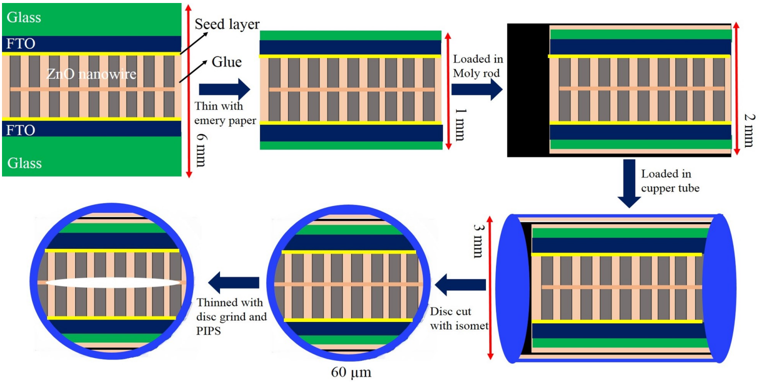

Figure 3.5: Schematic of the cross-sectional TEM sample preparation.

3.5 Solution processed large area DSSCs

The 50 mm × 50 mm size FTO substrates were seeded with an oriented ZnO seed layer using spray coating. Prior to commencing this process, FTO substrates were ultrasonically cleaned in ethanol and acetone for 15 min, respectively. The seed layer precursor solution was prepared using 0.1 M zinc acetate dihydrate in methanol at room temperature. The obtained transparent solution was sprayed onto the cleaned FTO substrate maintained at 350^{o}C with the help of a hotplate, using a portable spray gun connected with an argon cylinder. Finally, the seed layer deposited FTO substrates were annealed at 350^{o}C for 20 min for 1 h to obtain the oriented ZnO seed layers. The solution for growing ZnO nanowires was prepared by dissolving equimolar ratio of 0.025 M zinc nitrate hexahydrate and hexamethylenetetramine in Di-water. The ZnO seed layer deposited FTO was immersed in the solution, where the ZnO/FTO side was placed face down, and the plastic container was kept at 95^{o}C for 3 h. After the reaction, ZnO nanowires grown on FTO substrates were rinsed with Di-water and were annealed at 350^{o}C for 20 min.

Graphene oxide (GO) was synthesized from graphite powder according to the modified Hummer's method [78]. For this purpose, 1 g of graphite powder was added to 92 mL of H_2SO_4, followed by slowly adding 6 g of $KMnO_4$ under continuous stirring in an ice bath. After 15 min, 0.5 g of $NaNO_4$ was introduced into the mixture. The solution was further stirred at 35^oC for two hours, and then 100 ml of Di-water was added. After being stirred for 15 min, the reaction was terminated by the addition of 400 mL of Di-water and 6 mL of 30% H_2O_2 (10 mL). The product was washed with HCl (1:10) and then with water, before being suspended in Di-water. The brown dispersion was extensively dialyzed to remove residual metal ions and acids. After the unexploited graphite in the resulting mixture had been removed by centrifugation, as-synthesized GO was dispersed into individual sheets in ethanol at a concentration of 1 mg/mL with the help of sonication. The resulting solution was then sprayed on FTO substrates, maintained at 100^oC with the help of a hot plate, using a portable spray gun connected with an air compressor. The GO films were prepared by spray coating on substrates and were reduced by using solar irradiation. This procedure allowed ambient oxygen to be removed from the film [79]. Next, the incident solar radiation was focused on the film surface using a 60 mm diameter convex lens (focal length = 15 cm, focused spot diameter $\approx$ 1 mm) as shown in Fig 3.6(a). The experiments were carried out from June to May (weather: sunshine; time of day: 12:00–14:00 pm) in the city of Hyderabad, India. The average solar radiation intensity was in the range of 280–350 nm. To guide the scanning path of the focal spot in a controlled manner, a two-dimensional movable platform with a movement rate of 0.1 mm/s was adopted for the GO reduction. The focal spot was about 6 mm in diameter, while irradiated time ranged from 0 to 1800 s. As a result, the film colour changed from yellowish to dark, as shown in Fig 3.6(b). Raman, as well as XRD, SEM, and AFM, have been widely used for characterization of carbon materials. The resulting data confirm that graphitic nature can be increased by removing the oxygen-based functionalization groups from GO films, as discussed in Chapter 4.5.

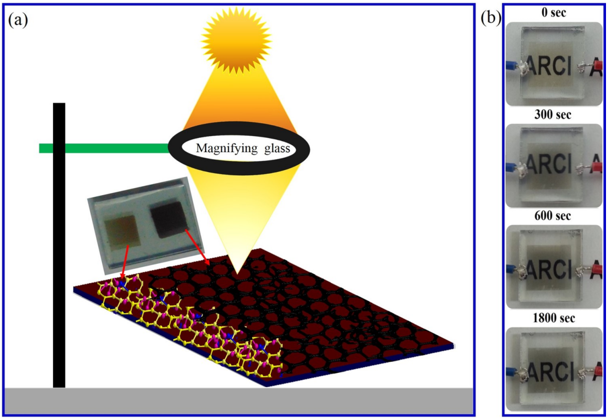

Figure 3.6: (a) Schematic of GO films reduced by solar irradiation, and (b) Photographs of GO films irradiated for three different time periods.

3.6 Solar cell fabrication

3.6.1 Dye-sensitized solar cell

A DSSC is a conventional sandwich configuration that consists of a working and a counter electrode, whereby the space between the electrodes is filled with an electrolyte solution, as shown in Fig 3.7. These electrodes are prepared on a specific glass that has a TCO coating on one side. The transparency of the substrate allows sunlight to enter the cell while its conductive surface collects charges.

Working electrode: Vertically aligned ZnO nanostructure arrays were grown on the seed layer coated FTO substrate by hydrothermal method. The length of the ZnO nanostructure arrays was varied by changing the growth time. Finally, ZnO nanostructure electrodes of different length were annealed in air at 350^{o}C for 20 min.

Dye-sensitization: After confirming that the ZnO nanostructures have optimum length and aerial density, the substrates with ZnO nanostructure arrays grown on them were carefully patterned into 6 mm × 6 mm dimensions. After annealing, ZnO nanostructure based electrodes were allowed to reach 120^{o}C. They were subsequently immersed in 0.3 mM solution of N719 dye in the mixture solvent of acetonitrile and tertbutanol (volume ratio 1:1) and were kept at room temperature for 1 h. Fig 3.7(a-d) shows the dye absorbed on the surface of the ZnO nanostructure arrays.

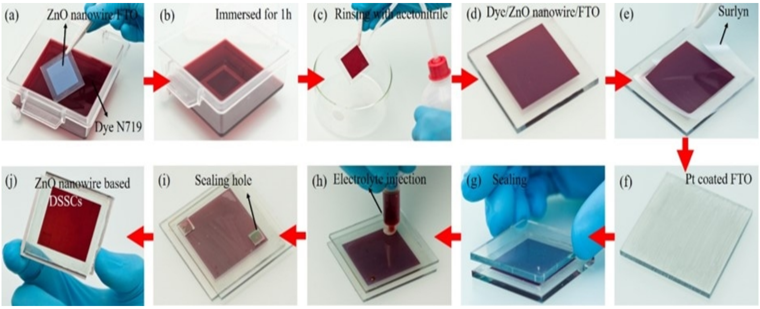

Figure 3.7: Dye-sensitized solar cell fabrication processor.

N719 dye: The sensitizer cis-bis (isothiocyanato) bis (2, 2'-bipyridyl-4, 4'-dicarboxylato) - ruthenium (II) bis-tetra butylammonium, commonly known as an N719 dye, was purchased from Solaronix SA and was used without any further purification.

Dye-desorption from the surface of the ZnO nanostructures: Dye-sensitized ZnO nanostructure was immersed in 3 ml of a basic solution (0.1 M NaOH in 1:1 Di-water and ethanol) for 5 h. After that, the solution color changed to reddish hue as the dye molecules detached from the ZnO nanostructures, as shown in Fig 3.8 [80]. This solution was used for the calculation of dye uptake on the surface of ZnO nanostructures using UV-Vis spectroscopy, as discussed in Chapter 4.1.

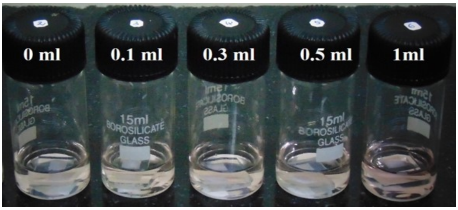

Figure 3.8: N719 Dye detached from the ZnO nanostructure for measuring UV-Vis spectra.

Counter electrode: The Pt paste is a set of chemical precursors for the deposition of catalytic platinum layers, as shown in Fig 3.7(f). In most DSSCs, the counter electrode features a catalytic amount of platinum that greatly enhances electron transfer to the electrolyte. This, in turn, increases the charge density in the solar cell, which directly translates to higher photocurrents and efficiencies. Platisol paste is the perfect companion for iodide-based redox-coupled electrolytes. Pt paste was deposited on the FTO substrate by a surgical blade and was heated at 400^{o}C/10 min [81]. The precursor was reduced to a minimal amount of platinum for optimum material usage while remaining transparent and catalytically active. In both cases, the geometric area of the counter electrode and ZnO working electrode was identical.

Reduced graphene oxide-based counter electrode: Pt counter electrodes give the best performance, but their high cost and the scarcity of Pt restrict large-scale application in DSSCs. These drawbacks have prompted researchers to develop low-cost Pt-free electrodes for DSSCs. Graphene is an attractive replacement for the Pt electrode in DSCs due to their high electronic conductivity, large surface area, corrosion resistance towards iodine, and high reactivity for tri-iodide reduction [82]. Sunlight reduced GO films is used as a counter electrode in DSSCs.

Sealing and electrolyte injection: The sensitized ZnO nanostructure electrode was withdrawn from the dye solution, rinsed with acetonitrile and dried under a nitrogen flow, as shown in Fig. 3.7(c, d). Both working and counter electrodes were assembled in a sandwich configuration, where Surlyn polymer (thickness: 60 μm) sheet was kept as a spacer. The cell was sealed in a hot press maintained at 135^{o}C. To avoid dye degradation, the heat was applied only from the counter electrode side. The space between electrodes in the dye-sensitized solar cell is filled with an electrolyte. A drop of the electrolyte solution was introduced into the cell through an injection hole via vacuum backfilling. Finally, injection hole was sealed by Surlyn and microscope cover glass, as shown in Fig 3.7(g-i).

Electrolyte: Lithium iodide, iodide, 4-tert-butylpyridine, and acetonitrile were purchased from Sigma-Aldrich and were used as received. 1-buyl-3 methlimidazolium iodide and guanidine thiocyanate were obtained from Merck. The redox electrolyte with $[I_3^-]/\ [I^-] = 1{:}9$ was prepared by dissolving 0.5 M LiI and 0.05 M I_2 in an acetonitrile solvent and, if necessary, additives were added.

3.6.2 Perovskite solar cell

For preparing PSCs under ambient atmospheric conditions, $CH_3NH_3PbI_3$ was formed on ZnO nanostructures by a two-step spin coating method.

Preparation of PbI_2 solution: The lead iodide solution was prepared by dissolving 1 M lead iodide in DMF (462 mg/ml) that was kept at 70^oC for 1h [33].

Synthesis of methylammonium iodide (CH_3NH_3I): To a stirred solution of methylamine in methanol (40 wt%, 20 mL) aqueous hydroiodic acid (57 wt%, 21.5 mL) was added dropwise at 0 ^oC over a period of 10 min. The reaction mixture was stirred at the same temperature for two hours. Evaporation of the solvent under reduced pressure took place below 50^oC. The residue was treated with diethyl ether, and the precipitate was collected by the filter, washed with diethyl ether three times. The crude product CH_3NH_3I was recrystallized from a mixed solvent of diethyl ether and ethanol to achieve the desired pure CH_3NH_3I in the form of white crystals. The obtained white crystals were dried overnight in vacuum at 60^oC. The material was kept in a dark and dry environment until further use. The MAI solution was prepared by dissolving the 10 mg in 1 ml of IPA at room temperature [31].

Cell fabrication: The methylammonium lead iodide (CH_3NH_3I) perovskite absorber layer was prepared using a two-step spin coating method. First, lead iodide (100 μL) solution was spin coated at 4,000 r.p.m. for 20 s on ZnO nanostructure and was dried at 100^oC for 10 min. Then, 200 μL of 0.063 M CH_3NH_3I solution in 2-propanol was spin coated on the PbI_2 film. Next, the substrate was heated on a hot plate set at 65^oC for 10 min, after which the substrate became deep dark brown in color [33, 83]. Finally, 100 nm of gold layer was deposited by sputtering on the electrode to form the back contact. The active area of the device was 0.16 cm^2, as shown in Fig 3.9.

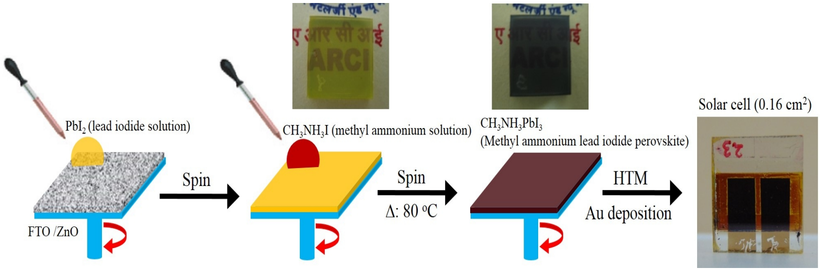

Figure 3.9: Schematic of preparation of the perovskite films by spin coating of the pre-mixed precursor of PbI_2 and CH_3NH_3I.

3.7 Current-voltage measurement

The solar simulator is a light source that approximates the illumination of natural sunlight. Solar simulators with various tailored spectral outputs are used to test a variety of samples including but not limited to solar cells, photo-stabile materials, and other samples under controlled, repeatable, laboratory conditions.

Standard current-voltage measurement of a solar cell determines the voltage-current response of the device, i.e., current-voltage characteristics, in the dark and under different light intensities. In the dark, the applied voltage bias on the device generates a current that flows in the direction opposite to that of the photocurrent. This reverse current is usually called the dark current. For an ideal diode, the dark current Idark relates to voltage in the manner described by Eq(3.3):

$$I_{dark} = I_s(e^{\frac{qv}{kT}} - 1) \tag{3.3}$$

where I_s is the saturation current of the diode (typically 10^{-7}-10^{-9} A), V is the voltage applied to the terminals of the cell and q is the elementary charge.

Under illumination, the current-voltage characteristics follow Eq. (3.4):

$$I_{dark} = I_{ph} - I_s(e^{\frac{qv}{kT}} - 1) = I_{ph} - I_s(e^{\frac{V}{V_T}} - 1) \tag{3.4}$$

where I_{ph} is the photocurrent that depends on irradiation intensity and V_T is often referred to as the thermal voltage that equals $\frac{kT}{q}$. For nonideal devices, an ideality factor, m, is used to describe the weaker dependence of dark current on voltage.

$$I_{dark} = I_{ph} - I_s(e^{\frac{V}{mV_T}} - 1) \tag{3.5}$$

An experimental I-V curve is shown in Fig 3.10, together with the power curve. The following parameter can be derived from the I-V curve.

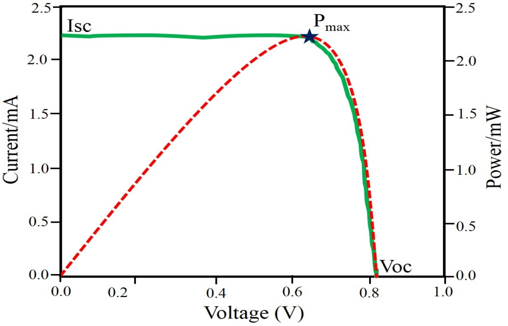

Figure 3.10: Current–voltage and power–voltage solar cell characteristics.

Open-circuit voltage (V$_{oc}$): The V$_{oc}$ is measured without any external load connected, i.e., the circuit is broken or open. In this condition, there is no external current flow between the two terminals of the device, i.e. I = 0 and V = V$_{oc}$. From Eq(3.5),

$$I_{dark} = I_{ph} - I_s(e^{\frac{V_{oc}}{mV_T}} - 1) = 0 \tag{3.6}$$

$$V_{oc} = mV_T ln(\frac{I_{ph}}{I_s} + 1) = mV_T ln(\frac{I_{ph}}{I_s}) \tag{3.7}$$

V$_{oc}$ increases logarithmically with the photocurrent and light intensity.

Short-circuit current (I$_{sc}$): The I$_{sc}$ is measured in conditions characterized by the applied voltage, V = 0. From Eq(3.5),

$$I_{sc} = I_{ph} \tag{3.8}$$

I$_{sc}$ increases linearly with the light intensity.

Fill factor (FF): The power is calculated as I × V and the maximum power point is labelled with the dot. At this point, the device delivers the highest power output with the voltage V$_m$ and current I$_m$.

$$V_m = V_{oc} - mV_T ln(\frac{V_m}{V_T} + 1) \tag{3.9}$$

The fill factor is defined as the ratio

$$FF = (\frac{V_m I_m}{V_{oc} I_{sc}}) \tag{3.10}$$

to describe how the maximum power rectangle fits under the I-V characteristics. Combining Eq(3.9) and (3.10), the approximation for FF can be given by Eq(3.11).

$$FF = \frac{\frac{V_{oc}}{mV_T} - ln(1 + \frac{V_{oc}}{mV_T})}{1 + \frac{V_{oc}}{mV_T}} \tag{3.11}$$

Typical FF of DSSC ranges from 0.6 to 0.8 depending on the individual device and usually increases with the decreasing light intensity. It is also influenced by the series resistance (R_s) arising from the internal resistance and resistive contacts of the cell, as well as parallel resistance (R_{sh}) due to the current leakage. Fig 3.11 illustrates a simplified equivalent circuit for DSSC in which R_s and R_{sh} are present. For an efficient solar cell, a small R_s but a large R_{sh} is required, since a large R_s and a small R_{sh} decrease the FF dramatically.

When R_s and R_{sh} are taken into account, a more precise diode equation is obtained, as given by Eq(3.12).

$$I_{dark} = I_{ph} - I_s(e^{\frac{V+IR_s}{mV_T}} - 1) - FF = (\frac{V + IR_s}{R_{sh}}) \tag{3.12}$$

Efficiency (η): Device efficiency η is a parameter that is associated with the performance of the device. It is defined as the ratio of the maximum power (R_{max}) to the incident sunlight power (P_s).

$$\eta = \frac{(V_m I_m)}{P_s} = \frac{(V_{oc}.I_{sc}.FF)}{P_s} \tag{3.13}$$

P_s is an important experimental parameter and, to compare different results, standard test conditions were always used for all the devices

employed in this work. These conditions include AM 1.5 spectrum illumination with an incident power density of 100 mW.cm^{-2} and a test temperature of 300 K.
When R_s and R_{sh} are taken into account, a more precise diode equation is given by Eq(3.14).

$$I_{dark} = I_{ph} - I_s(e^{(\frac{V+IR_s}{mV_T}} - 1) - FF = (\frac{V + IR_s}{R_{sh}}) \tag{3.14}$$

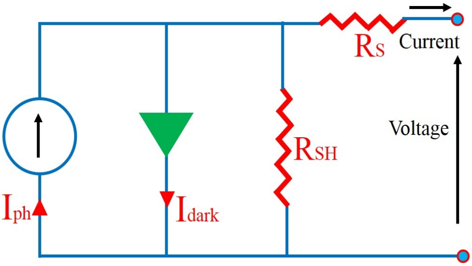

Figure 3.11: The equivalent circuit of a solar cell.

3.8 Incident photon-to-current conversion efficiency

The incident photon-to-current conversion efficiency (IPCE) is specified as the number of light-generated electrons in the external circuit divided by the number of incident photons at a certain wavelength. There are two types of IPCE external quantum efficiency (EQE) and internal quantum efficiency (IQE). The EQE is the ratio between the number of collected carriers and the number of all incident photons on the device active area at a given wavelength. The IQE is the ratio between the number of collected carriers and the number of all absorbed photons by only the active absorber at a given wavelength. The principle of EQE measurement is based on illuminating the sample by a monochromatic light and recording the device electrical current. The difference between IQE and

EQE is important for distinguishing loss mechanisms between absorption properties of the entire device and photo-conversion properties of the absorbing materials.

$$IPCE = (\frac{Nelectron}{Nphoton}) = (\frac{qNelectron/s}{qNphoton/s}) = (\frac{Iph(amp)}{qNphoton/S}) \tag{3.15}$$

$$P_{in}(watt) = P_{in}(\frac{Joule}{S}) = \frac{Nphotons}{S}hv = \frac{Nphotons}{S\lambda}hc \tag{3.16}$$

$$IPCE = (\frac{I_{ph}}{q.P_{in}.\lambda/hc})\frac{I_{ph}.hc}{P_{in}.q\lambda}hv = \frac{I_{ph}}{P_{in}}X\frac{1240}{\lambda(nm)}X100\% \tag{3.17}$$

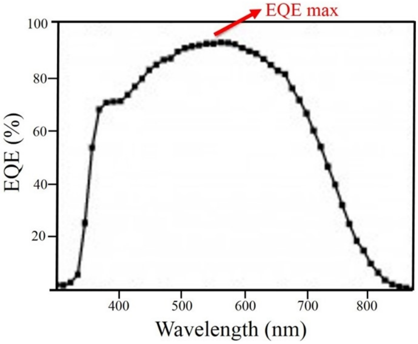

Figure 3.12: EQE and IQE of dye and perovskite solar cells.

The ZnO nanostructure was grown on the seed layer coated FTO substrate using the hydrothermal method. The surface and cross-sectional morphology of ZnO nanostructures were characterized through electron microscopy. The elemental compositions of the samples were determined using energy dispersive X-ray spectroscopy (EDS). The formation of the ZnO phase was confirmed by X-ray diffraction (XRD) and transmission electron microscopy (TEM) analysis. The ZnO nanostructures were employed as a photo-anode in a liquid electrolyte-based DSSC and HTM-free PSC configurations. Current-voltage characterization of DSSCs and PSCs were measured in the dark and under simulated solar light conditions. The output power was calibrated to 1 sun condition (AM 1.5G) using NREL certified silicon reference cell. The quantum efficiency of solar cells was measured in a DC mode using Xe light source, as discussed in Chapter 4.1 to 4.3.

Chapter 4

Results and Discussion

4.1 Spray coated seed layer for aligned ZnO nanowire arrays

Aligned ZnO nanostructures attract considerable interest due to their excellent properties, such as wide band gap, good electrical properties, and morphology tailoring. In particular, aligned ZnO nanowires are the most well-known ZnO nanostructure form and have been used to create a wide range of devices, such as piezoelectric nanogenerators and biosensors, third-generation solar cells, etc [60, 80]. The optimum performance of each device is governed by the morphology of ZnO nanostructures. Presently, 1D ZnO nanostructures are considered to be among the most promising oxide semiconductor materials that can replace TiO_2 as the photoelectrode, thus decreasing the recombination rate and enhancing the DSSCs performance. The aligned 1D ZnO nanostructures may significantly enhance the device performance because of the direct transport pathways for photo-excited electrons [60, 85]. Consequently, synthesis of aligned 1D ZnO nanostructures is the primary task for devices based on 1D ZnO nanostructures. As reported in the extant literature, 1D ZnO nanostructures can be synthesized by various methods, such as vapor–liquid–solid (VLS), electrochemical deposition and hydrothermal method. However, a hydrothermal method is the most inexpensive process to obtain uniform and well aligned 1D ZnO nanostructures on substrates [55]. For the growth of aligned ZnO nanostructures on arbitrary substrates, a seed layer is essential, to reduce the lattice mismatch between nanowire and substrates [86, 87]. Recently, pulsed laser deposition has also been employed for the deposition of ZnO seeds on a sapphire substrate for 1D ZnO nanostructure growth. However, the use of multistep, energy-intensive vacuum processes for ZnO seed layer deposition undermines the scale-up potential of solution-grown ZnO nanostructure-based devices. In this work, spray coating was employed as a non-vacuum route for deposition of a ZnO seed layer on large-area substrates.

In this chapter, the morphology characteristics caused by the seed layer coverage, growth substrate, and growth duration time are studied and are discussed in detail. These parameters can obviously affect the morphology of the ZnO nanostructures, such as orientation, distribution, diameter and length. This investigation may play an important role in the further application of the ZnO nanostructure-based devices.

In the present study, the effect of pristine and ZnO seed layer coated FTO substrate on the ZnO nanostructures grown by the hydrothermal method was investigated. The surface morphology of pristine and ZnO seed layer coated FTO substrate is shown in Fig 4.1(a) and Fig 4.1(b), respectively. The FTO layer was mostly comprised of sub-micron size FTO grains, as shown in Fig 4.1(a). Fig 4.1(b) provides a SEM image of surface of the ZnO seed layer coated FTO substrate. The underlying FTO grains are clearly visible, indicating thin and transparent nature of the spray coated seed layer. Both substrates were subjected to hydrothermal reaction for 3 h at 95^oC. The morphologies of the nanostructures grown on the two substrates are shown in Fig 4.1(c, d). It can be seen that randomly oriented ZnO micro-rods are obtained on pristine FTO substrate shown in Fig 4.1(c), while aligned ZnO nanorods are achieved on the FTO substrate covered with ZnO seed layer, as shown in Fig 4.1(d). The average diameter of the micro-rods of $\sim$500 nm was obtained on the FTO substrate. As can be seen, their distribution is disordered, indicating that pristine FTO substrate is not appropriate for synthesizing aligned ZnO nanowires. On the other hand, the average diameter of the ZnO nanorods is about 200 nm, and they present well-aligned nanowires. Hence, it can be concluded that ZnO seed layer is the necessary condition for obtaining aligned ZnO nanowires.

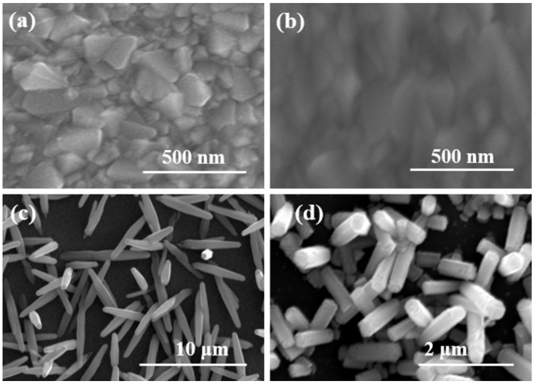

Figure 4.1: Top-view SEM images of (a) pristine and (b) ZnO seed layer-coated FTO substrate. The ZnO nanorods grown on the corresponding substrate are shown in (c) and (d), respectively.

X-ray diffraction (XRD) was used to study the crystalline structure and orientation of the ZnO seed layer as well as the subsequently grown nanowires. Fig 4.2(a, b) shows the XRD pattern of ZnO nanowires before and after growth. Fig 4.2(a) presents the XRD results for ZnO micro-rods grown on the FTO substrate. As can be seen, three peaks arise at $2\Theta = 31.75^o$, 34.44^o, and 36.38^o, which are assigned to the $(10\bar{1}0)$, (0002), and $(10\bar{1}1)$, planes of wurtzite ZnO [88]. It has been demonstrated that the ZnO micro-rods are randomly oriented on pristine FTO substrate due to the large lattice mismatch, and the strained interface region is formed on the FTO surface, which affects the alignment of the ZnO nanorods, as shown in Fig 4.2(c). However, in the present study, the ZnO nanowires were grown on ZnO seed layer coated FTO substrate. The most intensive peak was observed at $2\Theta = 34.43^o$, which corresponds to the (0002) plane. It is accompanied by weak reflection peaks from the ZnO nanowire, corresponding to $(10\bar{1}0)$ and $(10\bar{1}1)$ planes, as shown in Fig 4.2(b). It has been demonstrated that the seed layer reduces the lattice mismatch between the nanowire and a seed substrate and leads to nanowire growth perpendicular to the FTO substrate, as shown in Fig 4.2(d). The ZnO nanowire peak intensity ratio $(0002)/(10\bar{1}1)$ is increased, confirming that nanowires are aligned to the FTO substrate surface [89]. The lattice mismatch (δ) between the ZnO nanowire and the substrate was calculated by using Eq(4.1.0).

$$\delta(\%) = [\frac{(d_{ZnONW(0002)} - d_{FTO(110)})}{d_{FTO(110)}}]100 = -16 \tag{4.1}$$

where d is the interatomic distance and the lattice mismatch between the

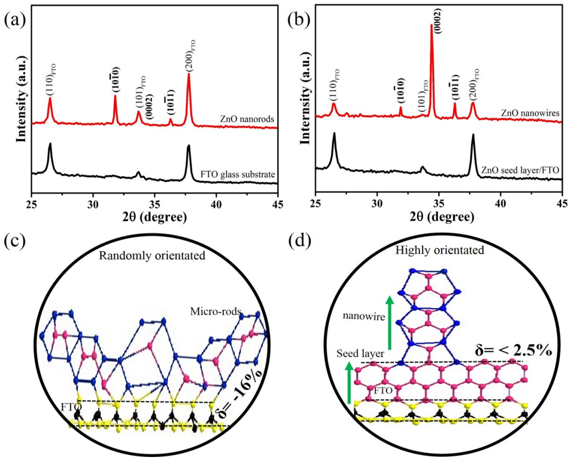

Figure 4.2: (a, b) XRD pattern of ZnO nanowires before and after growth, (c, d) schematic of ZnO nanowire orientation wrt the seed layer.

ZnO nanowire and seed substrate is calculated by Eq(4.1), $4\delta(\%) =< \ 2.5$ [57, 90]. The nanowires are perpendicular to the substrate, as shown in Fig 4.2(c).

$$\delta(\%) = [\frac{(d_{ZnONW(0002)} - d_{ZnOSL(0002)})}{d_{ZnOSL(0002)}}]100 =< \ 2.5 \tag{4.2}$$

The interatomic distance of ZnO nanowires is higher than that of the FTO substrate and the strain is positive.

In the solution-based approach, the ZnO nanostructure alignment and diameter affect the seed layer, as reported by Chen [91]. For the present study, the seed layer thickness and coverage were optimized using the seed layer precursor volume with optimum flow rate (1 ml/min). Increasing the seed layer precursor volume from 0.3 ml to 1 ml resulted in uniform coverage on the substrate and the seed layer thickness increased, as shown in Fig 4.3(a, b and c). These seed substrates were subjected to hydrothermal reaction for 3 h. Aligned ZnO nanowires with ~60 nm diameter and ~2μm length were grown on the surface, as shown in Fig 4.3(d, e, and f). The nanowires are grown on 0.5 ml seed layer precursor coated substrate possess relatively small diameter, better vertical alignment, and higher aerial density, as can be seen in Table 4.1.

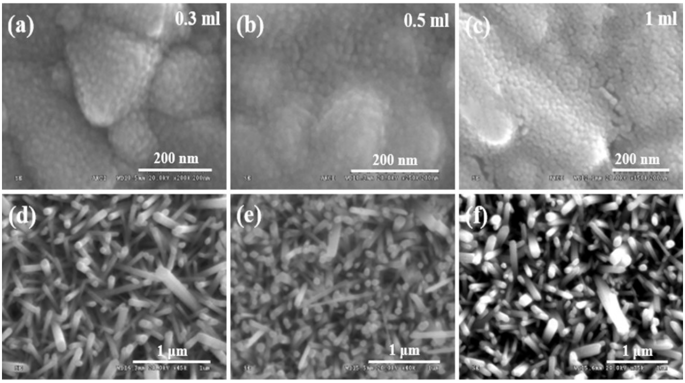

Figure 4.3: Top-view SEM images of FTO substrates spray coated with three different seed layer precursor volumes (a-c) and ZnO nanowires grown on the corresponding substrates (d-f), scale bar = 1 μm.

The seed layer precursor volume affected the seed grain size and the layer thickness. An aerial density of nanowires per unit area increased as the thickness of the ZnO seed layer decreased (Fig 4.4(a) blue line). However, the average diameter of nanowires decreased for thinner and compact ZnO seed layers (Fig 4.4(a) red line). Thus, the results clearly show that the aerial density of the ZnO nanowires increased as the average diameter decreased.

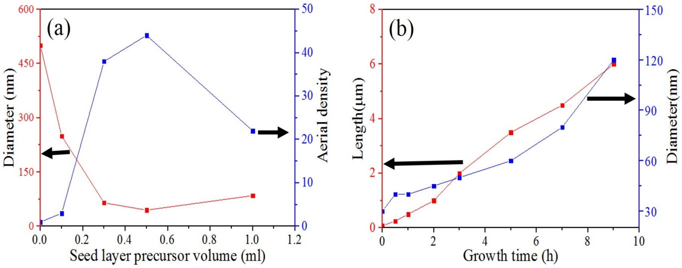

Figure 4.4: (a) Changes in aerial density per 1 μm^2 and an average diameter of ZnO nanowires grown on different ZnO seed layer thicknesses, and (b) changes in length per 1 μm^2 and an average diameter of ZnO nanowires grown using different growth times.

Fig 4.5(a) shows a TEM image of ZnO nanowire synthesized using the hydrothermal method, which reveals that the ZnO nanowire diameter is about 60 nm, as mentioned above (Fig 4.4(a)). Fig 4.5(b) provides an HR-TEM image of the corresponding ZnO nanowire. It can be clearly seen that the ZnO (0001) continuous lattice fringes indicate that they are defect free and exhibit single crystalline nature. The lattice distance measure is about 0.522 nm, indicating ZnO nanowire growth along the ZnO [0001] direction. In addition, the corresponding diffraction pattern (Fig 4.5(c)) confirms that the nanowire has a single-crystalline wurtzite structure growing along the c-axis [51].

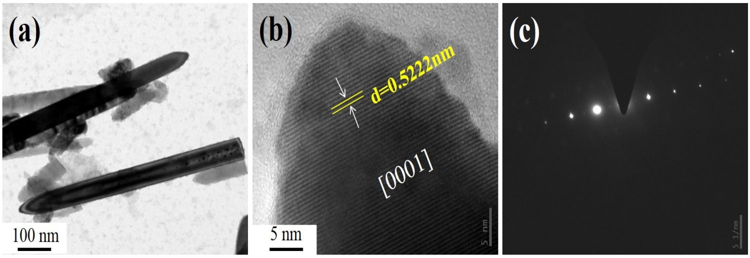

Figure 4.5: (a)TEM image of (a) low magnification (b) HR-TEM and (c) SAED of a ZnO nanowire.

4.1.1 Effect of the growth time

The alignment with a high surface area of ZnO nanowires can be improved by simply increasing the growth time, as reported by Gerrit Boschloo et al. [92]. In Fig 4.6(a-d) the SEM images of the ZnO nanowires grown at various times ranging from 0.5 h to 9 h are shown. It can be seen that the ZnO nanowires are uniformly grown across the entire surface. The cross-sectional SEM image demonstrates that the nanowires grew perpendicular to the substrate, and possess uniform diameter and length distribution (Fig 4.6(e-h)). The diameter and length of nanowires grown for 0.5 h are 35 nm and 150 nm, respectively (Fig 4.6(a, e)). When the growth time was increased to 2 h, the nanowire diameter and length increased to 40 nm and 1μm, respectively, and the nanowires were well aligned (Fig. 4.6(b, d)). However, continuing to increase the growth time to 9 h results in increased nanowire diameter and length, while aerial density decreased, as shown in Fig 4.6(d, h) and Fig 4.4(b).

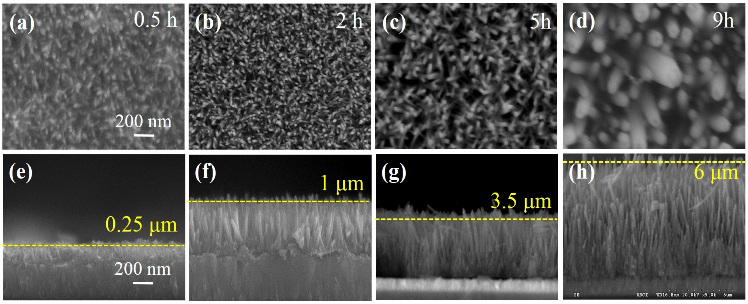

Figure 4.6: SEM images of the surface and cross-sectional morphologies of the ZnO nanowire obtained using different growth times (scale bar = 0.2 μm).

4.1.2 Scale-up process

Well-aligned ZnO nanowire with the high surface was optimized on 0.5 ml coated ZnO seed layer. Further, the ZnO nanowire was scaled up onto a large-area substrate (Fig 4.7(a)). The seed layer was prepared using spray coating by carefully moving the spray gun and adjusting the precursor volume to an optimal level (0.5 ml/2.25 cm^2). Next, a uniform ZnO seed layer was deposited on a 50 mm × 50 mm size FTO substrate. The results indicate that this method is advantageous for large-scale synthesis of ZnO nanowires for optoelectronic applications. The growth of ZnO nanowires on the substrate was carried out in an air-tight plastic container maintained at 95^{o}C for 3 h. A uniform and dense array of ZnO nanowires were formed, as can be seen from the representative top-view SEM image shown in Fig 4.7(b). The cross-sectional SEM image (Fig 4.7(c)) indicates that the ZnO nanowires are vertically aligned and are ~2 μm in length. This confirms that, by using the method employed in this study, ZnO nanowire arrays with uniform morphology could be synthesized on a large scale.

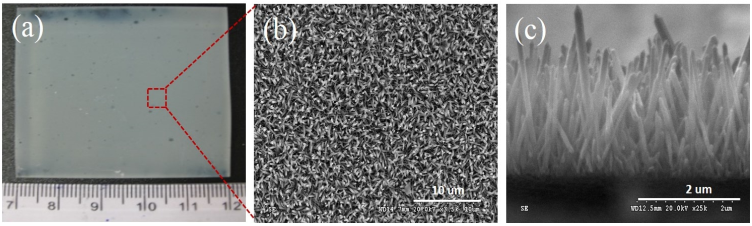

Figure 4.7: (a) Digital photograph of ZnO nanowires grown on a 50 mm × 50 mm size FTO substrate, (b) top view and (c) cross-sectional SEM image of ZnO nanowire arrays.

4.1.3 Photocurrent–voltage characteristics of aligned ZnO nanowire DSSCs

The photovoltaic properties of ZnO nanowire array grown on spray-coated ZnO seed layer/FTO substrates were studied in the liquid electrolyte DSSC configuration. Fig 4.8(a) shows the photocurrent–voltage characteristics of DSSCs measured under 1 sun illumination (100 mW.cm^{-2}, AM 1.5G) conditions. Table 4.1 presents the detailed ZnO nanowire photoanode properties and device parameters for various seed layer precursor volumes. Photoanodes comprising of ZnO rods grown on pristine FTO substrate exhibit a J$_{sc}$ of 1.39 mA cm^{-2}. It is obvious that an increase in the seed layer precursor volume results in a systematic improvement in J_{sc}, as the ZnO nanowires are well aligned and possess high surface area. ZnO nanowire arrays grown on 0.5 ml seed layer precursor coated substrate exhibit a maximum J_{sc} of 1.86 mA.cm^{-2}. In order to provide further insight into the maximum photocurrent observed in ZnO nanowire arrays grown on 0.5 ml precursor coated a substrate, dye loading capabilities of the photoanodes were investigated in detail.

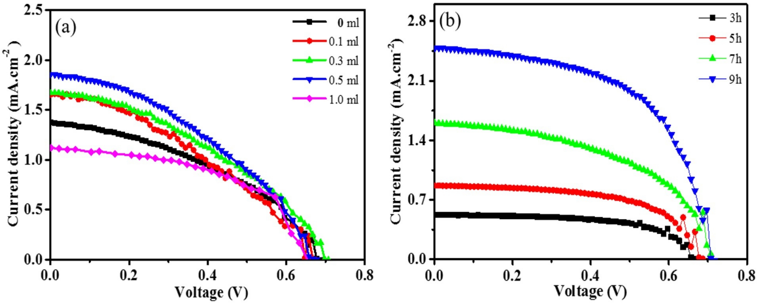

Figure 4.8: Photocurrent density–voltage characteristics of ZnO nanowire DSSCs with (a) various seed layer precursor volumes and (b) over different growth times.

Fig 4.9(a) shows the digital photograph of a sensitized ZnO nanowire dipped in 0.1 M NaOH solution for dye desorbed from ZnO nanowires for calculating the absorbance using UV–vis spectroscopy [93]. Fig 4.9(b) shows the UV–vis absorption spectra of desorbed N719 dye molecules from the ZnO nanowire arrays grown on different volumes of seed layer precursor coated the substrate. The concentration of adsorbed N719 dye was calculated using the Beer–Lambert law:

$$A = \varepsilon.l.c \tag{4.3}$$

where A is the absorption at 520 nm, ε is the molar extinction coefficient of N719 dye, l is the path length and c is the dye concentration.

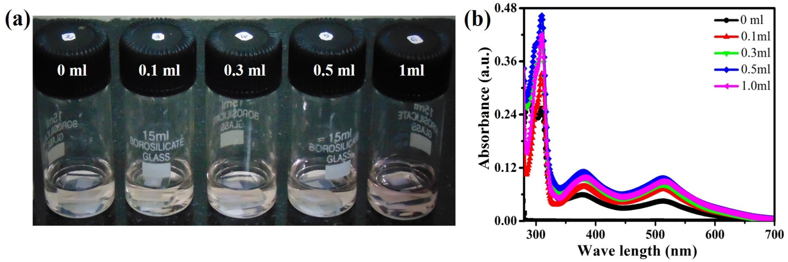

Figure 4.9: (a) Photograph of ZnO nanowire dipped in 1M NaOH solution, and (b) UV–vis spectra of desorbed dye from the ZnO nanowires grown on different volumes of the seed layer precursor coated substrate.

Table 4.1: ZnO nanowire array photoanode properties and detailed device parameters

Seed layer precursor (ml)	Mean diameter (nm)	Aerial density (μm^2)	Adsorbed dye [10^{-9} mol cm^{-2}]	V$_{oc}$	J$_{sc}$	FF	η (%)
0	500	-	2.805	0.68	1.39	0.41	0.39
0.1	250	3	4556	0.67	1.65	0.37	0.41
0.3	65	38	5.222	0.69	1.67	0.38	0.44
0.5	45	44	6.056	0.66	1.86	0.39	0.49
1	85	22	5.611	0.65	1.12	0.66	0.48

Dark current–voltage characteristics of DSSCs measured under forward bias condition can provide further insight into the role of various layers on the photovoltaic performance of DSSCs [94]. Fig 4.10(a) shows the dark current–voltage characteristics of ZnO nanowire array photoanode DSSCs. In the dark and forward bias conditions, electrons enter the cell through a photoanode, react with I_3^- ion and the resultant I^- is oxidized to I_3^- at the counter electrode, as schematically shown in Fig 4.10(b). The process I–III indicates the possible recombination pathways for the electrons with I_3^- ions. Regardless of seed layer precursor volume, all devices exhibit similar dark current onset potential. This result confirms that the charge recombination in I^-/I_3^- redox electrolyte DSSCs occurs predominantly at the porous metal oxide–electrolyte interface. In addition, the magnitude of the dark current density at any given potential continuously decreases with the increase in the seed layer precursor volume. It appears that the passage of electrons from FTO substrate to I_3^- ion in the electrolyte is obstructed by a continuous and dense ZnO seed layer. Under illumination, such thick seed layers can act as a blocking layer and prevent the photoinjected electrons from reaching the current collecting FTO substrate, thus decreasing the J_{sc} [95]. These findings imply that highly efficient ZnO nanowire DSSCs may be achieved by fine-tuning the seed layer morphology and thickness.

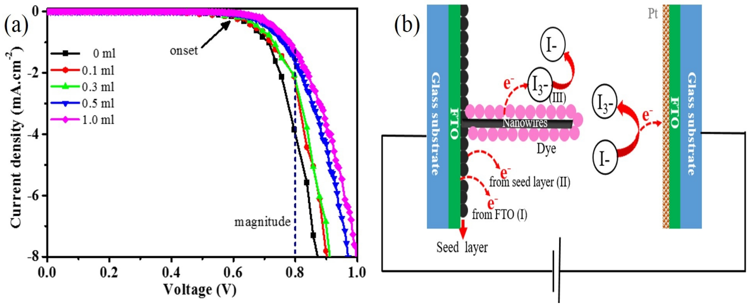

Figure 4.10: (a) Dark I–V characteristics,(b) schematic of electron flow in ZnO nanowires based DSSCs under dark and forward bias conditions.

Table 4.2: ZnO nanowires length wrt growth time and detailed device parameters

Growth time (h)	Length (μm)	V$_{oc}$ (mV)	J$_{sc}$ (mA. cm^{-2})	FF	η(%)
3	2	0.680	0.51	0.61	0.21
5	3.5	0.680	0.86	0.57	0.33
7	4.5	0.700	1.60	0.49	0.54
9	6	0.700	2.49	0.58	1.00

One of the motivations for using longer ZnO nanowires in DSSCs is achieving greater dye absorption, while still maintaining high electron collection efficiency, so that more sunlight could be absorbed to boost DSSC efficiency [92]. Therefore, as a proof of concept, DSSCs were fabricated using 2-6 μm long ZnO nanowires, as shown in Fig 4.8(b) and Table 4.2. As expected, increasing the nanowire length leads to an increase in J$_{sc}$ (2.49 mA.cm^{-2}). This effect is attributed to the high surface area and greater dye loading. The PCE gradually increases as a function of the wire length and reaches 1.003% as the film thickness increases to 6 μm.

A convenient and cost-effective spray coating approach for deposition of a ZnO seed layer on FTO substrate for growing aligned ZnO nanowires using the hydrothermal method was employed. As a result, aligned ZnO nanowires could be grown at a faster rate compared to the common solution-based approaches. These nanowires were used for fabricating DSSCs. It can be shown that the PCE gradually increases as a function of nanowire length and reaches 1.00% under 1 sun illumination for the ZnO nanowire length of 6μm. According to the available evidence, efficiency is low because of the electron recombination between the dye and the electrolyte. The recombination between dye and electrolyte using the conductive seed layer is discussed in Chapter 4.2.

4.2 Electrical property of aligned ZnO non-structure arrays

In previous section, it was noted that lower efficiency was due to the electron recombination at the nanowire/dye interface. For further enhancing the efficiency of DSSCs, a seed layer is usually required to improve the aerial density and achieve optimal alignment. The seed layer is electrically conductive for faster electron transport from the nanowire to the substrate and reduces electron recombination at the nanowire/dye interface. Presently, Al-doped ZnO (Al-ZnO) seed layer is considered to be among the most promising seed layers to replace the ZnO seed layer for growth of aligned ZnO nanowire arrays. It is also posited to decrease the recombination rate and enhanced the DSSCs performance was reported by Nayeri et al. [96]. The ultimate goal of the work presented in this chapter was to improve the electrical properties without changing the seed layer thickness. The conductive seed layer was prepared by adding the 1 at.% of Al to the ZnO seed solution. The seed layers were deposited by spray coating, using the optimum parameters, such as flow rate, precursor volume, and substrate temperature. Fig 4.11 shows the SEM image of two different seed layer coated FTO substrates. It is clearer from the surface and cross-sectional SEM images that the FTO surface is uniformly covered with ZnO seeds (Fig 4.11(a)), and a layer thickness of around 70 nm was achieved (Fig 4.11(c)). The grain size of seeds was calculated through the particle size analysis to range from 15 to 30 nm. This layer was used as a control seed layer for growth of ZnO nanowires. In Fig 4.11(b, d), SEM images show Al-ZnO seed layer coated FTO substrate used as a reference seed layer for ZnO nanowire growth. The deposited seed layer was dense, seed grain size ranged from 10 to 25 nm, and the film thickness was 85 nm. These two seed substrates were used for growth of ZnO nanowires by hydrothermal method at 95^oC.

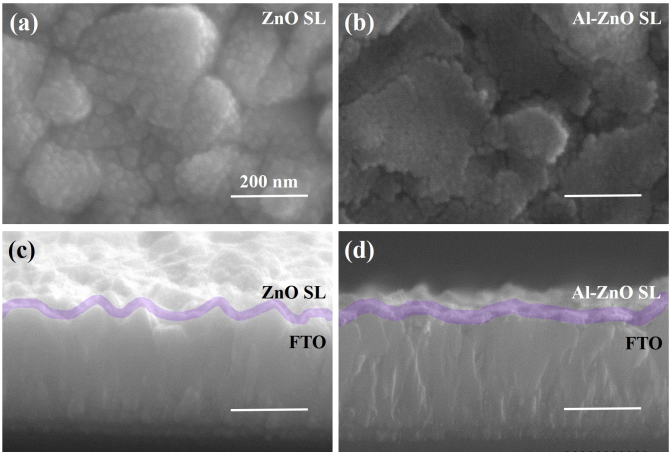

Figure 4.11: SEM images of (a) ZnO, (b) Al-ZnO seed layer coated on FTO substrate, and (c, d) cross-sectional image of the corresponding seed layers (scale bars in all figures represent 200 nm).

The surface and cross-sectional SEM images of as-grown nanowires on ZnO seed layer are shown in Fig 4.12(a, c). The SEM image clearly indicates that all nanowires are tilted by an average of 16^o with sharp tips on the substrate, due to the seed layer coverage and orientation. Further analysis indicates that the average nanowire length is about 0.5 μm, and the diameters are 80 nm, as shown Fig 4.12(c). The SEM images of nanowires grown on Al-ZnO seed layer are shown in Fig 4.12(b, d). ZnO nanowires grown on Al-ZnO seed layer are well aligned and uniform in diameter (50 nm), which is attributed to uniform seed coverage on the FTO surface. The average length of nanowires is around 0.5 μm (Fig 4.12(a, d)).

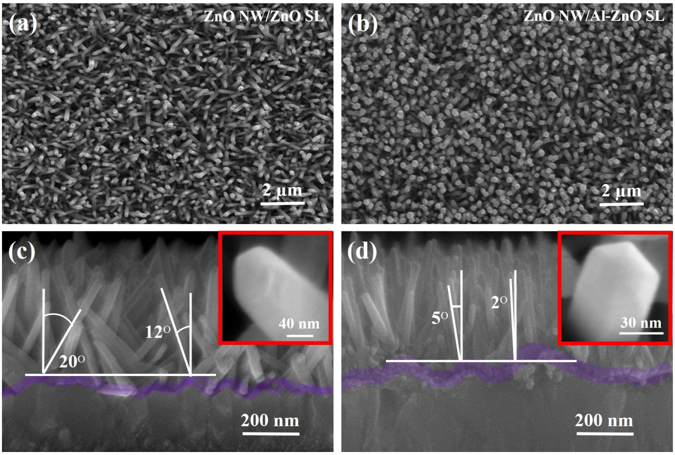

Figure 4.12: SEM image of ZnO nanowires grown on (a) ZnO, (b) AZO seed layer coated FTO substrates, and (c, d) the corresponding nanowires in the cross-section view (inset SEM image shows the nanowire diameter).

The crystalline structure and orientation of ZnO nanowires grown on ZnO and 1% Al-ZnO seed layer was studied by XRD. Fig 4.13(a) shows the XRD pattern of seed layer-coated FTO substrate. A weak intensity peak at 34.46^o arises from the seed layers and the diffraction peaks are indexed to a wurtzite phase of ZnO with a hexagonal structure (JCDS: 36-1451), which is due to thin seed layer and its crystalline size at around 10 nm. The peak intensity is associated with the crystalline size and seed layer thickness [97]. The XRD patterns of nanowires grown on seed layer coated FTO substrates as shown in Fig 4.13(b). In the nanowire XRD pattern, the intensity of seed layer reflection peaks was observed to increase, thus confirming that the nanowires are grown on a seed layer adopt the crystalline orientation of the underlying seed layer [98]. The nanowires grown on Al-ZnO seed layer show a preferentially c-axis orientation, and there is a significant increase in the diffraction peak intensity corresponding to the (0002) plane perpendicular to the FTO substrate. However, the weak diffraction peaks of $(10\bar{1}0)$ and $(10\bar{1}1)$ are also evident, indicating that a few nanowires are tilted relative to the substrate. The relative intensity ratio of $\mathrm{I}_($0002), defined as

$I_{(0002)} = \frac{I_{(0002)}}{I_{(10\bar{1}0)}+I_{(0002)}+I_{(10\bar{1}1)}}$, of nanowires grown on Al-ZnO seed layer is calculated at 0.96. This value is significantly higher than that of nanowires grown on ZnO seed layer ($I_{(0002)} = 0.71$). The (0002) peak intensity ratio also increased, indicating that nanowires are relatively well aligned compared to those grown on ZnO seed layer [74, 89].

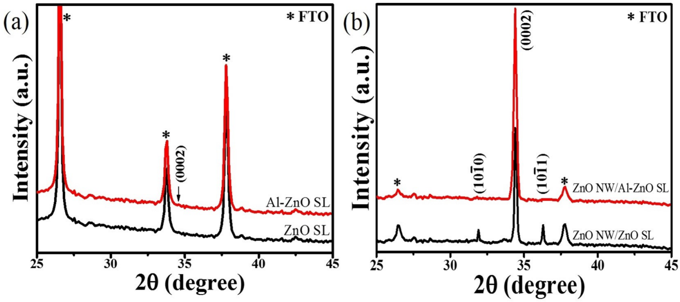

Figure 4.13: XRD pattern of (a) ZnO and Al-ZnO seed layer coated FTO substrates, and (b) ZnO nanowires grown on the corresponding substrates.

The structure of ZnO nanowires was characterized by TEM. Fig 4.14(a) shows a TEM image of a single ZnO nanowire with a diameter of ∼50 nm. The corresponding SAED confirms that the phase of the nanowire is wurtzite structured ZnO (The inset image on the right side of Fig 4.14(a)). Fig 4.14(b) provides an HRTEM image of the obtained nanowire, indicating that the continuous lattice fringes confirm that the nanowire is of single-crystal structure and defect free. The resolved lattice distance of 0.522 nm indicates that nanowires are grown along the ZnO [0001] direction [51, 74].

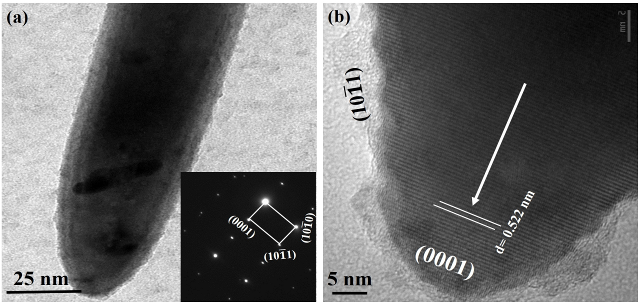

Figure 4.14: (a) TEM image and SAED pattern (inset) of a ZnO nanowire/ZnO seed layer, and (b) HRTEM image of the corresponding nanowire.

Aligned single-crystalline ZnO nanowires have a high aspect ratio, and can provide a direct conduction path for electrons. Better alignment with uniform diameter ZnO nanowires was obtained on Al-ZnO seed layer compared to the ZnO seed layer. Before measuring the nanowire electrical properties, the surface topography of ZnO nanowires was investigated by non-contact AFM. The topography image of the nanowires grown on pristine ZnO seed layer was found to be slightly tilted, less dense and has a larger diameter. On the other hand, nanowires grown on Al-ZnO seed layer are well aligned, dense, and have a uniform diameter and are thus superior to those grown on ZnO seed layer (Fig 4.15(b)). The results yielded by the AFM analysis reveal that by changing the seed layer, the nanowire alignment and uniform distribution on the FTO surface are achieved. Inset image in Fig 4.15(a, b) shows the 3D AFM topography of nanowires grown on Al-ZnO seed layer, revealing greater roughness than when ZnO seed layer is used. Non-contact AFM characteristics confirm that it is possible to measure the electrical properties at the top and the side-facet of a single nanowire.

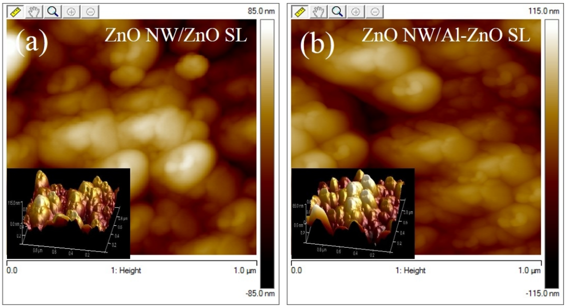

Figure 4.15: AFM topography and roughness (inset) image of ZnO nanowires grown on (a) ZnO, and (b) Al-ZnO seed layer coated FTO substrate.

Conductive-AFM (C-AFM) is employed to investigate the electrical properties of aligned ZnO nanowires. The PtIr probe with a force constant of ∼2 N/m and radius of ∼20 nm allows contact with the top and the side facets of the nanowire, thereby facilitating the evaluation of nanowire electric properties [75]. Fig 3.4 shows the schematic of AFM measurement setup employed for the electrical characterization of ZnO nanowire arrays. For this purpose, metal/semiconductor point contact was achieved by placing a PtIr coated conducting tip on top of a single ZnO nanowire. I–V characteristics was measured by applying an external voltage bias (from +0.6 to -0.6 V) between the PtIr-tip and the nanowire.

The nanowire grown on the substrate was loaded in vertical position on a sample mounting disc, and the C-AFM tip was used to scan across the nanowires. The C-AFM topography images (Fig 4.16(a, d)) and lateral force images (Fig 4.16(b, e)) were recorded simultaneously. In contact mode, the C-AFM tip remains in contact with the nanowire surface at a constant force and the C-AFM tip scans over the nanowires. Moreover, the nanowires are bent consecutively if their density is reasonably low [98]. The line scan tip speed was 7.03 μm/s, and the gain was set at a medium range. At the same points in the corresponding lateral force image (Fig 4.16(a, d)), some scratches are observed. The line scan across the nanowire midpoint in the topography image was used to generate a curve for the scanner retracting distance versus the nanowire lateral displacement, as shown in Fig 4.16(c, f).

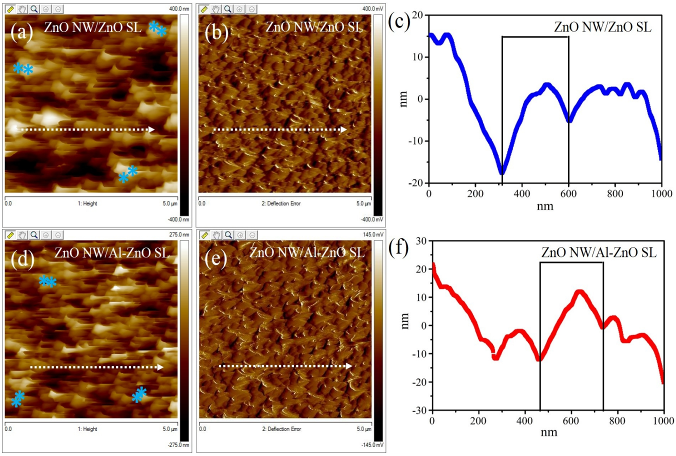

Figure 4.16: (a, d) Topography, (b, e) lateral force image of ZnO nanowires in contacting mode, and line profiles along the dotted lines, (c, f) the curves of scanner retracting distance versus the nanowire lateral displacement.

I–V measurements of nanowires were performed by selecting a proper nanowire from the surface topography image, which was first acquired in the C-AFM mode. The C-AFM tip was positioned at three different locations in each scan area of a single nanowire for measuring the average electrical property of nanowires, as shown in Fig 4.16(a, d) indicated with an asterisk symbol ($*$). The obtained I-V characteristic nanowire curves, as well as the 2D current maps recorded from specific areas, are provided in Fig 4.16(a, d). When the AFM tip is in contact with the nanowire top, asymmetric performance is observed (Fig 4.17(a)) and the current is 3 nA. With the change of the tip position from the top to a side facet, the current increases from 3 nA to 70 nA in the nanowire/ZnO seed layer. Side-facets of nanowire $(10\bar{1}0)$, $(1\bar{1}00)$, $(11\bar{2}0)$ exhibit affinity to H-atoms due to its high conductivity as compared to the top surface of the nanowire [75]. The nonlinear I-V characteristics of nanowires are due to the formation of Schottky barrier at the AFM tip-nanowire/ZnO seed layer interface. Seed layer plays a crucial role in the electron transport from the nanowire to the FTO [76, 99], as shown in Fig 4.17(c). As the work function of PtIr is 5.6 eV, which is substantially greater than the electron affinity of ZnO is 4.2 eV, the electron energy barrier is formed at the AFM tip and nanowire/ZnO seed layer interface, due to high leakage current. However, for nanowires grown on Al-ZnO seed layer, AFM tip interface shows a near-ohmic characteristic, as observed in Fig 4.17(d, e). A similar trend was noted when the AFM tip position changed from the top to the side facet, as the current increased from 3 nA to 200 nA. The energy barrier height decreased at the AFM tip and nanowire/Al-ZnO seed layer interface as Al-ZnO has higher electron affinity (4.8 eV) compared to ZnO (Fig 4.17(f)) [76, 100].

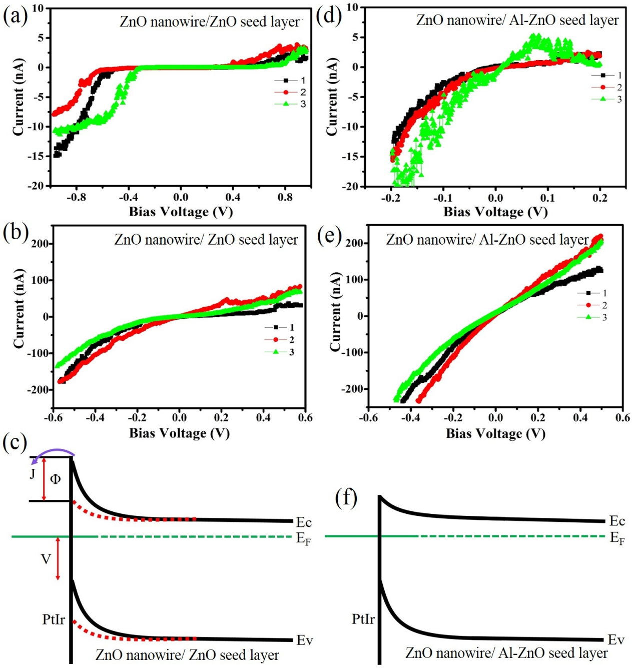

Figure 4.17: I-V curves obtained from a ZnO nanowire at (a) top, (b) side-facet of nanowire/ZnO seed layer, and I-V curves obtained from a ZnO nanowire at (d) top, and side-facet of nanowire/Al-ZnO seed layer; (c, f) energy barrier at the AFM tip and nanowire/seed layer interface under an applied voltage.

The ZnO nanowire alignment, crystalline structure, and electrical properties were characterized using electron microscopy and C-AFM. Well-aligned ZnO nanowires with conductive seed layer improve the electron transport and reduce the recombination at the nanowire/dye interfaces in DSSCs. For the proof of concept, DSSCs were fabricated using aligned ZnO nanowires, whereby the I-V characteristics of a ZnO nanowire grown on seed layer is shown in Fig 4.18(a). DSSCs with ZnO seed layer served as control cell and DSSCs with Al-ZnO seed layer were used as a reference device. Under illumination, DSSCs with Al-ZnO seed layer produce the higher PCE of 0.72% compared to the control cell with ZnO seed layer (Table 4.3), due to the well-aligned structure and higher surface area, as well as faster electron transport from the nanowire to the FTO. The FF of DSSCs with Al-ZnO was higher than that with the ZnO seed layer, which implies lower recombination between the nanowire/dye and the electrolyte.

The dark current characteristics of DSSCs with Al-ZnO and ZnO seed layer are shown in Fig 4.18(b). Dark current density supplies qualitative information on the photoelectrode surface dye loading. Under dark condition, the DSSCs with ZnO seed layer produces higher dark current density, due to the slow electron transport from the nanowire to the FTO and higher recombination is observed at ZnO nanowire/dye interfaces. Lower dark current density in DSSC with Al-ZnO seed layer is caused by efficient dye coverage on the surface of ZnO nanowire, as well as proper electrolyte penetration [94]. These factors result in low recombination at ZnO nanowire/dye interfaces (Fig 4.18(c)). Additionally, the increased V_{oc} can be explained in two ways. First, higher dye loading fosters more charge injection from the dye-sensitizer to the ZnO conduction band and faster electron transport from the nanowire to the FTO. Second, sufficient electrolyte pore filling in DSSCs with Al-ZnO seed layer leads to efficient hole scavenging at ZnO/dye interfaces, lowering the locus of recombination.

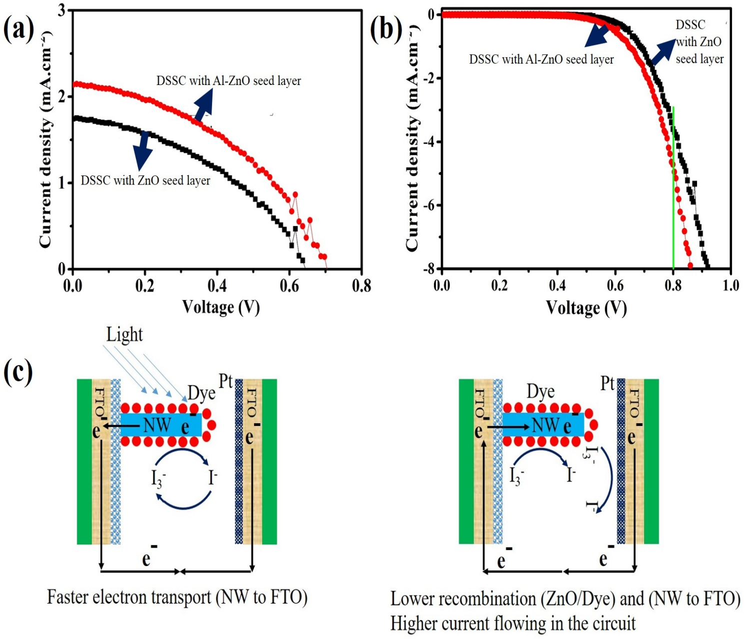

Figure 4.18: I-V characteristics of DSSCs with ZnO, Al-ZnO seed layer under (a) 1 sun,(b) dark; (c) Schematic representation of electron transfer function in DSSCs with Al-ZnO seed layer in dark and 1 sun.

Table 4.3: ZnO nanowire/seed layer-based DSSC properties and detailed device parameters

Device	V_{oc} (V)	J_{sc}(mA. cm^{-2})	FF	η(%)
ZnO NW/ZnO SL	0.64	1.74	0.46	0.51
ZnO NW/Al-ZnO SL	0.70	2.16	0.48	0.72

The influence of seed layers on the alignment, orientation, electrical property and their significant effects on the performance of DSSCs were studied by electron microscopy and C-AFM. The ZnO nanowires are grown on Al-ZnO seed layer yield a higher average current of 200 nA at 0.6 V as compared to wires grown on ZnO seed layer. The DSSCs were fabricated with ZnO and A-ZnO seed layer. The overall PCE of the DSSC with A-ZnO seed layer is higher than that of the control cell. Still, lower efficiency was reported in extant studies, due to the lower surface area and presence of light absorber (dye). In this work, the high surface area of ZnO nanostructures and dye was replaced by perovskite. Perovskite has higher absorption coefficient than the conventional ruthenium-based molecular dye (Chapter 4.3). Thus, most incoming light can be absorbed by the perovskite within a thin layer of about 2 μm, making it suitable as a sensitizer for increasing efficiency of solar cells.

4.3 Seed layer assisted growth of aligned 3D ZnO nanowall arrays

The superior performance observed in devices fabricated using 1D ZnO nanowires is usually attributed to enhanced electron transport and quantum confinement effect. 1D ZnO nanowire-based DSSCs have a lower efficiency that may be attributed to the lower surface area available for dye loading, and lower electron transport from the nanowire to the FTO. The results reported in the previous chapter indicate that 3D nanowall arrays could be an ideal morphology to overcome the aforementioned issues. Expanding from the 1D nanowires, aligned 3D nanowalls are novel building blocks for devices that require not only adequate carrier transport path but also the higher surface area. Nevertheless, aligned 3D nanowalls have received less research attention thus far, presumably because of the difficulties in retaining their shape during the growth process. The present study demonstrates a feasible and scalable low-temperature solution approach for growing aligned 3D ZnO nanowalls on FTO substrates by introducing a controlled amount of Al into the seed layer. Such aligned 3D ZnO nanowall architecture grown on a transparent conductive substrate was demonstrated to be beneficial for electron transport in dye and perovskite solar cells (PSCs). However, in the present study, dye and liquid electrolyte were replaced by perovskite.

4.3.1 The Growth of 3D ZnO nanowalls

Direct synthesis of aligned ZnO nanowalls on electrically conducting and insulating substrates by a vapor-solid-liquid method using Au catalyst was first reported by Meyyappan et al. [101]. The vapor-phase deposition provides aligned ZnO nanowalls. However, the main drawbacks of this method are the need for high temperature (greater than 900^{o}C), as well as insulating and/or low-transmittance epitaxial substrates and a metal catalyst, limiting their technical viability in optoelectronic applications. Hence, attempts were made to grow ZnO nanowalls at lower temperatures ($\sim 100^{o}$C) by solution process. Kim et al. reported growing ZnO nanowalls on Al electrode by aqueous solution route and successfully fabricated piezoelectric nanogenerator [102]. It has been postulated that Al is important for obtaining ZnO nanowalls in the low-temperature solution process. The hydroxyl-ions present in the growth solution react with Al to form $Al(OH)_4{}^-$ which in turn binds to the positively charged Zn^{2+} surface, blocking the ZnO growth along the (0001) direction and promoting lateral growth [103, 104]. By varying the Al film thickness, it is possible to moderate the growth kinetics of ZnO nanowalls. For instance, Koh et al. demonstrated that, by ensuring a steady supply of Al, nanowalls can be obtained, whereas depleted supply of Al leads to nanowire growth [105]. Although these approaches demonstrate the growth of ZnO nanowalls at relatively low-temperatures, the presence of Al in either bulk or film form leads to obstructing the incoming solar light and hampering their use in various solar cells. The growth of aligned ZnO nanowalls on TCO substrates is a rather challenging task.

This chapter describes, for the first time, synthesis of ZnO nanowall arrays on arbitrary substrates through a cost-effective hydrothermal method. By adding a controlled amount of Al into the ZnO seed layer, the morphology of ZnO nanostructure is gradually changed from 1D nanowire to 3D nanowall arrays. Such aligned 3D ZnO nanowall architecture, with the unique combination of high surface area and cage-like pores [102], grown on seed layer coated transparent conductive substrate is found to be beneficial for the electron transporting material (ETM) in dye and perovskite solar cells. The large internal voids are suitable for perovskite loading and enhance the efficiency of solar cells.

For the growth of aligned ZnO nanostructure on a non-epitaxial substrate, the seed layer is essential. The seed layer was prepared by spray coating, using the optimum conditions, including flow rate, substrate temperature, and seed layer precursor volume [106]. Fig 4.19(a) shows a surface view SEM image of pristine (0% Al) ZnO seed layer coated FTO substrate. The underlying FTO grains are clearly visible, indicating thin and transparent nature of spray coated seed layer. When these substrates were subjected to hydrothermal reaction for 3 h, aligned ZnO nanowires with a diameter of approx. 60 nm and length of $\sim 2\ \mu m$ were grown on the surface (Fig 4.19(f)). Addition of 1 at.% Al into seed layer solution did not affect the ZnO seed layer surface morphology, as can be seen from Fig 4.19(b). However, when the substrates were subjected to hydrothermal reaction, nanosheets started to grow across the ZnO nanowires, as highlighted in Fig 4.19(g). When the Al content in the seed layer precursor solution was increased to 2 at.%, nanosheets grew preferentially in the lateral direction, met with one another and eventually developed into nanowalls with a cage-like structure [107]. The ZnO nanostructure is grown on 3% Al-ZnO seed layer coated substrate exhibits well-aligned nanowall-like structure with submicron size channels roughly perpendicular to the substrate. It is widely known that Al undergoes chemical reactions under alkaline conditions in the presence of hexamethylenetetramine that results in $Al(OH)_4^-$, which in turn binds to the positively charged Zn^{2+} surface, blocking the ZnO growth along the [0001] direction and promoting lateral growth [108]. Further increasing the Al content (greater than 2%) in the seed layer precursor adversely affects transparency of the solution, due to the increased Al^{3+} ion quantity in the matrix solution (Fig 4.20(a)). This effect may be attributed to the fact that the seed layer with 1 at.% doping presents more voids than the seed layers with 2, 3, and 5% doping, which may lead to a decrease in optical scattering (Fig 4.20(b)) [109]. Increasing the Al content in the seed layer precursor adversely affects the transparency of the substrate (Fig 4.20(b)) and leads to the growth of thicker ZnO nanowalls. Consequently, the aligned nanowall structure collapses, as shown in Fig 4.19(j). With an increased Al content in the seed layer solution, the concentration of $Al(OH)_4^-$ ions also increases, and increase in the adsorption quantity and coverage rate of $Al(OH)_4^-$ ions on(0001) surface planes causes the increase in nanowall thickness in the range of 3040 nm (Fig. 4.21).

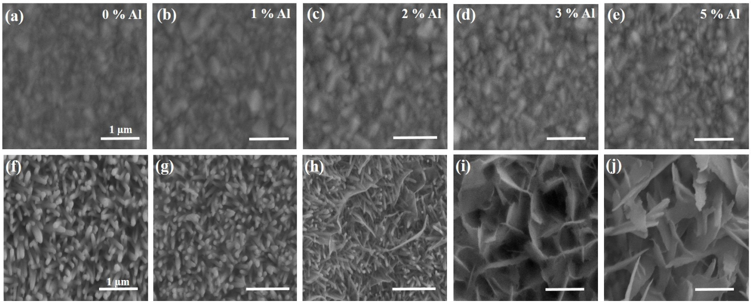

Figure 4.19: Surface-view SEM images of FTO substrates coated with 0-5 at.% of Al added ZnO seed layers (a-e) and ZnO nanostructures grown on corresponding substrates(f-j). Scale bars in all figures represent 1 μm.

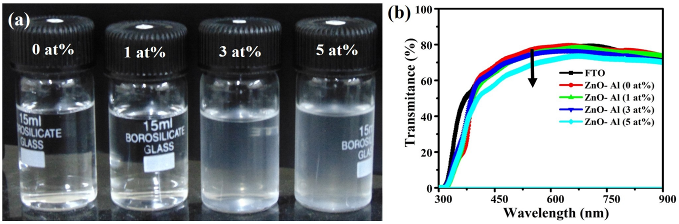

Figure 4.20: (a) Photograph of 0-5% Al-ZnO seed layer precursor solution and (b) UV-visible absorption spectrum of 0-5% Al-ZnO seed layer coated FTO substrate.

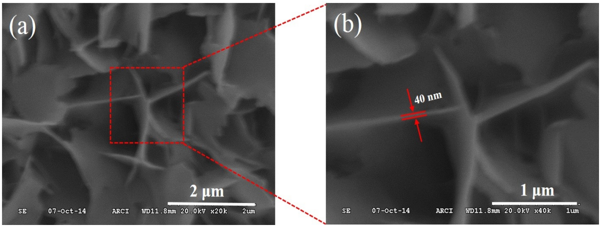

Figure 4.21: High magnification SEM image of aligned ZnO nanowalls grown on 3% Al-ZnO seed layer coated FTO substrate.

The crystallinity and elemental composition of the seed layer and ZnO nanowalls were studied by XRD and EDS, respectively, for confirming whether aluminum is introduced into the ZnO nanowall or not. Fig 4.22(a) presents the XRD pattern obtained from 0% Al-ZnO and 3% Al-ZnO seed layer coated FTO substrates. No additional peaks are observed for ZnO and Al, except those attributed to the FTO substrate. Nevertheless, when the FTO substrate was replaced with Si wafer, spray coated seed layers were found to show a moderate reflection peak at 34.49^o, along with two weak peaks at 31.83^o and 36.31^o. The lack of any Al peak associated with the 3% Al-ZnO seed layer may be attributed to the negligible amount of Al atoms. Fig 4.22(b) compares EDS of 0% Al-ZnO and 3% Al-ZnO seed layer coated FTO substrate. The 0% Al-ZnO seed layer coated FTO substrate shows the presence of Sn, Si, Zn and O elements, whereas the presence of 0.95 at.% Al is observed in 3% Al-ZnO seed layer coated substrate. The XRD patterns of seed layer coated FTO substrates after 3 h hydrothermal reaction are shown in Fig 4.22(c). The magnitude of the seed layer reflection peaks increased, thus confirming that the ZnO nanosheets grew on seeded substrate largely adopt the orientation of the underlying seed layer. All diffraction peaks in the patterns are indexed to a wurtzite phase of ZnO with a hexagonal structure (JCPDS: 36-1451) for both samples [88, 97]. The intense peak observed at $2\Theta = 34.3^o$ for ZnO nanowire indicates the growth along the c-axis normal to the FTO substrate. The weak characteristic peak observed at 34.3^o for ZnO nanowall can be attributed to the presence of nanosheets at an angle to the underneath FTO substrate. The XRD pattern does not provide any evidence of the presence of Al, demonstrating the purity of ZnO nanowalls. It was anticipated that the large formation enthalpy (10^{-5}) required for the incorporation of Al ions into the ZnO crystal may not be possible during low-temperature solution growth [110]. The lack of any readily observable 1.49 KeV Al peak in the EDS plot (Fig 4.22(d)) of ZnO nanowalls further confirms the aforementioned hypothesis.

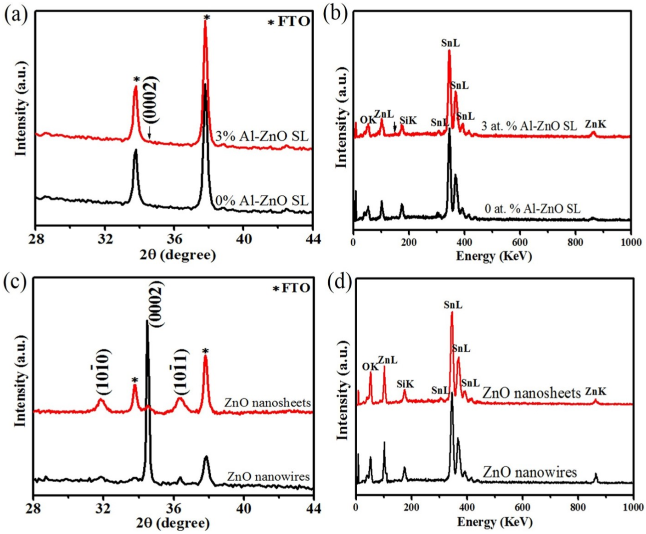

Figure 4.22: (a) XRD pattern,(b) EDS of 0% and 3% Al-ZnO seed layer on FTO substrate; (c) and (d) show XRD and EDS of ZnO nanostructures grown on the corresponding substrates, respectively.

The microstructure of ZnO nanowalls was further investigated using TEM, as shown in Fig 4.23. The low magnification image of ZnO nanowall is shown in Fig 4.23(a). Fig 4.23(b) is an HRTEM image of the corresponding ZnO nanowall. It can be clearly seen that the ZnO (0001) continuous lattice fringes indicate that they are defect free and single-crystalline in nature. The lattice distance measure is about 0.522 nm, and the growth proceeds along the ZnO [0001] direction, as indicated by yellow arrow (Fig 4.23(b)). The inset image shows the corresponding nanowall diffraction pattern. The nanowall has a single-crystalline wurtzite structure growing along the c-axis [102, 107].

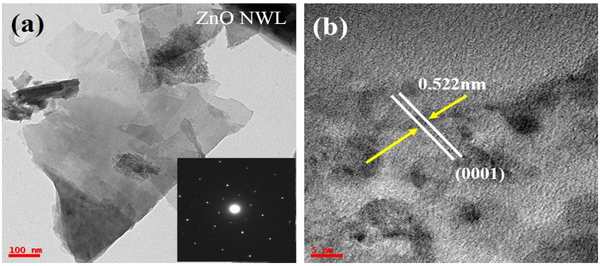

Figure 4.23: (a) TEM image and SAED pattern (inset) of ZnO nanowalls grown on Al-ZnO seed layer coated FTO substrate, and (b) HRTEM of the corresponding nanowire.

4.3.2 Effect of the growth time

The ZnO nanowall aspect ratio and alignment with interconnected nanowalls were studied at different growth times on Al-ZnO seed layer coated substrates. The SEM surface view (Fig 4.24(a-d)) images reveal that, at the initial stage, isolated nanowalls start to grow along the c-axis and evolve into a nanowall structure with increasing reaction time. Nanowalls maintain a linear growth rate as the growth time increases, and nanowalls of about 2 μm thickness were realized after 3 h of reaction [107]. Based on observations yielded by SEM analysis, the most plausible growth mechanism is schematically depicted in Fig 4.25. However, a further increase in growth time to 6 h increases the thickness and length of nanowalls, while alignment of nanowalls collapses, as shown in Fig 4.24(d, h).

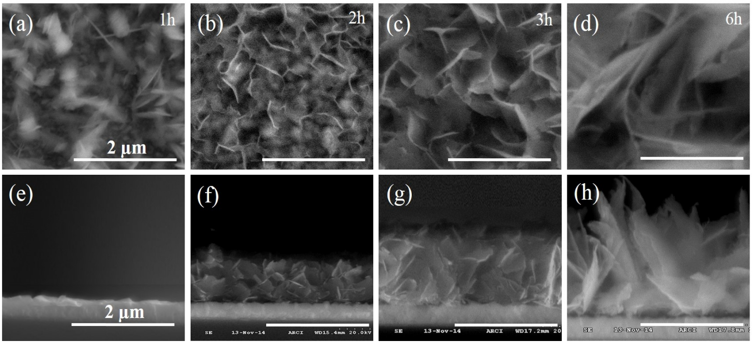

Figure 4.24: SEM image of aligned ZnO nanowalls grown on 3% Al-ZnO seed layer coated FTO substrates for various hydrothermal growth times, (a-e) top view, and (f-j) cross-section view.

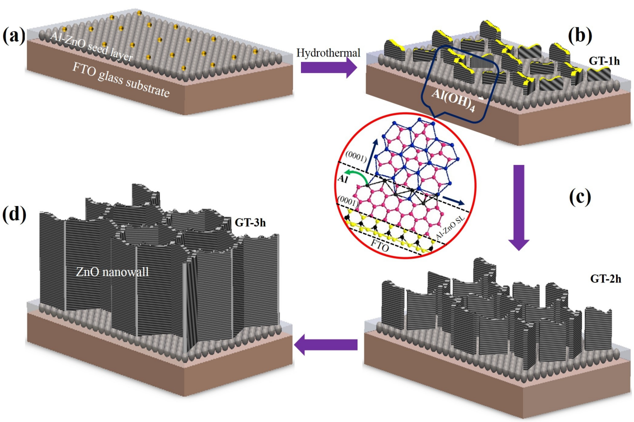

Figure 4.25: Schematic diagrams for ZnO nanowalls grown on Al-ZnO seed layer coated FTO substrate (a-d) using different growth time.

The preceding discussion pertained to the adequate alignment and highly c-axis orientated single-crystalline ZnO nanowalls grown on the FTO surface, studied using electron microscopy and XRD. SEM morphology of ZnO nanowall shows that a large void space is available across the nanowalls, which can be further functionalized with a suitable metal oxide to enhance the surface area. The seed layer assisted the growth of desired ZnO nanostructure, and this approach can be adopted to grow 1D ZnO nanowires on the surface of ZnO nanowalls. As schematically shown in Fig 4.26, by combining ZnO nanowall and nanowire growth processes in series, hybrid ZnO nanowall-nanowire architecture was realized on FTO substrate. Fig 4.27 shows SEM images of 0% Al-ZnO seed layer coated ZnO nanowall array subjected to hydrothermal reaction for various durations. The seeds were evenly coated on ZnO nanowalls without blocking the void space (Fig 4.27(a, e)). Although nanowires start to grow immediately on the nanowall surface, 3 h duration was found to be optimal for yielding a maximum filled ZnO nanowall-nanowire hybrid architecture [103]. The morphology and diameter of a ZnO nanowire grown on the 3D ZnO manual surface were found to be similar to those of nanowires grown on seed layer coated FTO substrate.

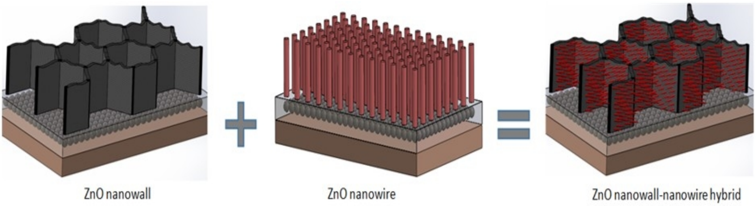

Figure 4.26: Schematic diagram depicting the growth of hybrid ZnO nanostructure.

Fig 4.28 presents the TEM image of ZnO nanowire grown on nanowalls. Fig 4.28(a) represents the ZnO nanowire morphology with a diameter of 20 to 40 nm. In Fig 4.28(b), the HRTEM image reveals the detailed lattice structure of the nanowall. The continuous lattice fringes indicate that they are defect free and are single-crystalline in nature. The lattice distance measure is about 0.522 nm, which is consistent with the distance of (0001) lattice plane of ZnO. The nanowall and wire are of

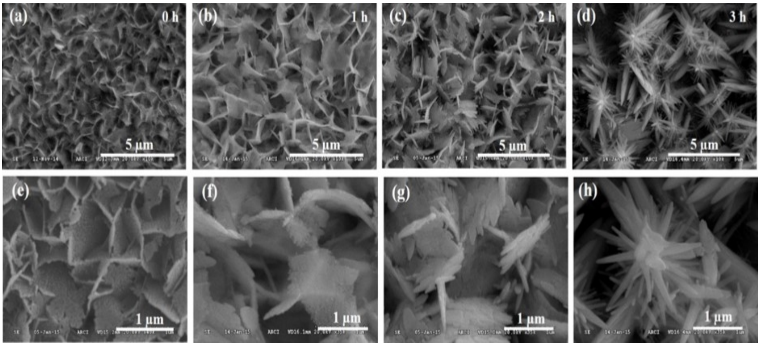

Figure 4.27: SEM image of hybrid ZnO nanostructure grown for various growth times: (a, e) 0 h, (b, f) 1 h, (c, g) 2 h and (d, h) 3 h.

single-crystal structure and are grown along [0001], enclosed by six $10\bar{1}0$ sides facets. The inset image shows the corresponding diffraction pattern confirming that the nanowire has a single-crystalline wurtzite structure growing along the c-axis [54, 74].

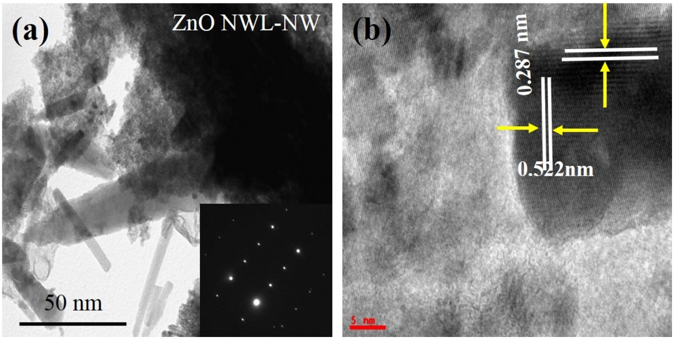

Figure 4.28: (a) TEM image of hybrid ZnO nanostructure, and inset SAED pattern of nanowire, (b) HR-TEM of the corresponding nanowire.

4.3.3 Dye and perovskite solar cells

The aligned ZnO nanostructure and hybrid ZnO architecture grown on FTO substrate is highly suitable for use in third-generation solar cell technology. Fig 4.29 shows surface and cross-sectional SEM images of 1D, 3D, and hybrid ZnO architecture. The high surface area and continuous network of aligned ZnO nanowall array and hybrid nanostructure could be advantageous for absorber loading and electron transport in dye and perovskite solar cells [111, 112]. Yang et al. reported on the performance of the hybrid ZnO nanostructure arrays, highlighting their great potential for practical applications in third-generation solar cells.

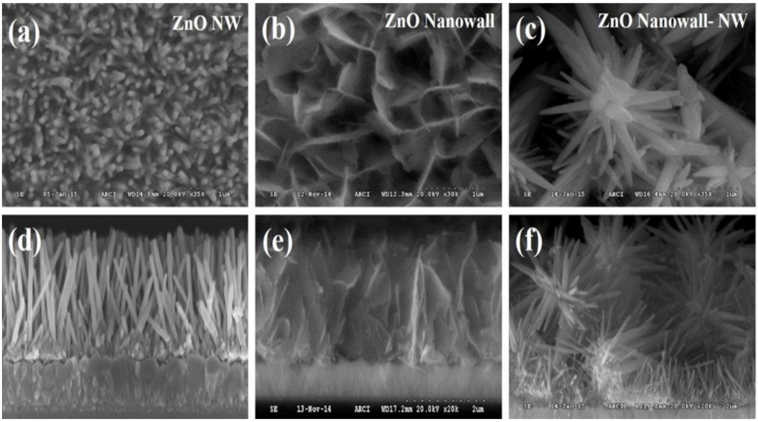

Figure 4.29: (a-c) SEM images of ZnO nanostructures and (d-f) their corresponding cross-sectional images.

The methylammonium lead iodide-based perovskite ($MAPbI_3$) film was deposited on ZnO nanostructures using two-step spin-coating method at the ambient atmospheric conditions (RH $\sim$75 %). Surface and cross-sectional SEM image of $MAPbI_3$ perovskite ZnO nanostructures is shown in Fig 4.30(a-f). The SEM image shows higher infiltration of $MAPbI_3$ perovskite into hybrid ZnO nanostructures.

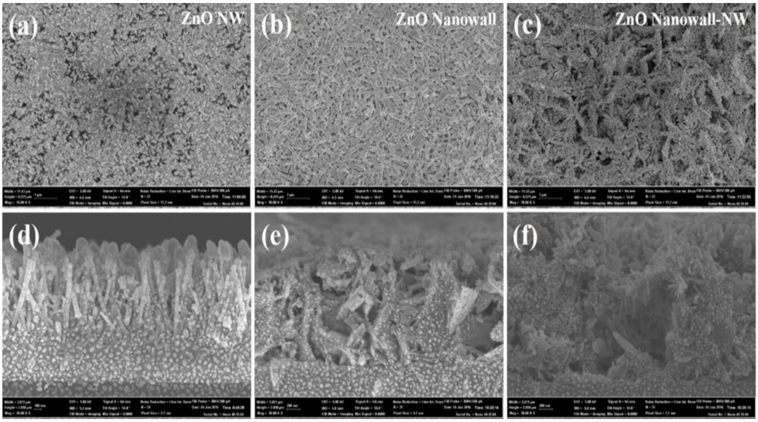

Figure 4.30: SEM images of perovskite deposited (a) ZnO nanowire, (b) nanowall, (c) nanowall-nanowire arrays and (d-f) corresponding cross-sectional images.

To confirm the perovskite formation and infiltration, the pertinent data were studied through the TEM. Higher perovskite infiltration was observed on the ZnO nanowall compared to the nanowire, due to the large void space available across the nanowalls, as shown in Fig 4.31(a, c). Moreover, the ZnO nanostructure surface is fully covered with $MAPbI_3$ perovskite. The HRTEM image in Fig 4.31(b, e) shows lattice fringes with an inter-planar d-spacing of 0.32 nm, which is consistent with the d-spacing of (220) or (004) lattice plane of MAPbI3 perovskite [83]. This finding further supports the notion of high crystallinity in the final $MAPbI_3$ perovskite layer. The corresponding diffraction pattern (Fig 4.31(c, f)) confirms that the perovskite has a tetragonal structure of the $MAPbI_3$ perovskite grains within the layer.

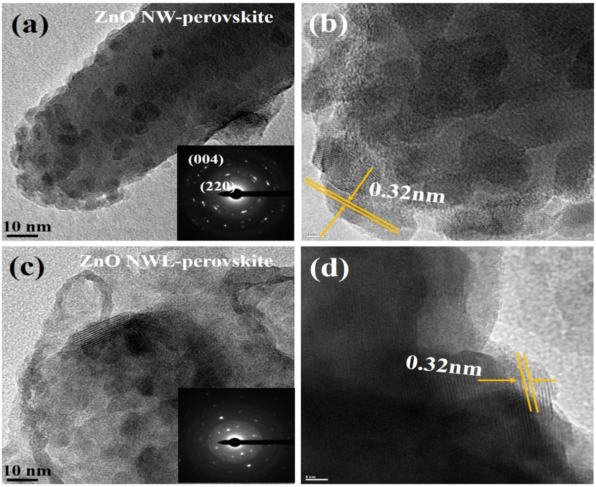

Figure 4.31: (a, c) TEM image and SAED pattern (inset) of $MAPbI_3$ perovskite on ZnO nanostructures and (b, d) HRTEM of the corresponding $MAPbI_3$ perovskite.

The dye and perovskite solar cells were fabricated with ZnO nanowalls grown on 3% Al-ZnO seed layer coated FTO substrate for various hydrothermal growth times. The current-voltage characteristics of corresponding dye and perovskite solar cells measured under 1 sun condition (100 $mW.cm^{-2}$, Air Mass 1.5G) are shown in Fig 4.32(a, b). Nevertheless, PSCs fabricated using ZnO nanowall arrays grown for 2 h show an V_{oc} of 704 mV and a J_{sc} of 6.560 $mA.cm^{-2}$, yielding a PCE of 1.98%. The J_{sc} was further increased to 7.460 $mA.cm^{-2}$ for PSCs fabricated with ZnO nanowall arrays grown for 3 h, and a maximum of 2.23% was obtained (Table 4.4). As discussed in the previous section, vertically aligned nanowalls with open channel-like structures might have improved the $CH_3NH_3PbI_3$ absorber loading and thus yield maximum J_{sc} and η. The low J_{sc} observed for partially collapsed ZnO nanowall array grown for 6 h further supports this hypothesis. The adhesion of ZnO nanowall arrays grown for a longer duration (higher than 6 h) was found to be poor and not suitable for the device fabrication.

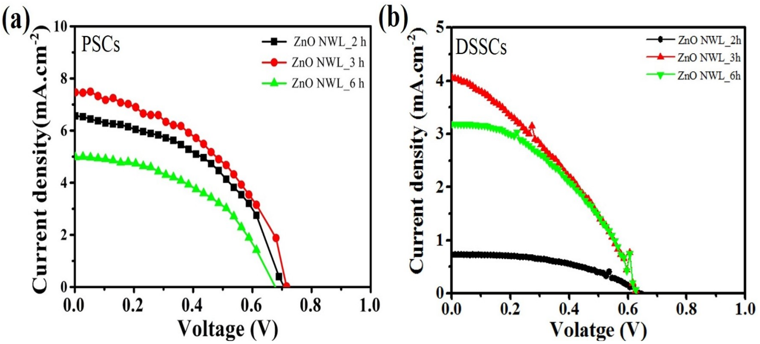

Figure 4.32: I-V characteristics of dye and perovskite solar cells.

It is worth noting that conventional liquid electrolyte DSSCs fabricated with ZnO nanowall photoanode also exhibit similar performance trends. As the growth time increased, ZnO nanowall length also increased. The long nanowalls will provide high surface area for dye loading (Fig 4.33(a)) but the surface recombination rate between dye and nanowall is high, as long nanowalls exhibit low efficiency, as shown in Fig. 4.33(b) and Table 4.5.

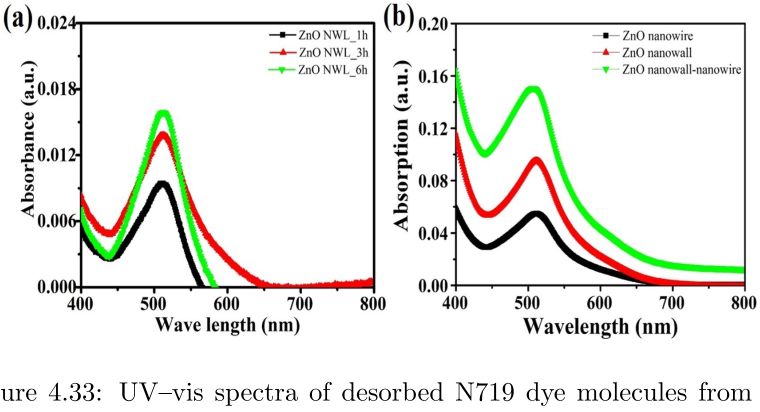

Figure 4.33: UV–vis spectra of desorbed N719 dye molecules from (a) ZnO nanowall with different growth time, and (b) ZnO nanostructures.

Table 4.4: Characteristics of “ZnO nanostructure” PSCs in Figure 4.32(a)

Growth time (h)	V_{oc} (mV)	J_{sc} (mA.cm^{-2})	FF	η(%)
2	0.704	6.560	0.429	1.98
3	0.715	7.460	0.419	2.23
6	0.675	4.950	0.419	1.40

Table 4.5: Characteristics of “ZnO nanostructure” DSSCs in Figure 4.32(b) and 4.33(a)

Growth time (h)	Dye loading [10^{-9} mol. cm^{-2}]	V_{oc} (mV)	J_{sc} (mA.cm^{-2})	FF	η(%)
2	7.333	0.63	0.73	0.44	0.2
3	8.750	0.62	4.07	0.35	0.88
6	10.00	0.63	3.20	0.41	0.82

Although a maximum efficiency of 0.88% for DSSC and 2.42% for PSC was attained in the optimal ZnO nanowall, these values are well below of best-in-class performance. It appears that insufficient surface area of ZnO nanowalls constraints J_{sc} to relatively low value. The large void space available across the ZnO nanowalls can be further functionalized with a suitable metal oxide to enhance the surface area, due to which higher absorber loading and J_{sc} should be expected. The seed layer assisted the growth of desired ZnO nanostructure approach can be adopted to grow ZnO nanowires on the surface of ZnO nanowalls. Fig 4.27 shows SEM images of 0% Al-ZnO seed layer coated ZnO nanowalls subjected to hydrothermal reaction for various durations. The seeds were evenly coated on ZnO nanowalls without blocking the void space (Fig 4.27(a, e)). Although nanowires start to grow immediately on the nanowall surface, 3 h duration was found to be optimal for yielding maximum filled ZnO nanowall-nanowire hybrid architecture. The morphology and diameter of ZnO nanowires grown on the 3D ZnO nanowall surface were found to be similar to those of nanowires grown on seed layer coated FTO substrate.

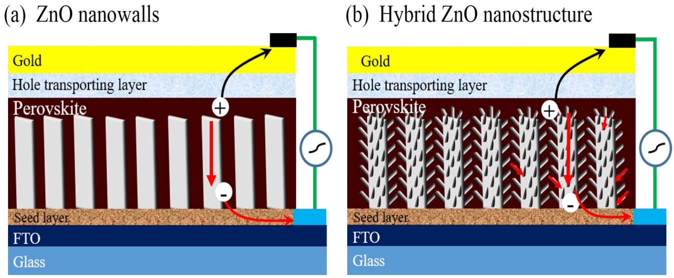

Figure 4.34: Schematic representation of electron transport in (a) ZnO nanowall, and (b) hybrid ZnO nanostructure-based perovskite solar cells.

The photovoltaic properties of DSSCs and PSCs fabricated with ZnO nanowall, ZnO nanowire, and ZnO nanowall-nanowire hybrid photoanode is shown in Fig 4.35(a, c). The PSCs comprising of ZnO nanowall-nanowire hybrid shows a maximum J_{sc} of 9.65 mA.cm^{-2}, which higher than that measured for pristine ZnO nanowall (7.75 mA.cm^{-2}) or nanowire (5.33 mA.cm^{-2}) devices. There is no notable difference in V_{oc} and FF, which due to the defect-free carrier transport path but also the higher surface area, as shown in Fig 4.34. Accordingly, a maximum PCE of 3.28% was achieved in ZnO nanowall-nanowire hybrid PSCs (Table 4.6). To provide further insight into the highest J_{sc} observed in ZnO nanowall-nanowire hybrid PSCs, IPCE spectra of the devices were studied. The IPCE of ZnO nanowall PSC is higher than that of the ZnO nanowire device throughout the spectral range of 400-800 nm, indicating improved absorber loading on 3D ZnO nanowall architecture. The observed IPCE enhancement in the long wavelength region for hybrid architecture may be attributed to the improved light scattering effects (Fig 4.35(b)). Given the HTM-free configuration and all-ambient processing steps, an efficiency value of 3.27% obtained in this case is impressive, and further optimization may lead to higher performance. It is worth noting that conventional liquid electrolyte DSSCs fabricated with hybrid ZnO nanostructure photo-anode also exhibit similar performance trends (Fig 4.35(c, d) and Table 4.7).

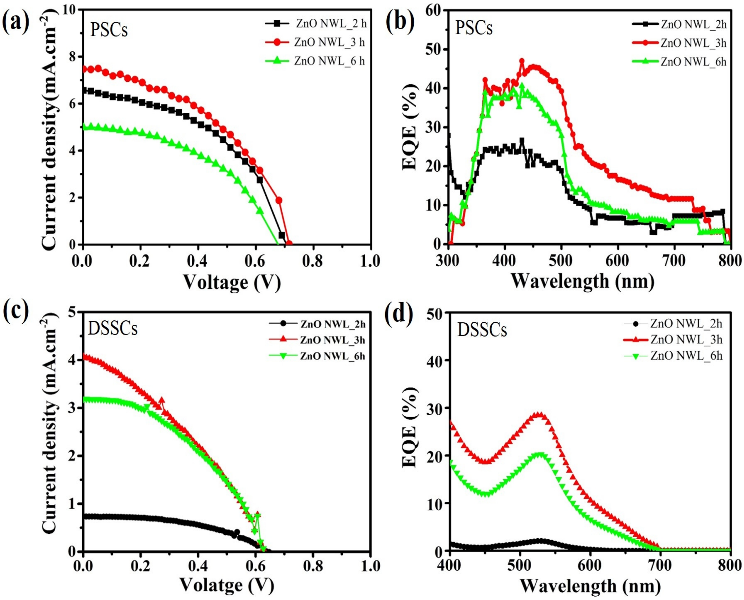

Figure 4.35: (a, c) I-V characteristics, and (b, d) IPCE of ZnO nanostructure-based dye and perovskite solar cells.

Table 4.6: Characteristics of “various ZnO nanostructures” PSCs in Figure 4.35(a)

Nanostructures	V_{oc} (mV)	J_{sc} (mA.cm^{-2})	FF	η(%)
Nanowalls	0.767	7.75	0.43	2.56
Nanowires	0.742	5.33	0.46	1.82
Hybrid	0.791	9.65	0.43	3.28

Table 4.7: Characteristics of “various ZnO nanostructures” DSSCs in Figure 4.35(a) and 4.33(b)

Nanostructures	Dye loading [10^{-9} mol. cm^{-2}]	V_{oc} (mV)	J_{sc} (mA.cm^{-2})	FF	η(%)
Nanowalls	3.652	0.58	4.98	0.56	1.09
Nanowires	6.056	0.62	1.28	0.60	0.47
Hybrid	9.611	0.60	6.20	0.59	1.32

The discussion presented above demonstrated an effective and scalable low-temperature approach for growing aligned 3D ZnO nanowalls on FTO substrate by introducing a controlled amount of Al into the seed layer. Such aligned hybrid 3D ZnO nanowall architecture grown on an FTO substrate was demonstrated to be beneficial for electron transport in dye and perovskite solar cells. The internal voids of aligned 3D ZnO nanowalls were successfully functionalized with ZnO nanowires, thereby improving absorber loading and photocurrent. All-ambient-processed, HTM-free PSCs fabricated using optimum ZnO hybrid nanostructure show maximum J_{sc} of 9.65 mA.cm^{-2} and efficiency of 3.28% under 1 sun condition. Although obtained efficiency values are modest in comparison with best-in-class performance, optimization of absorber coating and processing steps may yield increases across all measures (V_{oc}, J_{sc}, and FF) and therefore an improvement in efficiency.

4.4 Growth mechanism of aligned ZnO nanostructure arrays

The fundamental studies on the growth of aligned ZnO nanostructures and the operation of photovoltaic devices depend directly on the ability to synthesize such materials with predefined structure and functionalities, as discussed in Chapter 4.1-4.3. To accomplish these aims, strict control of the aligned ZnO nanostructure growth process and in-depth understanding of growth mechanisms are required. This chapter introduces the fundamentals of aligned nanostructure growth and the commencement of growth mechanisms. The growth approaches of aligned nanostructures are broadly classified into two categories: (i) catalyst-assisted [113], and (ii) seed layer-assisted growth mechanisms [55]. Recently, nanowire growth was extended to include the growth of nanowalls. The ZnO nanowire growth was further developed and adopted for nanowall growth. The growth mechanism, growth kinetics, and bulk morphological and structural properties are also discussed in the subsequent sections. The electron microscopy and XRD, introduced as a vital tool for nanostructure analysis, are also presented.

4.4.1 Catalyst-assisted ZnO nanostructure growth

The metal catalyst-assisted growth mechanism of aligned nanostructure synthesis, first reported by Wagner and Ellis in 1964 [113], is called vapor-liquid-solid (VLS) process. During the VLS process, the growth mechanism involves the absorption of source material from the gas phase into a liquid droplet of a metal catalyst. The metal catalyst serves as the nucleation site for nanostructure growth. The various processes involved in the VLS growth are schematically described in Fig 4.36. For the growth of ZnO nanowires, gold and Zn are routinely employed as a metal catalyst and precursor material, respectively. The liquid droplet initially acts as an appropriate site for gas phase reactant absorption and, after supersaturation of this liquid alloy, nucleation site forms for crystallization. The catalyst droplet affects the growth direction and controls the nanowire diameter. The growth terminates when no reactant remains in the system or the ambient temperature decreases under the eutectic temperature of the catalyst alloy. A nanowire grown via VLS mechanism has a metal nanoparticle located at its tip [144].

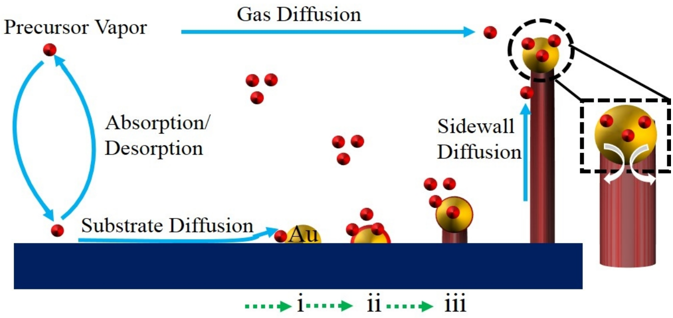

Figure 4.36: Schematic of the vapor-liquid-solid mechanism of the nanowire and step-by-step nanowire growth kinetics.

The nanowall growth was first suggested to be initiated at the narrow boundaries between Au grains that form after the dewetting of an evaporated Au film upon heating. As these boundaries provide a network of high-energy sites for adatom incorporation, the nanowall growth by the VLS mechanism precedes nanowire growth, as shown in Fig 4.37(a, b). However, while the presence of Au is necessary for nanowall growth, evidence suggests that Au does not alloy with Zn. The available XRD and EDS patterns did not show any sign of the presence of Au, demonstrating the purity of ZnO nanowalls [115-117]. Although vapor-phase deposition provides crystalline nanowalls, the need for high temperature (higher than 900^oC), as well as insulating and low-transmittance epitaxial substrates and a metal catalyst, limits their technical viability in optoelectronic applications. Hence, attempts have been made to grow aligned ZnO nanostructures on transparent conducting substrate at lower temperatures ($\sim100^oC$) [55] by seed layer-assisted solution process, and their growth mechanism is discussed in the following section.

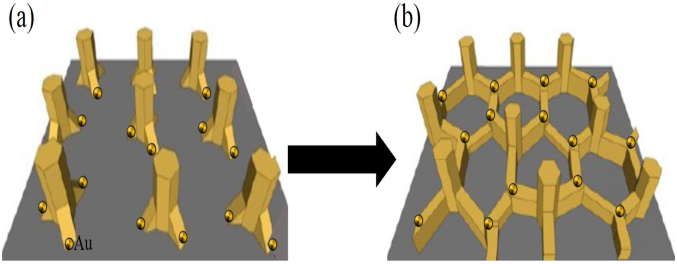

Figure 4.37: Schematic of the vapor-liquid-solid mechanism of a 3D nanowall.

4.4.2 Seed layer-assisted ZnO nanostructure growth

Seed layer-assisted solution-based approach is a highly economical process for obtaining uniform and high-quality aligned ZnO nanowires on a transparent conducting substrate. However, lattice matching between the ZnO nanostructure and the substrate is another important factor in developing an aligned ZnO nanowire on a substrate.

Homogeneous nucleation of the solid phase in liquid does not occur easily, even though the ions are in the supersaturated state. This limitation arises because the homogeneous nucleation requires higher activation energy barrier through rapid cooling and the formation of the solid phase in liquid. Heterogeneous nucleation favors the solution growth due to low contact angle at the liquid–solid interfaces, which reduces the activation energy barrier of growth on the substrate [113]. Although heterogeneous nucleation on a foreign surface is easier than the homogeneous nucleation, controlling random and complex nucleation on the foreign surface is difficult due to lattice mismatch, strain at the interface of growing species and differential surface energy. Therefore, for nanostructure growth, the seed layer should be deposited on the substrate produced with the same material as nanomaterial being grown on it. The advantage of using the same material as a seed layer stems from the resulting effective nucleation on favorable sites with minimal surface free energy, which control morphology and orientation of nanocrystals [118].

ZnO nanowire: In a typical hydrothermal method, growth solution is prepared with equimolar aqueous solutions of the zinc nitrate hexahydrate $(Zn(NO_3)_2).6H_2O$ and the hexamethylenetetramine $((CH_2)_6N_4)$. In the all low-temperature solution based process, Zn^{2+} and OH^- are provided by hydration of $Zn(NO_3)_2.6H_2O$ and HMTA [74, 91]. When the temperature is applied to the growth solution, HMTA hydrolyzes in Di-water and steadily produces formaldehyde (HCHO) and ammonia (NH_3):

$$(CH_2)_6N_4 + H_2O \rightarrow 4NH_{3(g)} + 6HCHO_{(g)} \tag{4.4}$$

The ammonia then decomposes in the solution to form OH^- ions:

$$NH_3 + H_2O \rightarrow NH_4^+ + OH^- \tag{4.5}$$

Ammonia is critical in the synthesis process because, if HMTA hydrolyzed very quickly and produced a large amount of OH^- ions in a short period, a high pH environment would be created in the growth solution. The Zn^{2+} ions in the solution would then react with a large amount of OH^- ions available and precipitate quickly. This would result in a fast consumption of the precursors and affect the oriented growth of ZnO nanowires. Real-time measurements carried out by Ashfold et al. revealed that the pH of the growth solution remains between 5.5 and 5.6 when the temperature is applied [91]. The Zn^{2+} ions form the dissociated zinc nitrate solution and then react with the OH^- ions to form $Zn(OH)_2$ that undergoes a condensation reaction to form a water molecule and crystalline ZnO:

$$Zn^{2+} + 2OH^- \leftrightarrow Zn(OH)_{2(s)} \tag{4.6}$$

$$Zn(OH)_2 \leftrightarrow ZnO_{(s)} + H_2O \tag{4.7}$$

During the growth process, the Zn^{2+} and OH^- concentrations reach the critical supersaturation value, while $Zn(OH)_2$ forms spontaneously in the solution and proceeds to dehydrate into ZnO. Fig 4.38 describes in detail various processes involved in the aqueous growth of aligned ZnO nanowires and depicts their growth direction. In a supersaturated solution, ZnO begins to nucleate on a substrate spray-coated with a ZnO seed layer, which acts as a pre-oriented layer for the nucleation and growth of ZnO nanowires with preferred c-direction alignment [118, 119]. The Zn- and O-terminated (0001) surfaces of ZnO nanostructures are grown along the c-axis direction, yielding high-energy polar surfaces.

Therefore, when a ZnO nucleus is newly formed, owing to the high energy of the polar surfaces, the incoming precursor molecules tend to absorb favorably on the polar surfaces. This leads to fast growth along the [0001] direction, forming ZnO nanowires [119].

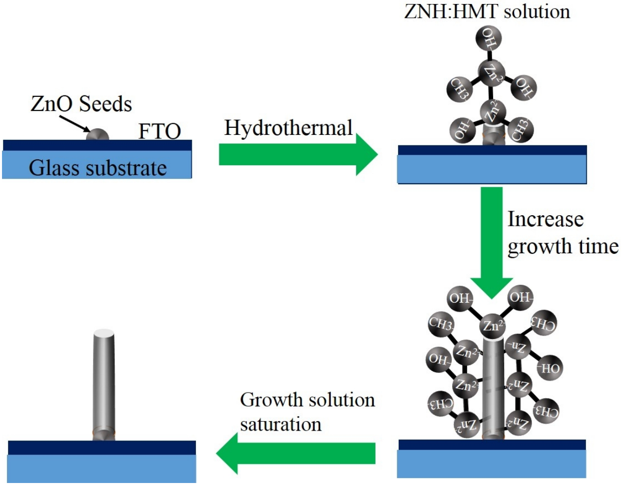

Figure 4.38: Schematic of growth of the ZnO nanowire on seed layer-coated substrate by hydrothermal method.

ZnO nanowall: An efficient and low-temperature solution approach for growing aligned ZnO nanowall on FTO substrate by introducing a controlled amount of Al into a seed layer is described below. The growth mechanism of aligned ZnO nanowalls on Al-ZnO seed layer-coated FTO substrate is also demonstrated. The Zn^{2+} ions exist in the form of $Zn(OH)_2$ complex species serving as growth units for ZnO crystal growth in any direction. The excess OH^- ions are easily adsorbed on the positively charged (0001) surface, and growth along the [0001] direction is partially restricted. Additional hydroxide ions originate from Al source of the seed layer (Eq 4.8). Al undergoes chemical reactions under alkaline conditions in the presence of amine and is supposed to form an aluminum hydroxide [$Al(OH)_4{}^-$] (Eq 4.9). $Zn(OH)_2$forms spontaneously in the solution and proceeds to dehydrate into ZnO (Eq 4.10).

$$Al - ZnOSL + (CH_2)_6N_4 + H_2O \rightarrow 4NH_{3(g)} + 6HCHO_{(g)} + Al(OH)_4^- \tag{4.8}$$

$$Zn^{2+} + 2OH^- + Al(OH)_4^- \leftrightarrow Zn(OH)_{2(s)} \tag{4.9}$$

$$Zn(OH)_2 \leftrightarrow ZnO_{(s)} + H_2O \tag{4.10}$$

It can be presumably bind to the positively charged Zn^{2+}-terminated (0001) polar surface of ZnO more strongly than to other nonpolar surfaces; thus, the ZnO growth along the [0001] direction is effectively blocked [84]. Fig 4.39 describes in detail various stages involved in the growth of 3D ZnO nanowall on a substrate. By increasing the growth time, the nanowalls are extended in the direction of the polar surface, which are connected and form a cage-like 3D morphology.

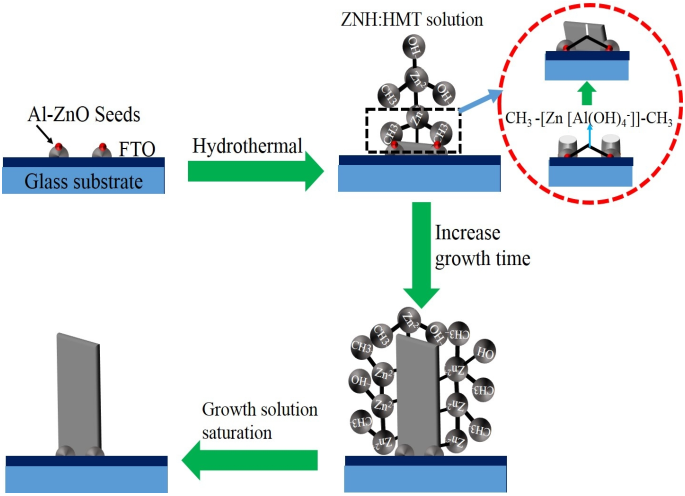

Figure 4.39: Schematic of various stages of the 3D ZnO nanowalls synthesis by hydrothermal method.

The growth mechanism of aligned ZnO nanostructures was characterized using the electron microscopy and XRD. The SEM image confirms that a suitable alignment can be obtained with the optimized synthesis parameters. In addition, XRD spectra and HRTEM reveal a preferred orientation and growth direction of ZnO nanostructures. As-grown ZnO nanostructure crystalline structure and morphology were examined using XRD and electron microscopy. The cross-sectional morphology of the SEM image indicates that the ZnO micro-rods are randomly grown on pristine FTO surface, as shown in Fig 4.40(a). The corresponding rod diffraction pattern is shown in Fig 4.40(b). All diffraction peaks in the patterns are indexed to a wurtzite phase of ZnO with a hexagonal structure (JCDS: 36-1451) [120]. The XRD pattern also reveals that the ZnO micro-rods are randomly orientated on the substrate, due to a significant lattice mismatch (δ = -65 %) between the ZnO rods and the substrate, as shown in Fig 4.40(c). The seed-free growth of aligned ZnO nanowires is very difficult on substrates, due to lattice mismatch [56]. Having a seed layer is crucial for attaining an aligned nanowire on a substrate. After depositing the seed layer on the FTO substrate, the seed layer will reduce the lattice mismatch between the ZnO nanowire/seed substrate and would facilitate the growth of an aligned ZnO nanowire on the substrate, as shown in Fig 4.40(d). The corresponding ZnO nanowires grown on seed layer diffraction patterns are shown in Fig 4.40(e). The diffraction pattern reveals that nanowires are highly c-axis orientated on the substrate, due to the low lattice mismatch (δ = 2.5 %), as shown in Fig 4.40(f). With respect to the nanowall growth, it can be seen that the pyramidal Al-ZnO seeds eventually merge, forming an Al-ZnO layer that forms networks between the nanowires, as shown in Fig 4.39. The ZnO nanostructure was grown on an Al-ZnO seed layer-coated substrate characterized by aligned nanowalls with submicron-sized channels roughly perpendicular to the substrate, as shown in Fig 4.40(g). The $Al(OH)_4{}^-$, which in turn binds to the positively charged Zn^{2+} surface and blocks the ZnO growth along the [0001] direction while promoting lateral growth, is shown in Fig 4.40(i) [108]. The diffraction pattern of ZnO nanowalls is shown in Fig 4.40(h). The XRD patterns of seed layer-coated FTO substrates after hydrothermal reaction of 2 h duration are shown in Fig 4.40(h). The intensity of the seed layer reflection peaks was observed to increase, thus confirming that the nanostructures grown on a seeded substrate adopt the crystalline orientation of the underlying seed layer. All diffraction peaks in the patterns are indexed to the wurtzite phase of ZnO with a hexagonal structure. The weak characteristic peak observed at 34.3^o for the ZnO nanowall can be attributed to the presence of nanosheets positioned at an angle to the underlying FTO substrate. Al plays a vital role in the growth of a ZnO nanowall on a substrate. When as-grown ZnO nanowalls were examined for Al content, XRD pattern did not provide any evidence of the presence of Al, demonstrating the purity of the ZnO nanowalls.

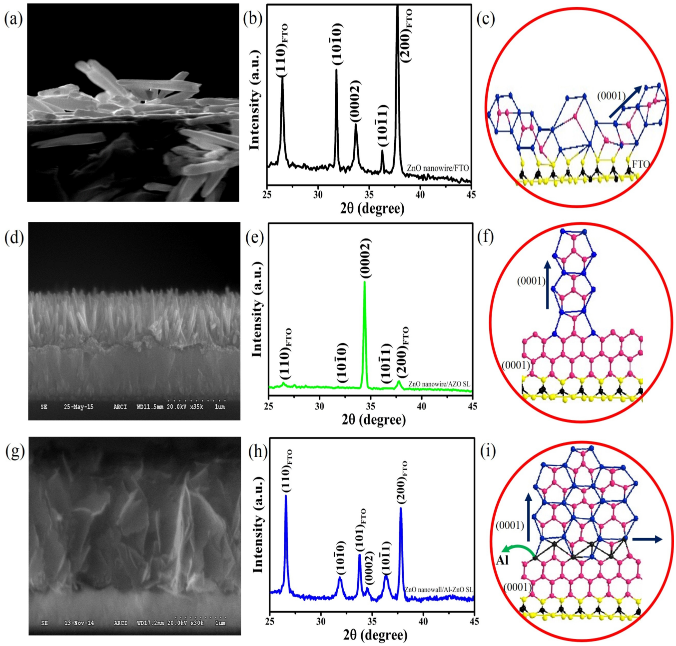

Figure 4.40: Cross-sectional SEM image of (a, d, g) ZnO nanostructure grown on an FTO substrate, (b, e, h) XRD, and (c, f, i) schematic representation of ZnO nanostructure growth.

Fig 4.41(a) shows the low-magnification cross-sectional TEM image of ZnO nanowires grown from a ZnO seed layer. The nanowires with the average diameter of ∼60 nm are grown perpendicular to the substrate. The square regions in Fig 4.41(a) represent the selected area for use in the TEM analysis. The corresponding SAED patterns are shown in Fig 4.41(c) and Fig 4.41(d), respectively. The SAED patterns obtained from the nanowire (SAED1) and the seed layer (SAED2) depicted in Fig 4.41(a) indicate that a single-crystal ZnO nanowire and the seed layer exhibit excellent crystalline quality and are grown without any tilting of the (0001) planes. The HRTEM image clearly shows the lattice spacing of the ZnO nanowire/seed layer with an interplanar spacing of 0.522 nm, as shown in Fig 4.41(b, e) [119]. Moreover, the nanowire and the seed layer growth direction, determined from both the HRTEM image and the SADP, followed the [0001] orientation, the fastest growth direction in the ZnO crystal.

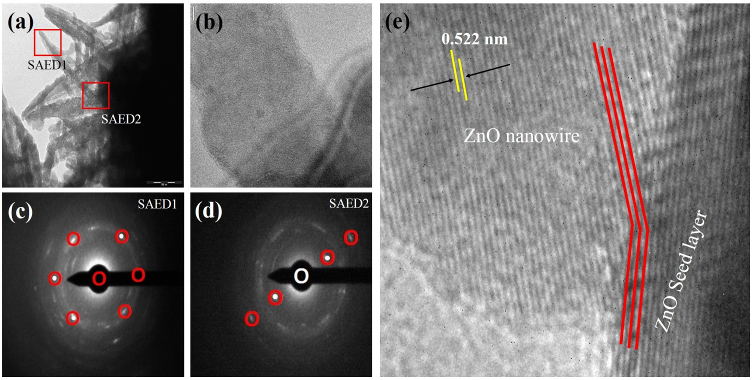

Figure 4.41: Cross-sectional TEM images of ZnO nanowires grown on ZnO seed layer coated FTO substrate (a) Low-magnification image of ZnO nanowire/seed layer interface, (b, e) HRTEM image and (c, d) SAED pattern of ZnO nanowire and ZnO seed layer.

Fig 4.42 shows the high-magnification cross-sectional SEM and TEM images of aligned ZnO nanowire arrays, where the ZnO nanowires are clearly seen to grow directly on the seed layer grains. Strong evidence confirming that the ZnO nanowire diameter is directly influenced by the seed layer grain size is provided in Fig 4.42(a). The average diameter of the ZnO nanowire and the seed grain size were estimated from nanowire/seed layer interfaces using cross-sectional electron microscopy. The SEM image shows a similar relationship between the nanowire diameter and seed grain size, as shown in Fig 4.42(b).

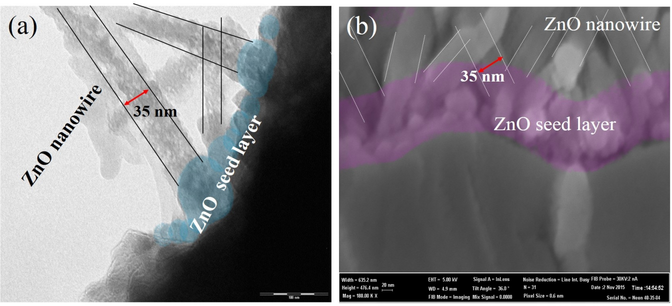

Figure 4.42: High magnification electron microscopy image of a nanowire grown on a ZnO seed layer coated FTO substrate.

Fig 4.43(a) presents low-magnification cross-sectional TEM image of ZnO nanowalls synthesized on the Al-ZnO seed layer coated FTO substrate by hydrothermal method at 95^oC for 2 h. It can be seen that the nanowalls are vertically aligned on the FTO substrate. All the nanowalls have similar overall dimensions and hexagonal nanowalls exhibit excellent in-plane crystallographic alignment resulting from the symmetry and lattice match at the interface. The square region of Fig 4.43(a) represents the selected area apertures used in the TEM analysis. The corresponding SAED patterns are shown in Fig 4.43(c, d). The ZnO nanowalls are perpendicular to the substrate, as shown in Fig 4.43(a). The SAED obtained from the nanowall (SAED1) and the Al-ZnO seed layer (SAED2) of the sample reveals a single crystal ZnO with a wurtzite structure. The HRTEM images presented in Fig 4.43(b, e) clearly show the lattice fringes. From Fig 4.43(e), the interplanar spacing of 0.522 nm can be measured for the nanowall and the seed layer, which corresponds to the wurtzite ZnO (0001) plane [119, 120].

TEM characterization does not provide any evidence for the nanowall growth seen on the single grain of Al-ZnO seed substrate. The nanowall was grown on top of the seed layer arrays, with no evident influence of the seed grain size and nanowall thickness. Fig 4.44 shows the interface between Al-ZnO and nanowall, without a clear boundary and no evidence of the origin of the nanowall growth.

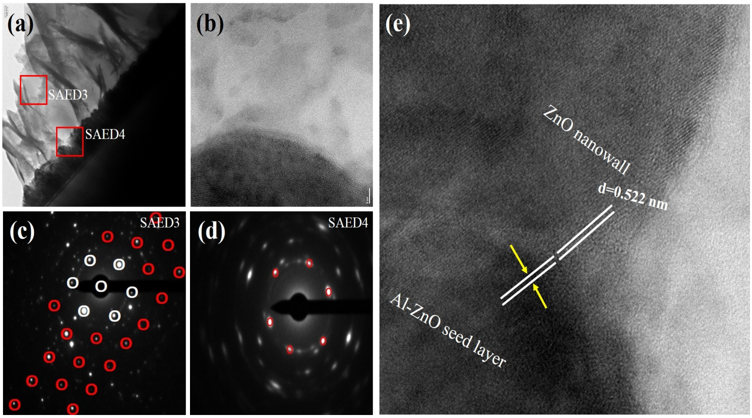

Figure 4.43: Cross-sectional TEM images of ZnO nanowalls grown on Al-ZnO seed layer coated FTO substrate (a) Low-magnification image of ZnO nanowall/seed layer interface, (b, e) HRTEM image and (c, d) SAED pattern of ZnO nanowall and Al-ZnO seed layer.

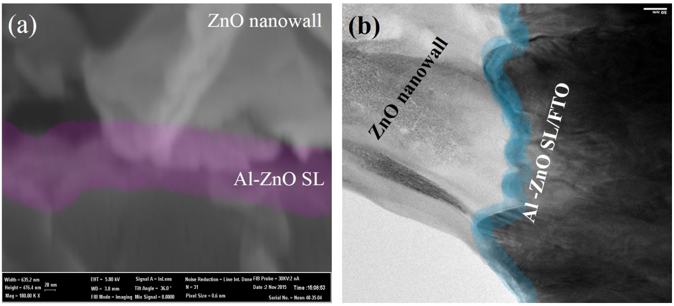

Figure 4.44: High magnification electron microscopy image of ZnO nanowalls grown on the Al-ZnO seed layer coated FTO substrate.

Well-aligned ZnO nanostructures have been synthesized using the low-temperature solution approach. The morphologies of ZnO nanostructures are seen to be strongly affected by the chemical nature of the seed layer. By varying Al content in the seed layer, the morphology of the ZnO nanostructure is gradually changed from 1D nanowire to 3D nanowall arrays. SEM observations revealed that well-aligned ZnO nanostructures can be obtained using the optimized synthesis parameters and a seed layer. XRD spectra and HRTEM observations revealed a preferred orientation of the ZnO nanostructure toward the c-axis of the wurtzite structure, while also showing single crystallinity and growth direction of the as-grown ZnO nanostructure.

4.5 Solution processed large area DSSCs

The advantage of spray coating and solution growth of aligned nanostructures is the ability to scale up the process in a cost-effective manner. As a proof of concept, aligned ZnO nanostructures were grown on 50 mm × 50 mm size FTO substrate and were employed as a photoanode in DSSCs. For the fabrication of functioning DSSCs, a catalytic counter electrode with similar dimensions is an equally important component. A thin layer of Pt deposited on FTO substrate is usually employed as a counter electrode for tri-iodide reduction in DSSCs. Low abundance and the high cost of this noble metal restrict its suitability for large-area DSSCs. The potential application of reduced graphene oxide (rGO) as an alternative counter electrode material in large area DSSCs was investigated. A low-cost and scalable method for preparing large-area graphene CE on an FTO substrate via spray coating and the large area graphene oxide (GO) film are reduced by the sunlight reduction technique.

4.5.1 Large-area photoanode

Initially, the 50 mm × 50 mm size FTO substrates were seeded with an oriented ZnO seed layer using spray coating. Prior to commencing this process, FTO substrates were ultrasonically cleaned in ethanol and acetone for 15 min, respectively. The seed layer precursor solution was prepared using 0.1 M zinc acetate dihydrate in methanol at room temperature. The obtained transparent solution was sprayed onto the cleaned FTO substrate maintained at 350^oC with the help of a hotplate, using a portable spray gun connected with an argon cylinder. Finally, the seed layer deposited FTO substrates were annealed at 350^oC for 20 min for 1 h to obtain the oriented ZnO seed layers. The solution for growing ZnO nanowires was prepared by dissolving equimolar ratio of 0.025 M zinc nitrate hexahydrate and hexamethylenetetramine in Di-water. The ZnO seed layer deposited FTO substrate was immersed in the solution, where the ZnO/FTO side was placed face down, and the plastic container was kept at 95^oC for 3 h. After the reaction, ZnO nanowires grown on FTO substrates were rinsed with Di-water and were annealed at 350^oC for 20 min. Fig 4.45(a) shows the photograph of ZnO nanowires grown on the FTO substrate, revealing that the substrate exhibits uniform growth without any patches. Surface and cross-sectional FESEM images shown in Fig 4.45(b) and (c) indicate that well-aligned ZnO nanowire arrays with high density are observed on the surface of the substrate. Almost all ZnO nanowires are perpendicular to the substrate and have a uniform length of 2μm.

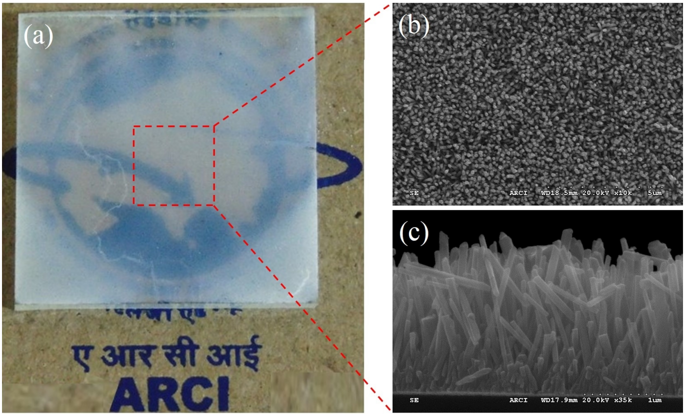

Figure 4.45: (a) Photograph, and (b, c) surface and cross-sectional SEM image of ZnO nanowire grown on 50 mm × 50 mm size FTO substrate.

4.5.2 Large-area counter electrode

In order to achieve high efficiency in DSSCs, the counter electrode (CE) should be catalytic to the regeneration reaction of the redox mediator. Platinum is usually employed as a CE of DSSCs. However, Pt is expensive, and it degrades in a corrosive electrolyte. Gratzel et al. were the first to investigate carbonaceous materials such as carbon black and carbon nanotubes (CNTs) as a replacement for Pt as the CE of DSSCs. The carbonaceous materials are inexpensive, chemically inert, electrocatalytically active and more stable in the corrosive electrolyte. However, carbon black and CNTs based CEs have low specific catalytic activity towards tri-iodide reduction, presumably due to their intrinsic chemical structure. Later, various two-dimensional forms of carbon materials, such as few layer graphite, GO, and graphene, were investigated as the CE in DSSCs. These materials have the advantage of large surface area, abundant catalytic sites, and improved electrical conductivity. Remarkable mechanical properties of 2D carbon materials offer further advantages for the fabrication of flexible CEs. The first work on the application of graphene as the CE in DSSCs was reported by Roy-Maythew et al. in 2010 [121]. The device showed energy conversion efficiency of 4.99%, which is similar to that of the control DSSC with Pt as the CE. The catalytic activity of graphene is related to its defects. Nitrogen doping can introduce defects in graphene and increase the catalytic activity. Wang et al. employed n-doped graphene (n-rGO) as a CE for DSSCs and demonstrated 7.01% efficiency, which is comparable to that of 7.34% Pt-CE DSSC [122, 123]. Recently, Kavan et al. used graphene nanoplatelets as a CE for DSSC and demonstrated 9.4% efficiency, which exceeds 8.2% obtained with Pt-CE based control cell.The graphene nanoplate layer is superior to Pt both in terms of electrocatalysis and electrochemical stability under prolonged potential cycling test conditions [124].

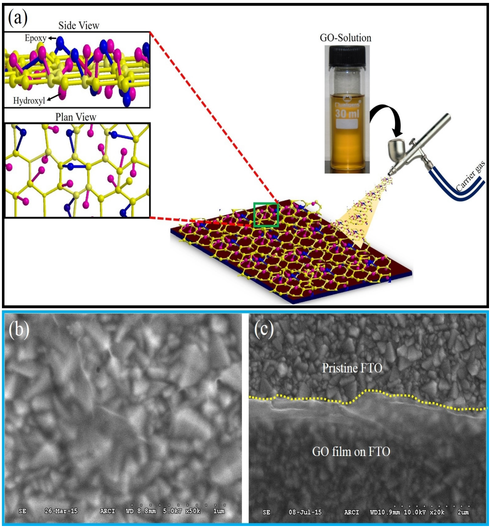

Figure 4.46: (a) Schematic of GO coated FTO substrate by spray coating, and (c, d) SEM image corresponding substrate.

A convenient way to make graphene in any usable quantity is achieved through the reduction of GO sheets. Well-known GO reduction methods include chemical and thermal reduction. The obtained graphene sheets are subsequently dispersed in an organic solvent and deposited on the desired substrate. The spray-coating approach allows for fast and efficient deposition of rGO sheets onto substrates of virtually any size. GO was prepared from exfoliated graphite using modified Hummers method and was dispersed in ethanol [125]. The resultant GO solution was sprayed as a continuous film on FTO substrate at 80^{-1}C on a hot plate. As-prepared GO sheets are characterized by oxygen-containing hydroxyl and epoxy functional groups. These functional groups are randomly distributed on both sides of GO sheet, as schematically shown in Fig 4.46(a). The functional groups affect the conductivity and electrochemical activity of GO film [121]. The surface morphology of GO films was investigated using SEM. The underlying FTO grains were clearly visible, indicating thin and tightly packed, transparent GO sheets, as shown in Fig 4.46(b). The SEM images show that the GO film is composed of multiple sheets positioned one on top of the other. Fig 4.46(c) shows the bare and GO covered portion of the FTO substrate. The thickness of GO film was found to be around 100 nm.

In addition to the deposition of GO on the FTO substrate, the reduction of GO film is also very important, as different reduction processes affect the final material performance. Recently, Sun et al. reported on the efficient route for the reduction of large-area GO films through a sustainable and chemical-free process. They proposed that GO film could be swiftly reduced using sunlight as an irradiation source [79]. In the present study, a similar approach was employed to fabricate large-area rGO layer counter electrode for DSSCs. Fig 4.46(a) shows the schematic setup for reduction of GO films by sunlight irradiation. The photoreduction of the GO film was carried out using focused sunlight irradiation. The sunlight was directly focused on the GO film surface by using 85 mm-diameter magnifying lens and focus spot diameter of approx. 10 mm, which could be demonstrated by the fast color change from yellow-brown to black. By further increasing the irradiation time from 0 to 1800 s, the GO film transmittance decreased, as shown in Fig 4.48(a). After irradiation of 0, 600 and 1800s, these films were characterized, while the reduction properties were assessed through the electron microscopy, XRD, and Raman spectroscopy. The surface morphology of the GO film irradiated for 600 and 1800s was evaluated through SEM. The surface morphology was similar, but the visible transmittance decreased for the

GO film irradiated for 1800s. The underlying FTO grains were visible but slightly darker than those in the GO film, as shown in Fig 4.46(b, c).

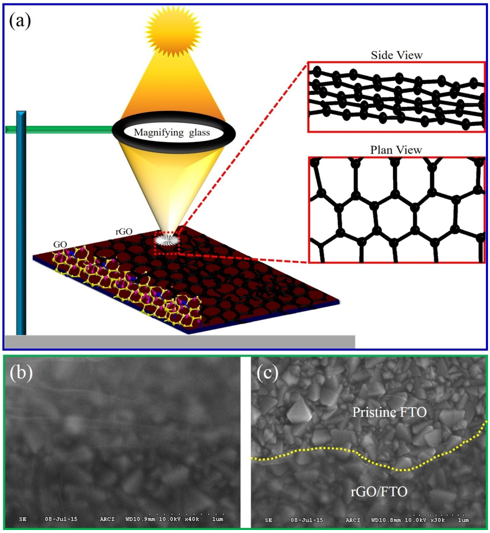

Figure 4.47: (a) Schematic setup for reduction of GO film using sunlight and functional groups removed from GO sheet, and (b, c) SEM image of the GO film on FTO substrate after reduction.

Raman spectroscopy has been extensively used for characterizing sp^2 and sp^3 hybridized carbon atoms including those in carbon-based materials. Clearly, the two distinct peaks observed at 1329 and 1589 cm^{-1} correspond to the D and G bands, respectively, as shown in Fig 4.48(b). The G band is characteristic of C-C bond in graphitic-like structures, whereas the D-band is caused by the disordered structure of graphene and thus makes Raman spectroscopy one of the most sensitive techniques to characterize disorders in sp^3 carbon materials. The subtraction of functional groups would lead to the partial recovery of sp^2 domains, represented by an obvious decrease in the D/G intensity ratio (I_D/I_G). The (I_D/I_G) ratio of rGO film is decreased with increasing the irradiation time 0 to 600sec, due to the functional groups removed from the GO sheets. By further increasing the irradiation time from 600s to 1800s, the (I_D/I_G) ratio was increased from 0.94 to 0.96. This change may be attributed to the GO sheet damage and higher disorder structure [126], as shown in Fig 4.49. The electrical properties of GO-coated FTO substrates were also investigated using the Keithley source-measure unit and the I-V characteristics are shown in Fig 4.48(c). The etched FTO substrate on deposited GO film (0.36 cm^2 area) resulted in transparent GO films irradiated for three different time periods. The GO films were irradiated for 0, 600 and 1800s, whereby those irradiated for 600 s showed higher current (0.003 mA) as the functional groups in GO sheets were removed. After being continuously irradiated for 1800s, films showed lower current (0.0025 mA) because of higher presence of defects in GO sheets (Fig 4.49).

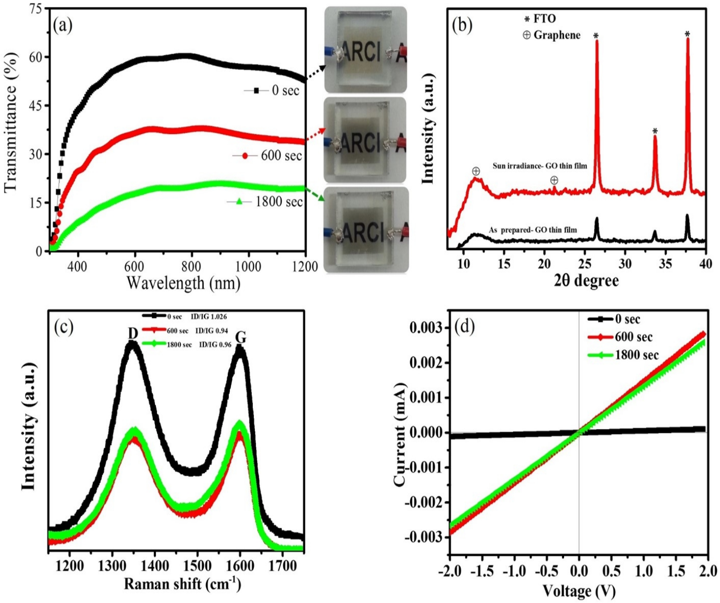

Figure 4.48: (a) UV-vis transmittance spectra and photographic image, (b) XRD patterns (b) Raman spectra, (c) current–voltage characteristics of GO films irradiated for three different time periods.

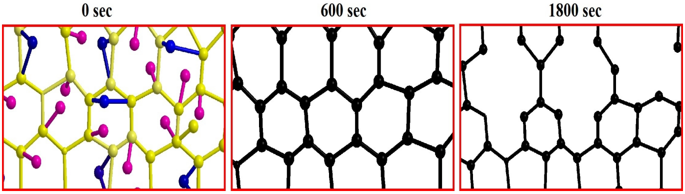

Figure 4.49: Schematic of GO film exposed to sunlight for three different irradiation time periods.

Fig 4.48(d) shows the structural characterization of the GO film before and after reduction for 600s. The XRD data pertaining to the GO film reveals a layered nanostructure, as indicated by a broad diffraction peak at $2\Theta = 11.8^o$, which corresponds to d-spacing of 0.75 nm. However, after reduction, the rGO film shows peaks at $2\Theta = 11.8^o$ and $2\Theta = 24.3^o$. The higher degree peak indicates a significant decrease in the interlayer spacing of the rGO sheets (d-spacing $\approx$0.37 nm) after the removal of functional groups [79]. Broadening of the diffraction peak is also noted, which could be attributed to the smaller sheet size and the irregular stacking of rGO sheets.

The GO film was dipped in ethanol and sonicated for 10 min. TEM samples were prepared by drop casting, whereby a few drops of the ethanol-GO were placed onto lacey carbon-coated grids. Fig 4.50(a) shows the TEM image of GO sheet, which appears thin and transparent to the electrons. The HRTEM image of the same GO sheet revealed its amorphous nature [127], which was confirmed by the SAED pattern shown in Fig 4.50(b, c). After the reduction, the GO film was used for TEM analysis, as shown in Fig 4.50(d). The rGO sheets are thin and more extensive edge defects can be observed. The HRTEM image provides an accurate way to measure the number of layers at multiple locations on the edge of the sheet and also revealed that the rGO sheet is 4-layered, as shown in Fig 4.50(e). The SAED pattern of the rGO sheet reveals a hexagonal pattern, confirming the three-fold symmetry of the arrangement of carbon atoms. When different regions of the rGO sheet are examined, well-defined diffraction spots are always observed, indicating crystallinity of all regions examined. Stacking disorder of graphene layers in multilayer regions is suggested by the appearance of electron diffraction spots mis-aligned with respect to each other. Green arrows indicate secondary diffraction spots observed due to a random orientation between adjacent graphene layers, as shown in Fig 4.50(f) [128].

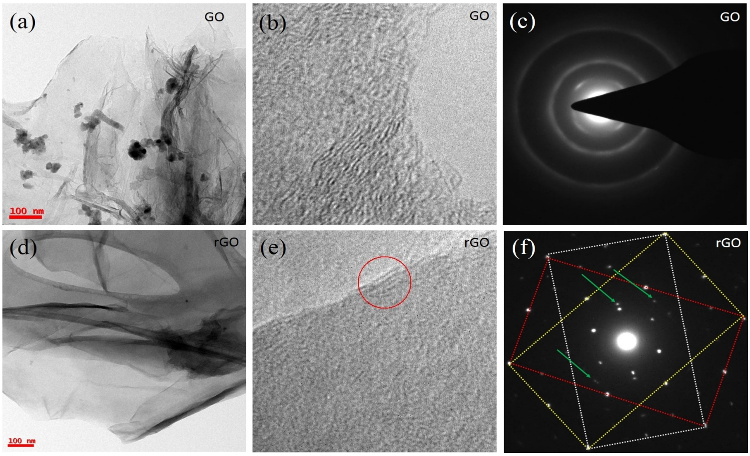

Figure 4.50: TEM image of (a, d) GO and rGO sheet and , (b, c, e and f) HRTEM images, SAED pattern of the corresponding GO and rGO sheet irradiated for 0 and 600 sec.

The irradiated GO films were used for 0.36 cm^2 area DSSCs as CEs, as shown Fig 4.51(a). Fig 4.51(b) shows the performance of DSSCs with different CEs under 1 sun illumination condition AM 1.5 and power Pin of 100 $mW.cm^{-2}$. DSSC with 600 sec irradiated GO CE shows 2.23% overall light to electric energy conversion efficiency, which is comparable to 5.2% obtained with a Pt CE device. Regardless of illumination condition, J_{sc} of rGO CE DSSC is higher than that of Pt CE and demonstrated a low-cost DSSC using rGO CE with 2.23% energy conversion efficiency accompanied by good stability. Moreover, this electrode exhibits low charge transfer resistance, owing to its high surface area.

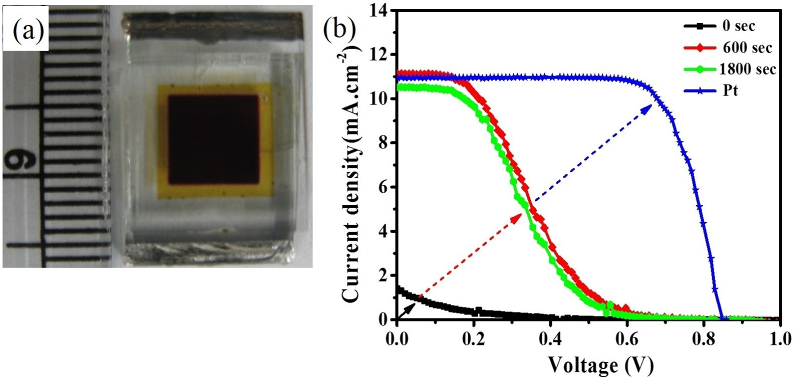

Figure 4.51: (a) photograph, and (b) I-V characteristics of 6 mm × 6 mm size graphene-based DSSCs.

If the DSSCs is scaled up to several square centimeters, the FTO resistance increases, leading to low fill factor (FF) and low conversion efficiency, as reported by Gratzel et al. [129, 130]. To reduce the resistance of FTO for large-area DSSCs, stripe type aligned ZnO nanostructures, TiO_2 electrode, and graphene based CE were prepared with current-collecting metal (Ag) fingers on FTO glass, as shown in Fig 4.52. The photovoltaic performance of a module fabricated with rGO based TiO_2 DSSC was used as a reference, while those fabricated with rGO served as CE for ZnO nanostructure based DSSC. Fig 4.53 shows the photovoltaic characteristics of the DSSCs with Ag fingers [131]. The V_{oc}, J_{sc}, FF and efficiency were summarized in Table 4.8. The results indicate that ZnO nanostructure-DSSC with graphene CE exhibit 0.13% overall light to electric energy conversion efficiency, which is comparable to 1.2 % of the graphene CE based TiO_2 device. Thus, this work demonstrated a low-cost dye-sensitized solar cell using graphene counter electrode with 1.2% for TiO_2 and 0.13 % for ZnO nanostructure, energy conversion efficiency and good stability. In addition, this electrode exhibits low charge transfer resistance, owing to its high surface area. The aligned ZnO nanostructure based DSSC shows lower efficiency, which is due the lower surface area, lower dye loading and higher recombination.

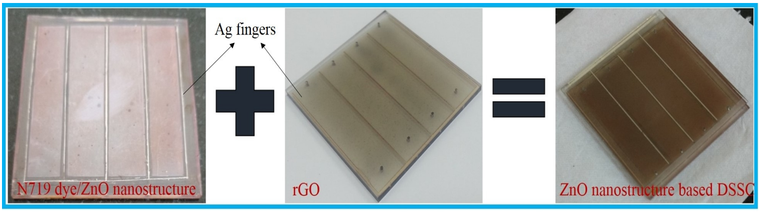

Figure 4.52: (a) Photograph of 50 mm × 50 mm size graphene-based ZnO nanostructre DSSC

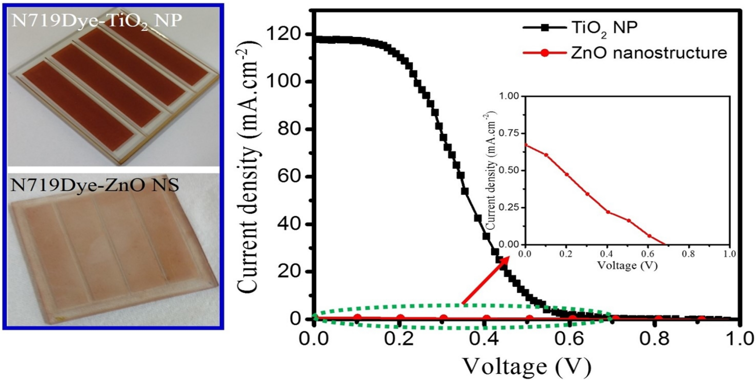

Figure 4.53: (a) Photograph of TiO_2 and ZnO nanostructure after dye adsorption, and (b) I-V characteristics of 50 mm × 50 mm size graphene-based DSSCs.

Table 4.8: The Graphene based ZnO, TiO_2 nanostructres DSSC detailed device parameters and active area=25 cm^2 for ZnO, 15.2 cm^2 for TiO_2

.

DSSC	V_{oc} (mV)	J_{sc} ($mA.cm^{-2}$)	FF	n(%)
ZnO nanostructure	0.68	0.67	0.29	0.13
TiO_2	0.65	116	0.25	1.2

A large-area dye-sensitized solar cell module based on spray-coated graphene counter electrode was developed. The GO solution was prepared using the modified Hummers method. Graphene film was deposited on FTO substrate by spray coating to realize a large-area counter electrode with a transparency of 50%. The large-area DSSCs module achieved a η of 1.2% for TiO_2 and ZnO for 0.13%. In terms of the performance/cost ratio of photovoltaic devices, the GO solution can be a viable alternative to current technology based on Pt. Moreover, the use of iodine-based mediator could boost the performances of DSSC modules, as already demonstrated for lab-scale DSSC devices. Further optimization of graphene-based ink formulations and their deposition methods on both rigid and flexible substrates will pave the way for the development of all-printed, flexible, and transparent graphene-based photovoltaic devices on arbitrary substrates.

Chapter 5

Conclusion and outlooks

The objective of this work was to develop aligned nanostructures as the electron transport layer in dye and perovskite solar cells. Aligned ZnO nanostructure arrays were chosen as a more appropriate candidate for this application, dye to serving as a good sensitizer scaffold and an electron transporting layer in third-generation solar cells. In addition, the aligned ZnO nanostructures synthesized on the spray-coated seed layer by solution-based approach could be produced in a cost-effective manner. The conclusions yielded by this work can be summarized as follows.

- To obtain well-aligned ZnO nanostructures grown on TCO substrate, the seed layer is necessary for alignment and control of the ZnO nanostructure morphology, which was realized in this work. Such aligned ZnO nanostructure was demonstrated to be beneficial for electron transport in dye and perovskite solar cells.

- By changing Al content in the seed layer, the ZnO nanostructure morphology can be gradually changed from 1D nanowire to 3D nanowall arrays. The ZnO nanowalls are novel building blocks for devices that require not only efficient carrier transport path but also the greater surface area. Dye and perovskite solar cells were fabricated using ZnO nanowalls that exhibit higher photocurrent density (J_{sc}) and PCE than the 1D ZnO nanowire-based devices.

- I-V characteristics of aligned ZnO nanowires with ZnO and Al-ZnO seed layer of dye-sensitized solar cells were studied in the dark and under simulated solar light. The DSSC with Al-ZnO seed layer exhibited lower recombination than that with the ZnO seed layer, as the seed layer was electrically conductive. The electrical properties of nanostructure/seed layer were characterized through the C-AFM.

- The growth mechanism of ZnO nanostructures, alignment and crystalline structure were characterized by electron microscopy and XRD.

- Solar irradiated GO films open the potential for replacing platinum CEs in the DSSCs of similar efficiency, thus facilitating the use of graphene-based materials for large-scale applications.

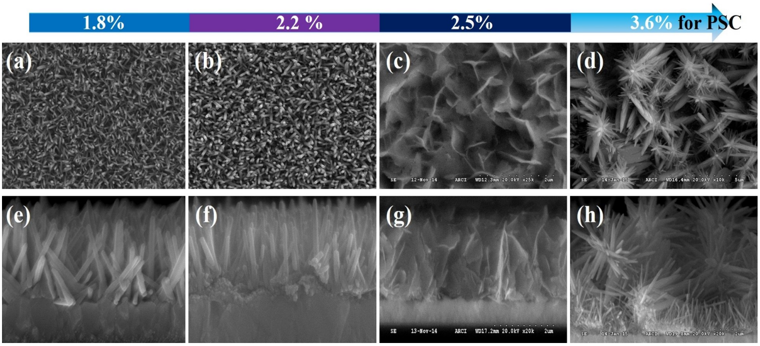

Figure 5.1: SEM images of ZnO nanostructures (a)nanowires on ZnO seed layer, (b) nanowires on (1 %)Al-ZnO seed layer, (c)nanowalls on 3(%) Al-ZnO seed layer, (d)Hybrid ZnO nanostructures on 3(%)Al-ZnO seed layer, and (e-h)cross-sectional image of the corresponding ZnO nanostructures and ZnO nanostructures wrt to efficiency.

5.0.1 Outlooks

It is believed that, with due optimization, aligned ZnO nanostructures grown on Al-ZnO seed layer will pave the way for greater advancements in device structure and energy conversation efficiency.

- For growth of ZnO nanowall on arbitrary substrates, the high temperature is not needed. The initial results demonstrated in this thesis can be reproduced in electron transport layer in dye and perovskite solar cells.

- It would be beneficial to conduct further studies aiming to establish if the replacement of TiO_2 electrode by aligned hybrid ZnO nanostructure could enhance the performance of dye and perovskite solar cells.

- Future development of novel Al-ZnO/graphene composite bi-functional (TCO seed) layer for the optoelectronic application is also recommended.

Bibliography

1. British Petroleum. Primary energy consumption - leading countries 2014. Br. Pet. 48 **(2015)**. doi:bp.com/statisticalreview.
2. Foley, T. et al. REN12-GSR2015-Onlinebook-low. **(2015)**.
3. Jacobson, M. Z. & Delucchi, M. A. Providing all global energy with wind, water, and solar power, Part I: Technologies, energy resources, quantities and areas of infrastructure, and materials. Energy Policy 39, 1154–1169 **(2011)**.
4. Becquerel. Recherches sur les effets de la radiation chimique de la lumiere solaire au moyen des courants electriques. Comptes Rendus LAcademie des Sci. 9, **(1839)**.
5. Norton, J. D. Einstein's Miraculous Argument of 1905 The Papers of Einstein's Year of Miracles , 1905. 1–46 **(1905)**.
6. Sze, S. M. Semiconductor Devices: Physics and Technology. Technology **(2006)**. doi:10.1016/S0026-2692(82)80036-0
7. Zhou, Y. & Zhu, K. Perovskite Solar Cells Shine in the 'Valley of the Sun'. ACS Energy Lett. 64–67 **(2016)**. doi:10.1021/acsenergylett.6b00069
8. Beard, M. C. & Ellingson, R. J. Multiple exciton generation in semiconductor nanocrystals: Toward efficient solar energy conversion. Laser Photonics Rev. 2, 377–399 **(2008)**.
9. Wurfel, P. & Wurfel, U. Physics of solar cells: from basic principles to advanced concepts. (Wiley-VCH, **2009**).
10. Shockley, W. & Queisser, H. J. Detailed balance limit of efficiency of p-n junction solar cells. J. Appl. Phys. 32, 510–519 **(1961)**.
11. Henry, C. H. Limiting efficiencies of ideal single and multiple energy gap terrestrial solar cells. J. Appl. Phys. 51, 4494–4500 **(1980)**.
12. Green, M. A., Emery, K., Hishikawa, Y., Warta, W. & Dunlop, E.

D. Solar cell efficiency tables (version 48). Prog. Photovoltaics Res. Appl. 24, 905–913 **(2016)**.
13. Marti, A. & Araujo, G. L. Limiting efficiencies for photovoltaic energy conversion in multigap systems. Sol. Energy Mater. Sol. Cells 43, 203–222 **(1996)**.
14. Brown, A. S. & Green, M. A. Detailed balance limit for the series constrained two terminal tandem solar cell. Phys. E Low-Dimensional Syst. Nanostructures 14, 96–100 **(2002)**.
15. O'Regan, B. & Gratzel, M. A low-cost, high-efficiency solar cell based on dye-sensitized colloidal TiO_2 films. Nature 353, 737–740 **(1991)**.
16. Kochuveedu, S. T., Jang, Y. H. & Kim, D. H. A study on the mechanism for the interaction of light with noble metal-metal oxide semiconductor nanostructures for various photophysical applications. Chem. Soc. Rev. 42, 8467–93 **(2013)**.
17. Gregg, B. A. Excitonic Solar Cells. J. Phys. Chem. B 107, 4688–4698 **(2003)**.
18. Frank, A. J., Kopidakis, N. & Lagemaat, J. Van De. Electrons in nanostructured TiO_2 solar cells: Transport, recombination and photovoltaic properties. Coord. Chem. Rev. 248, 1165–1179 **(2004)**.
19. Boschloo, G., Hagfeldt, A. & Spectus, C. O. N. Characteristics of the Iodide / Triiodide Redox Mediator in Dye-Sensitized Solar Cells. Acc. Chem. Res. 42, 1819–1826 **(2009)**.
20. Wang, M. et al. An organic redox electrolyte to rival triiodide/iodide in dye-sensitized solar cells. Nat. Chem. 2, 385–389 **(2010)**.
21. Akihiro Kojima, Kenjiro Teshima, Yasuo Shirai, & T. M. Organometal Halide Perovskites as Visible- Light Sensitizers for Photovoltaic Cells. J Am Chem Soc 131, 6050–6051 **(2009)**.
22. Poglitsch, A. & Weber, D. Dynamic disorder in methylammoniumtrihalogenoplumbates (II) observed by millimeter-wave spectroscopy. J. Chem. Phys. 87, 6373 **(1987)**.
23. Kawamura, Y., Mashiyama, H. & Hasebe, K. Structural Study on Cubic–Tetragonal Transition of $CH_3NH_3PbI_3$. J. Phys. Soc. Japan 71, 1694–1697 **(2002)**.
24. Schulz, P. et al. Interface energetics in organo-metal halide perovskite-based photovoltaic cells. Energy Environ. Sci. 7, 1377–1381

(2014).
25. D'Innocenzo, V. et al. Excitons versus free charges in organo-lead tri-halide perovskites. Nat. Commun. 5, 3586 **(2014)**.
26. Tanaka, K. et al. Comparative study on the excitons in lead-halide-based perovskite-type crystals $CH_3NH_3PbBr_3$ CH3NH 3PbI3. Solid State Commun. 127, 619–623 **(2003)**.
27. Mitzi, D. B., Feild, C. a., Harrison, W. T. a. & Guloy, a. M. Conducting tin halides with a layered organic-based perovskite structure. Nature 369, 467–469 **(1994)**.
28. Alcocer, M. J. P., Leijtens, T., Herz, L. M., Petrozza, A. & Snaith, H. J. Electron-Hole Diffusion Lengths Exceeding Trihalide Perovskite Absorber. 341, **(2014)**.
29. Kim, H.-S. et al. Mechanism of carrier accumulation in perovskite thin-absorber solar cells. Nat. Commun. 4, 2242 **(2013)**. 30. Im, J.-H., Lee, C.-R., Lee, J.-W., Park, S.-W. & Park, N.-G. 6.5% Efficient Perovskite Quantum-Dot-Sensitized Solar Cell. Nanoscale 3, 4088 **(2011)**.
31. Kim, H.-S. et al. Lead iodide perovskite sensitized all-solid-state submicron thin film mesoscopic solar cell with efficiency exceeding 9%. Sci. Rep. 2, 591 **(2012)**.
32. Lee, M. M., Teuscher, J., Miyasaka, T., Murakami, T. N. & Snaith, H. J. Efficient hybrid solar cells based on meso-superstructured organometal halide perovskites. Science 338, 643–647 **(2012)**.
33. Burschka, J. et al. Sequential deposition as a route to high-performance perovskite-sensitized solar cells. Nature 499, 316–320 **(2013)**.
34. Saliba, M. et al. Cesium-containing Triple Cation Perovskite Solar Cells: Improved Stability, Reproducibility and High Efficiency. Energy Environ. Sci. 9,**(2016)**.
35. Qian, L., Zheng, Y., Xue, J. & Holloway, P. H. Stable and efficient quantum-dot light-emitting diodes based on solution-processed multilayer structures. Nat. Photonics 5, 543–548 **(2011)**.
36. Nazeeruddin, M. K., Baranoff, E. & Gratzel, M. Dye-sensitized solar cells: A brief overview. Sol. Energy 85, 1172–1178 **(2011)**.
37. Jang, K. Il, Hong, E. & Kim, J. H. Effect of an electrodeposited TiO2 blocking layer on efficiency improvement of dye-sensitized solar cell. Korean J. Chem. Eng. 29, 356–361 **(2012)**.

38. Cameron, P. J. & Peter, L. M. Characterization of titanium dioxide blocking layers in dye-sensitized nanocrystalline solar cells. J. Phys. Chem. B 14394–14400 **(2003)**. doi:10.1021/jp030790+

39. Wang, H. et al. Single-crystalline rutile TiO_2 hollow spheres: Room-temperature synthesis, tailored visible-light-extinction, and effective scattering layer for quantum dot-sensitized solar cells. J. Am. Chem. Soc. 133, 19102–19109 **(2011)**.

40. Kalyanasundaram, K. Applications of functionalized transition metal complexes in photonic and optoelectronic devices. Coord. Chem. Rev. 177, 347–414 **(1998)**.

41. Lee, J. H. et al. Thickness effect of the TiO_2 nanofiber scattering layer on the performance of the TiO_2 nanoparticle/TiO_2 nanofiber-structured dye-sensitized solar cells. Curr. Appl. Phys. 14, 856–861 **(2014)**.

42. Yan, K., Qiu, Y., Chen, W., Zhang, M. & Yang, S. A double layered photoanode made of highly crystalline TiO_2 nanooctahedra and agglutinated mesoporous TiO2 microspheres for high efficiency dye sensitized solar cells. Energy Environ. Sci. 4, 2168 **(2011)**.

43. Faglia, G. Nanostructured materials improve efficiency in excitonic solar cells. SPIE Newsroom 2, 5–6 **(2010)**.

44. Wang, H. et al. Rutile TiO_2 nano-branched arrays on FTO for dye-sensitized solar cells. Phys. Chem. Chem. Phys. 13, 7008–7013 **(2011)**.

45. Chen, H. & Yang, S. Hierarchical Nanostructures of Metal Oxides for Enhancing Charge Separation and Transport in Photoelectrochemical Solar Energy Conversion Systems. Nanoscale Horiz. 1, 96–108 **(2016)**.

46. Zhang, Q. & Cao, G. Nanostructured photoelectrodes for dye-sensitized solar cells. Nano Today 6, 91–109 **(2011)**.

47. Huang, S. Y., Schlichthorl, G., Nozik, a J., Gratzel, M. & Frank, a J. Charge recombination in dye-sensitized nanocrystalline TiO2 solar cells. J. Phys. Chem. B 101, 2576–2582 **(1997)**.

48. Xu, J., Chen, Z., Zapien, J. A., Lee, C. S. Zhang, W. Surface engineering of ZnO nanostructures for semiconductor-sensitized solar cells. Adv. Mater. 26, 5337–5367 **(2014)**.

49. Morkoc, H. & Ozgur, U. General Properties of ZnO. Zinc Oxide: Fundamentals, Materials and Device Technology **(2009)**.

50. Tang, C., Spencer, M. J. S. & Barnard, A. S. Activity of ZnO polar surfaces: an insight from surface energies. Phys. Chem. Chem. Phys. 16, 22139–44 **(2014)**.
51. Sohn, J. I. et al. Surface energy-mediated construction of anisotropic semiconductor wires with selective crystallographic polarity. Sci. Rep. 4, 5680 **(2014)**.
52. Ding, Y., Pradel, K. C. & Wang, Z. L. In situ transmission electron microscopy observation of ZnO polar and non-polar surfaces structure evolution under electron beam irradiation. J. Appl. Phys. 119, **(2016)**.
53. Wang, X., Summers, C. J. & Wang, Z. L. Large-scale hexagonal-patterned growth of aligned ZnO nanorods for nano-optoelectronics and nanosensor arrays. Nano Lett. 4, 423–426 **(2004)**.
54. Yang, B. P. et al. Controlled Growth of ZnO Nanowires and Their Optical Properties. 323–331 **(2002)**.
55. Vayssieres, L. Growth of arrayed nanorods and nanowires of ZnO from aqueous solutions. Adv. Mater. 15, 464–466 **(2003)**.
56. Mai, W. et al. Vertically aligned ZnO nanowire arrays on GaN and SiC substrates. Chem. Phys. Lett. 460, 253–256 **(2008)**.
57. Schwenzer, B., Gomm, J. R. & Morse, D. E. Substrate-induced growth of nanostructured zinc oxide films at room temperature using concepts of biomimetic catalysis. Langmuir 22, 9829–9831 **(2006)**.
58. Song, J. & Lim, S. Effect of Seed Layer on the Growth of ZnO Nanorods. J. Phys. Chem. C 111, 596–600 **(2007)**.
59. Breedon, M., Rahmani, M. B., Keshmiri, S. H., Wlodarski, W. & Kalantar-zadeh, K. Aqueous synthesis of interconnected ZnO nanowires using spray pyrolysis deposited seed layers. Mater. Lett. 64, 291–294 **(2010)**.
60. Law, M., Greene, L. E., Johnson, J. C., Saykally, R. & Yang, P. Nanowire dye-sensitized solar cells. Nat. Mater. 4, 455–459 **(2005)**.
61. Seol, M., Kim, H., Tak, Y. & Yong, K. Novel nanowire array based highly efficient quantum dot sensitized solar cell. Chem. Commun. (Camb). 46, 5521–5523 **(2010)**.
62. Akhtar, M. S., Khan, M. A., Jeon, M. S. & Yang, O. B. Controlled synthesis of various ZnO nanostructured materials by capping agents-assisted hydrothermal method for dye-sensitized solar cells. Electrochim. Acta 53, 7869–7874 **(2008)**.

63. Xu, C., Wu, J., Desai, U. V. & Gao, D. Multilayer assembly of nanowire arrays for dye-sensitized solar cells. J. Am. Chem. Soc. 133, 8122–8125 **(2011)**.

64. Fu, Y. S. et al. ZnO hierarchical nanostructures and application on high-efficiency dye-sensitized solar cells. Mater. Sci. Eng. B Solid-State Mater. Adv. Technol. 166, 196–202 **(2010)**.

65. Gan, X., Li, X., Gao, X., Zhuge, F. & Yu, W. ZnO nanowire/TiO_2 nanoparticle photoanodes prepared by the ultrasonic irradiation assisted dip-coating method. Thin Solid Films 518, 4809–4812 **(2010)**.

66. Xu, F., Dai, M., Lu, Y. & Sun, L. Hierarchical ZnO Nanowire-Nanosheet Architectures for High Power Conversion Efficiency in Dye-Sensitized Solar Cells. J. Phys. Chem. C 114, 2776–2782 **(2010)**.

67. Liu, D. & Kelly, T. L. Perovskite solar cells with a planar heterojunction structure prepared using room-temperature solution processing techniques. Nat. Photonics 8, 133–138 **(2013)**.

68. Zhou, H. et al. Interface engineering of highly efficient perovskite solar cells. Sci. (Washington, DC, U. S.) 345, 542–546 **(2014)**.

69. Riveros, R., Romero, E. & Gordillo, G. Synthesis and characterization of highly transparent and conductive SnO2:F and In2O3:Sn thin films deposited by spray pyrolysis. Brazilian J. Phys. 36, 1042–1045 **(2006)**.

70. Byrappa, K. & Adschiri, T. Hydrothermal technology for nanotechnology. Prog. Cryst. Growth Charact. Mater. 53, 117–166 **(2007)**.

71. Liu, J., She, J., Deng, S., Chen, J. & Xu, N. Ultrathin seed-layer for tuning density of ZnO nanowire arrays and their field emission characteristics. J. Phys. Chem. C 112, 11685–11690 **(2008)**.

72. Xu, S. & Wang, Z. L. One-dimensional ZnO nanostructures: Solution growth and functional properties. Nano Res. 4, 1013–1098 **(2011)**.

73. Guillemin, S. et al. Critical Nucleation E ff ects on the Structural Relationship Between ZnO Seed Layer and Nanowires. J. Phys. Chem. C 116, 25106–25111 **(2012)**.

74. Greene, L. E., Yuhas, B. D., Law, M., Zitoun, D. & Yang, P. Solution-grown zinc oxide nanowires. Inorg. Chem. 45, 7535–7543 **(2006)**.

75. Beinik, I. et al. Electrical properties of ZnO nanorods studied by

conductive atomic force microscopy. J. Appl. Phys. 110, 1–7 **(2011)**.
76. Brillson, L. J. & Lu, Y. ZnO Schottky barriers and Ohmic contacts. J. Appl. Phys. 109, (2011).
77. Yang, S. et al. The piezotronic effect of zinc oxide nanowires studied by in situ TEM. Adv. Mater. 24, 4676–4682 **(2012)**.
78. Radich, J. G. & Kamat, P. V. Origin of reduced graphene oxide enhancements in electrochemical energy storage. ACS Catal. 2, 807–816 **(2012)**.
79. Han, D. D. et al. Moisture-responsive graphene paper prepared by self-controlled photoreduction. Adv. Mater. 27, 332–338 **(2015)**.
80. Heo, N., Jun, Y. Park, J. H. Dye molecules in electrolytes: new approach for suppression of dye-desorption in dye-sensitized solar cells. Sci. Rep. 3, 1712 **(2013)**.
81. Kim, H.-J., Lee, D.-Y., Koo, B.-K., Lee, W.-J. & Song, J.-S. Preparation and characterization of Pt counter electrode with buffer layer for dye-sensitized solar cell. Nanocomposites Nanoporous Mater. 119, 283–286 **(2007)**.
82. Park, H., Brown, P. R., Bulović, V. & Kong, J. Graphene as transparent conducting electrodes in organic photovoltaics: Studies in graphene morphology, hole transporting layers, and counter electrodes. Nano Lett. 12, 133–140 **(2012)**.
83. Fu, Y. et al. Solution growth of single crystal methylammonium lead halide perovskite nanostructures for optoelectronic and photovoltaic applications. J. Am. Chem. Soc. 137, 5810–5818 **(2015)**.
84. Wang, Z. L. Song, J. Piezoelectric Nanogenerators Based on Zinc Oxide Nanowire Arrays. Science (80). 312, 242–246 **(2006)**.
85. Gonzalez-Valls, I. & Lira-Cantu, M. Vertically-aligned nanostructures of ZnO for excitonic solar cells: a review. Energy Environ. Sci. 2, 19–34 **(2008)**.
86. Ponce, F. A., Major, J. S., Plano, W. E. & Welch, D. F. Crystalline structure of AlGaN epitaxy on sapphire using AlN buffer layers. Appl. Phys. Lett. 65, 2302–2304 **(1994)**.
87. Li, C. et al. Effect of Seed Layer on Structural Properties of ZnO Nanorod Arrays Grown by Vapor-Phase Transport. 990–995 (2008).
88. Greene, L. E. et al. General route to vertical ZnO nanowire arrays using textured ZnO seeds. Nano Lett. 5, 1231–1236 **(2005)**.
89. Baxter, J. B., Walker, a M., Ommering, K. Van & Aydil, E. S.

Synthesis and characterization of ZnO nanowires and their integration into dye-sensitized solar cells. Nanotechnology 17, S304–S312 **(2006)**.

90. Pinardi, K., Maes, H. E. & Jain, S. C. Structure of ll- VI Lattice for Mismatched Underwater Epilayers used for Lasers Communication. Science (80). 43, 31–43 **(1998)**.

91. Tian, J.-H. et al. Improved seedless hydrothermal synthesis of dense and ultralong ZnO nanowires. Nanotechnology 22, 245601 **(2011)**.

92. Fan, J. et al. Cobalt(II/III) redox electrolyte in ZnO nanowire-based dye-sensitized solar cells. ACS Appl. Mater. Interfaces 5, 1902–1906 **(2013)**.

93. Hara, K. et al. Oligothiophene-containing coumarin dyes for efficient dye-sensitized solar cells. J. Phys. Chem. B 109, 15476–15482 (2005).

94. Ito, S. et al. Control of dark current in photoelectrochemical (TiO_2/I^{-}-$I_3{}^{-}$)) and dye-sensitized solar cells. Chem. Commun. (Camb). 4351–4353 **(2005)**. doi:10.1039/b505718c

95. Chen, C. et al. Effect of polyphenyl-substituted ethylene end-capped groups in metal-free organic dyes on performance of dye-sensitized solar cells. RSC Adv. 2, 7788 **(2012)**.

96. Nayeri, F. D., Soleimani, E. A. & Salehi, F. Synthesis and characterization of ZnO nanowires grown on different seed layers: The application for dye-sensitized solar cells. Renew. Energy 60, 246–255 **(2013)**.

97. Kakati, N., Jee, S. H., Kim, S. H., Oh, J. Y. & Yoon, Y. S. Thickness dependency of sol-gel derived ZnO thin films on gas sensing behaviors. Thin Solid Films 519, 494–498 **(2010)**.

98. Song, J., Wang, X., Riedo, E. & Wang, Z. L. Elastic property of vertically aligned nanowires. Nano Lett. 5, 1954–1958 **(2005)**.

99. Kumar, A. et al. Barrier inhomogeneities limited current and 1/f noise transport in GaN based nanoscale Schottky barrier diodes. Sci. Rep. 6, 27553 **(2016)**.

100. Park, W. I., Yi, G. C., Kim, J. W. & Park, S. M. Schottky nanocontacts on ZnO nanorod arrays. Appl. Phys. Lett. 82, 4358–4360 **(2003)**.

101. Ng, H. T. et al. Growth of Epitaxial Nanowires at the Junctions of Nanowalls. Science (80). 300, 1249–1249 **(2003)**.

102. Kim, K.-H. et al. Piezoelectric two-dimensional nanosheets/anionic layer heterojunction for efficient direct current power generation. Sci. Rep. 3, 2017 **(2013)**.
103. Bang, S. et al. Photocurrent detection of chemically tuned hierarchical ZnO nanostructures grown on seed layers formed by atomic layer deposition. Nanoscale Res. Lett. 7, 290 **(2012)**.
104. Yu, L. et al. Dependence of Al^{3+} on the growth mechanism of vertical standing ZnO nanowalls and their NO_2 gas sensing properties. Sensors Actuators, B Chem. 204, 96–101 **(2014)**.
105. Iwu, K. O., Strano, V., Di Mauro, A., Impellizzeri, G. & Mirabella, S. Enhanced Quality, Growth Kinetics, and Photocatalysis of ZnO Nanowalls Prepared by Chemical Bath Deposition. Cryst. Growth Des. 15, 4206–4212 **(2015)**.
106. Islavath, N., Ramasamy, E., Das, D. & Joshi, S. V. Spray coated seed layer for scalable synthesis of aligned ZnO nanowire arrays on FTO substrate and their photovoltaic properties. Ceram. Int. 41, 4118–4122 **(2015)**.
107. Gupta, M. K., Lee, J. H., Lee, K. Y. & Kim, S. W. Two-dimensional vanadium-doped ZnO nanosheet-based flexible direct current nanogenerator. ACS Nano 7, 8932–8939 **(2013)**.
108. Ye, C., Bando, Y., Shen, G. & Golberg, D. Thickness-dependent photocatalytic performance of ZnO nanoplatelets. J. Phys. Chem. B 110, 15146–15151 **(2006)**.
109. Jun, M.-C., Park, S.-U. & Koh, J.-H. Comparative studies of Al-doped ZnO and Ga-doped ZnO transparent conducting oxide thin films. Nanoscale Res. Lett. 7, 639 **(2012)**.
110. Joo, J., Chow, B. Y., Prakash, M., Boyden, E. S. & Jacobson, J. M. Face-selective electrostatic control of hydrothermal zinc oxide nanowire synthesis. Nat. Mater. 10, 596–601 **(2011)**.
111. Yu, Y. et al. Development of lead iodide perovskite solar cells using three-dimensional titanium dioxide nanowire architectures. ACS Nano 9, 564–572 **(2015)**.
112. Jaramillo-Quintero, O. A. et al. Recombination reduction on lead halide perovskite solar cells based on low temperature synthesized hierarchical TiO_2 nanorods. Nanoscale 8, 6271–6277 **(2016)**.
113. Wagner, R. S. & Ellis, W. C. Vapor-liquid-solid mechanism of single crystal growth. Appl. Phys. Lett. 4, 89–90 **(1964)**. 114.

Givargizov, E. I. Fundamental aspects of VLS growth. J. Cryst. Growth 31, 20–30 **(1975)**.
115. Kim, D. S., Gösele, U. & Zacharias, M. Surface-diffusion induced growth of ZnO nanowires. J. Cryst. Growth 311, 3216–3219 **(2009)**.
116. Kodambaka, S., Tersoff, J., Reuter, M. C. & Ross, F. M. Diameter-independent kinetics in the vapor-liquid-solid growth of Si nanowires. Phys. Rev. Lett. 96, 1–4 **(2006)**.
117. Dahiya, A. S. et al. Controlled growth of 1D and 2D ZnO nanostructures on 4H-SiC using Au catalyst. Nanoscale Res. Lett. 9, 379 **(2014)**.
118. Zhao, C. X. et al. Large-scale synthesis of bicrystalline ZnO nanowire arrays by thermal oxidation of zinc film: Growth mechanism and high-performance field emission. Cryst. Growth Des. 13, 2897–2905 **(2013)**.
119. Hsieh, T.-H., Chen, J.-Y., Huang, C.-W. & Wu, W.-W. Observing Growth of Nanostructured ZnO in Liquid. Chem. Mater. acs.chemmater.6b02040 **(2016)**. doi:10.1021/acs.chemmater.6b02040
120. Cheng, J. J., Nicaise, S. M., Berggren, K. K. & Gradečak, S. Dimensional Tailoring of Hydrothermally Grown Zinc Oxide Nanowire Arrays. Nano Lett. 16, 753–759 **(2016)**.
121. Roy-mayhew, J. D., Bozym, D. J., Punckt, C. & Aksay, I. a. Functionalized Graphene as a Catalytic counter electrode in dye sensitized Solar Cells. ACS Nano 4, 6203–6211 **(2010)**.
122. Wang, G., Xing, W. & Zhuo, S. Nitrogen-doped graphene as low-cost counter electrode for high-efficiency dye-sensitized solar cells. Electrochim. Acta 92, 269–275 **(2013)**.
123. Roy-Mayhew, J. D., Boschloo, G., Hagfeldt, A. & Aksay, I. A. Functionalized graphene sheets as a versatile replacement for platinum in dye-sensitized solar cells. ACS Appl. Mater. Interfaces 4, 2794–2800 **(2012)**.
124. Kavan, L., Yum, J. H. & Gratzel, M. Graphene nanoplatelets outperforming platinum as the electrocatalyst in co-bipyridine-mediated dye-sensitized solar cells. Nano Lett. 11, 5501–5506 **(2011)**.
125. Vapors, A. et al. Highly Efficient Restoration of Graphitic Structure in Graphene Oxide Using. 4, 5285–5292 **(2010)**.
126. Canado, L. G. et al. Quantifying defects in graphene via Raman spectroscopy at different excitation energies. Nano Lett. 11, 3190–3196

(2011).

127. Srinivasan, S., Shin, W. H., Choi, J. W. & Coskun, A. A bifunctional approach for the preparation of graphene and ionic liquid-based hybrid gels. J. Mater. Chem. A 1, 43 **(2013)**.

128. Reina, A. et al. Large area, few-layer graphene films on arbitrary substrates by chemical vapor deposition. Nano Lett. 9, 30–35 **(2009)**.

129. Wang, H. & Hu, Y. H. Graphene as a counter electrode material for dye-sensitized solar cells. Energy Environ. Sci. 5, 8182 **(2012)**.

130. Kumara, G. R. A., Kawasaki, S., Jayaweera, P. V. V, Premalal, E. V. A. & Kaneko, S. Large area dye-sensitized solar cells with titanium based counter electrode. Thin Solid Films 520, 4119–4121 **(2012)**.

131. Casaluci, S., Gemmi, M., Pellegrini, V., Di Carlo, A. & Bonaccorso, F. Graphene-based large area dye-sensitized solar cell modules. Nanoscale 8, 5368–78 **(2016)**.